University of Stavanger

4036 Stavanger
Tel: +47 51 83 10 00
E-mail: post@uis.no
www.uis.no

ISBN: 978-82-8439-198-4
ISSN: 1890-1387

Yucong Ma University of Stavanger

Design and Dynamic Analysis of a Novel Subsea Shuttle Tanker

University of Stavanger

YUCONG MA FACULTY OF SCIENCE AND TECHNOLOGY

Design and Dynamic Analysis of a Novel Subsea Shuttle Tanker

PhD: Thesis UiS No. 730

Design and Dynamic Analysis of a Novel Subsea Shuttle Tanker

Yucong Ma

Thesis submitted in fulfilment of
the requirements for the degree of
PHILOSOPHIAE DOCTOR
(PhD)

Faculty of Science and Technology
Department of Mechanical and Structural Engineering and Materials Science
2023

University of Stavanger
NO-4036 Stavanger

www.uis.no

ISBN: 978-82-8439-198-4
ISSN: 1890-1387
PhD: Thesis UiS No. 730

Year: 2023
Title: Design and Dynamic Analysis of a Novel Subsea Shuttle Tanker
Author: Yucong Ma

Preface

This thesis is submitted in partial fulfilment of the requirements for the degree of Doctor of Philosophy (PhD) at the University of Stavanger (UiS), Norway. This PhD project was conducted in the period from August 2020 to December 2023 at the Department of Mechanical and Structural Engineering and Materials Science (IMBM), Faculty of Science and Technology (TN), University of Stavanger, with sponsorship from the Norwegian Ministry of Education and Research (Kunnskapsdepartementet, KD). Additional support was provided by the Research Council of Norway (Forskningsrådet, NFR) through the FORNY20-FORNY2020 program, project number 329115. The main supervisor was Prof. Yihan Xing, and the co-supervisors were Prof. Muk Chen Ong and Prof. Tor Henning Hemmingsen.

I confirm that this thesis is my own work. All sources and materials used in this work have been documented.

Ullandhaug, Stavanger, Norway
July 09, 2023

Yucong Ma

Acknowledgements

I sincerely thank Prof. Yihan Xing, the main supervisor of this work, for his guidance, support, and advice. His invaluable insights and experiences in both research and industry, along with his unwavering commitment, have consistently impressed me. I would also like to acknowledge the contributions of the co-supervisors of this project, Prof. Muk Chen Ong and Prof. Tor Henning Hemmingsen. Many meaningful discussions were sparked between Muk and me. His guidance on work and philosophy has been instrumental in shaping this work and will continue to influence my future endeavours. I am thankful for Tor's time and effort in reviewing, editing and providing insights into our collaborative work and this thesis. My gratitude goes equally to Prof. Dan Sui from the Department of Energy and Petroleum Engineering for her contributions to this project and her valuable input on control theory.

I would like to express my appreciation to all co-authors of the works that form the foundation of this thesis. The collaboration and friendship with Dr. Guang Yin and Dr. Marek Jan Janocha have greatly encouraged me. I also commend Terje Andreas Jevnaker for his diligence and assistance in the SST extreme hovering analysis throughout his master's thesis and our joint work.

My heartfelt thanks go to my colleagues and friends who supported and encouraged me during my PhD studies. A special mention goes to the best office mate, Dr. Omar El Beshbichi, whose constant inspiration has been invaluable on this journey. I am also grateful for my friendships with Dr. Hui Cheng, Chern Fong Lee, Zihao Wang,

Anja Schnepf, Yu Ma, and numerous other PhD candidates and post-doctoral fellows at UiS. Beyond the campus, I extend my gratitude to Chengqian Zhang for his friendship and collaboration. Alongside my research work, my involvement in the UiS doctoral community, Stipendiatorganisasjonene i Norge, the Chinese student union, and other activities have enriched my life.

Lastly, I would like to offer my deepest appreciation to my parents, Jianan Zhang, my cat Eowyn, and my dog Sofie, for their unwavering love and companionship.

Abstract

Underwater pipelines, tanker ships, and liquefied gas carriers have traditionally been employed to transport hydrocarbons between offshore oil and gas facilities and onshore locations. However, both methods come with limitations. Underwater pipelines are costly to install and maintain, while the operation of tanker ships and liquefied gas carriers is heavily dependent on weather conditions, rendering them impractical in severe sea states. As an alternative, a pioneering subsea shuttle tanker (SST) system was proposed as an alternative for offshore transportation. The SST was designed to function at a constant speed and depth beneath the ocean surface, specifically designed for transporting liquid carbon dioxide from existing onshore/offshore sites where carbon dioxide is captured or temporarily stored, to subsea wells for reservoir injection. Nonetheless, the potential applications of the SST extend to being a versatile freight carrier, capable of transporting diverse cargoes such as subsea tools, hydrocarbons, chemicals, and even electricity.

This PhD project unfolds in two phases: design and dynamic analysis. In the design phase, a baseline design for the SST was formulated based on existing literature. This comprehensive design encompasses critical aspects of SST design and operation, including structural design, hydrostatic stability computations, resistance and propulsion estimations, operational scenarios, and offloading methodologies. Challenges inherent to CO_2 SST transportation were scrutinised, involving thermodynamic properties, purity considerations, and hydrate formation of CO_2 during various vessel-transportation states. These aspects

were explored in relation to cargo sizing, material selection, and energy consumption.

The second phase revolves around dynamic analysis, centred on the derived baseline SST. A manoeuvring model for the SST was constructed as a foundation. Hydrodynamic derivatives were calculated using semi-empirical formulas. Subsequently, the SST's capability to maintain position during the offloading process was evaluated. A linear quadratic regulator was employed to address the SST's station-keeping challenge in stochastic currents, ensuring the vessel remains stationary during offloading. The model was further extended to explore the station-keeping under extreme current conditions, utilising probabilistic methods to predict maximum and minimum depth excursions. These predictions offer valuable insights for cost-effective SST design and operational decision-making.

The study then delved into the SST's recoverability under undesired malfunctions through the establishment of a safety operating envelope (SOE). This envelope considered potential submersible malfunctions, such as partial flooding, jam-to-rise, and jam-to-dive incidents. By identifying feasible speed and depth ranges from an operational safety perspective, the SOE contributes to a reduction in the designed collapse depth, leading to cost savings in materials and enhanced payload capacity.

Furthermore, computational fluid dynamics (CFD) analysis was conducted to predict pressure, skin friction, drag, and lift forces affecting the SST. This included scenarios of the SST's near-wall voyage and hovering.

Collectively, the original contributions of this thesis encompass the conceptual design, application of control systems and dynamic analysis of the SST. These contributions pave the way for future exploration in the development of commercial submarine concepts and diverse ocean space utilisation strategies.

Publications during the PhD

The material comprising this doctoral dissertation has been acknowledged and published in peer-reviewed journals and conferences, ensuring the thesis's quality. All contents in these publications have been confirmed for copyright compliance and authorised for inclusion in this thesis.

The licensing for Paper 1, Paper 4, and Paper 5 is governed by CC BY 4.0. Paper 2 is licensed under CC BY 3.0. Copyright for Paper 3 and Paper 6 is held by the American Society of Mechanical Engineers (ASME). Permission has been obtained from ASME to incorporate Paper 3 and Paper 6 - in whole or in part, as is or adapted - in this thesis. The publications included in this thesis are enumerated below:

Paper 1

Ma, Y., Xing, Y., Ong, M. C., & Hemmingsen, T. H. (2021). Baseline design of a subsea shuttle tanker system for liquid carbon dioxide transportation. *Ocean Engineering*, 240, 109891.

Paper 2

Ma, Y., Xing, Y., & Hemmingsen, T. H. (2021). An evaluation of key challenges of CO2 transportation with a novel Subsea Shuttle Tanker. In *Proceedings of the Third Conference of Computational Methods & Ocean Technology (COTech 2021)*, 1201(1), 012078.

Paper 3

Ma, Y., Xing, Y., & Sui, D. (2023). Trajectory envelope of a subsea shuttle tanker hovering in stochastic ocean current—model development and tuning. *Journal of Offshore Mechanics and Arctic Engineering*, 145(3), 030901.

Paper 4

Ma, Y., Jevnaker, T. A., & Xing, Y. (2023). Station keeping of a subsea shuttle tanker system under extreme current during offloading. *Ships and Offshore Structures*, 1-13.

Paper 5

Ma, Y., & Xing, Y. (2022). Identification of the safety operating envelope of a novel subsea shuttle tanker. *Ocean Engineering*, 266, 112750.

Paper 6

Ma, Y., Yin, G., Janocha, M., Xing, Y., & Ong, M. C. (2023). Numerical investigation on near-bottom operation of an extra-large freight submarine. *Journal of Offshore Mechanics and Arctic Engineering*, 1-24.

In addition, my studies, including the work that formulates the thesis, served as a basis and were extended to other works, including thesis for master students, conference proceedings, and journal articles. The publications I was involved in during my PhD study but not included in this thesis are listed below:

Paper 7

Ma, Y., Sui, D., Xing, Y., Ong, M. C., & Hemmingsen, T. H. (2021). Depth control modelling and analysis of a subsea shuttle tanker. In *40th International Conference on Offshore Mechanics and Arctic Engineering*, 85154, V005T05A026.

Paper 8

Xing, Y., Santoso, T. A. D., & Ma, Y. (2021). Technical–economic feasibility analysis of subsea shuttle tanker. *Journal of Marine Science and Engineering*, 10(1), 20.

Paper 9

Dai, T., Yang, S., Xing, Y., & Ma, Y. (2022). Dynamic design and analysis of subsea CO2 discharging flowline for cargo submarines used for CCS in low-carbon and renewable energy value chains. *Frontiers in Marine Science*, 9, 1016062.

Paper 10

Xing, Y., Gaidai, O., Ma, Y., Naess, A., & Wang, F. (2022). A novel design approach for estimation of extreme responses of a subsea shuttle tanker hovering in ocean current considering aft thruster failure. *Applied Ocean Research*, 123, 103179.

Paper 11

Ma, Y., Xing, Y., Silva, M. S. D., & Sui, D. (2022). Modelling of a subsea shuttle tanker hovering in ocean currents. In *41st International*

Conference on Offshore Mechanics and Arctic Engineering, 85901, V05BT06A039.

Paper 12

Jamissen, P. L., Xing, Y., & Ma, Y. (2022). Probabilistic Design of Thin-Walled Cylindrical Structures for Application In Large Cargo Submarines. In *41st International Conference on Offshore Mechanics and Arctic Engineering*, 85895, V05AT06A010.

Paper 13

Ma, Y., Xing, Y., Sui, D., Ong, M. C., & Hemmingsen, T. H. (2023). Two-Dimensional Planar Modelling of the Depth Control of a Subsea Shuttle Tanker. *Journal of Offshore Mechanics and Arctic Engineering*, 145(4), 044501.

Paper 14

Ahmad, U. N., Xing, Y., & Ma, Y. (2023). UiS Subsea-Freight Glider: A Large Buoyancy-Driven Autonomous Cargo Glider. *Journal of Offshore Mechanics and Arctic Engineering*, 145(4), 045001.

Paper 15

Yousef, H. H., Ma, Y., Xing, Y., & Xu, X. (2023). Uncertainty analysis of the safety operating envelope of a subsea shuttle tanker. In *42nd International Conference on Offshore Mechanics and Arctic Engineering*, 86878, V005T06A088.

Paper 16

Patel, K. S., Ma, Y., Xing, Y., & Li, L. (2023). Modelling and analysis of the bending moment in a subsea shuttle tanker under the effect of waves using a multi-body approach. In *42nd International Conference on Offshore Mechanics and Arctic Engineering*, 86878, V005T06A087.

Paper 17

Zhang, C., Ma, Y., Thies, F., Ringsberg, J. W., & Xing, Y. (2023). Towards autonomous inland shipping: a manoeuvring model in confined waterways. *Ships and Offshore Structures*. (under review)

Paper 18

Yousef, H. H., Ma, Y., Patel, K. S., & Xing, Y. (2023). A novel design of a hybrid glulam-steel substructure for the IEA 15-MW floating wind turbine. In *Proceedings of the Fourth Conference of Computational Methods & Ocean Technology (COTech 2023)*. (accepted)

Nomenclature

Abbreviations

2D	Two-dimensional
3D	Three-dimensional
$k-\omega$ SST	$k-\omega$ shear stress transport
ACER	Averaged conditional exceedance rate
BG	Distance between the centres of buoyancy and gravity
CAD	Computer-aided design
CCS	Carbon capture and storage
CFD	Computational fluid dynamics
CH_3CHO	Acetaldehyde
CI	Confidence interval
CO	Carbon monoxide
CO_2	Carbon dioxide
CoB	Centre of buoyancy
CoG	Centre of gravity
DWT	Deadweight tonnage

EOR	Enhanced oil recovery
FPU	Floating production unites
GM	Metacentric height
H_2	Hydrogen
H_2O	Water
H_xS	Hydrogen sulphide
HCHO	Formaldehyde
LNG	Liquefied natural gas
LPG	Liquefied petroleum gas
M	Metacentre
NH_3	Ammonia
NO_x	Nitrogen oxides
O_2	Oxygen
PCS	Pressure Compensation System
ppm	Parts per million
ppmv	Parts per million by volume
PSD	Power spectral density
QPC	Quasi-propulsive coefficient
RANS	Reynolds-averaged Navier–Stokes
RNH_3	Amines
ROV	Remotely operated vehicle

SIMPLE	Semi-Implicit Method for Pressure Linked Equations
SO_x	Sulphur oxides
SOE	Safety operating envelop
SOP	Standard Operating Procedure
SST	Subsea shuttle tanker
VLGC	Very large gas carrier

Control, Manoeuvring, and Fluid Dynamic Analysis Variables

$\boldsymbol{\eta}$	Vector consists of NED position and Euler angles
$\boldsymbol{\nu}$	Linear and angular velocity in the body-fixed system
$\boldsymbol{\tau}$	Control force vector
$\boldsymbol{C}_c(\boldsymbol{\nu})$	Coriolis-centripetal matrix
$\boldsymbol{D}_d(\boldsymbol{\nu})$	Damping matrix
$\boldsymbol{g}(\boldsymbol{\eta})$	Force vector
$\boldsymbol{J}_\Theta(\boldsymbol{\eta})$	Euler transformation matrix
$\boldsymbol{M}$	System mass matrix
$\dot{(\,)}$	Time derivative
$\hat{\boldsymbol{x}}$	Observed state
$\hat{\boldsymbol{y}}$	Observed output
μ_1, μ_2	Constants in ocean current realisation

ω_1, ω_2	Ocean current inflow angle
$\Re$	Real number
$\boldsymbol{A}$	State matrix
$\boldsymbol{B}$	Input matrix
$\boldsymbol{Con}$	Controllability
$\boldsymbol{C}$	Output matrix
$\boldsymbol{G}$	Gain matrix
$\boldsymbol{L}$	LQR cost function
$\boldsymbol{Obs}$	Observability
$\boldsymbol{P}_\infty$	Positively defined symmetric matrix obtained from the Riccati equation
$\boldsymbol{R}$	Effort weight matrix
$\boldsymbol{u}$	System's input
$\boldsymbol{x}$	System's state
$\boldsymbol{y}$	System's outputs
θ_c	Ocean current inflow angle
C_b	Tank blowing constant
C_g	Gas constant
D_t	Compensation tank diameter
J	LQR Cost function
m_{a0}	Initial mass of the compressed air for compensation tank blowing

N, D, θ	Position in North, down, and pitch
N_t	total number of compensation tanks
p_a	Atmospheric pressure
T	Temperature in compensation tanks
t	Time
V_c	Ocean current speed
Vol_a	Air volume inside compensation tank
Vol_t	Single compensation tank volume
x_t	Compensation tank position along the x-axis
z_0	Diving depth

ACER

α_{kj}	Exceedance probability
η	Extreme response
M_N	Extreme value distribution function
N	number of sample points for a specific moment X_n
P_η	Probability of response
$P_k(\eta)$	Succession of conditional approximation
R	Number of samples or realisations
r	specific realisation number
$\hat{s}_k(\eta)$	standard deviation of samples

CFD Analysis

Δy	Distance between the first grid centre and the wall
κ	von Karman constant
ν	Kinematic viscosity
ν_t	Turbulent eddy viscosity
$\overline{(\,)}$	Reynolds average of the physical variables
$\overline{u_i' u_j'}$	Reynolds stress
$\overline{u_i}, \overline{u_j}$	Corresponding Reynolds averaged velocity components
ρ	Water density
τ_{wall}	Wall shear stress
C_D	Drag coefficient
C_F	Skin friction coefficient
C_f	Wall shear stress coefficient
C_L	Lift coefficient
C_P	Form drag coefficient
C_p	Pressure coefficient
$CD_{k\omega}$	Positive part of the cross-diffusion term
F_1, F_2	Blending functions
F_x	Drag force
F_y	Downward pointing lift force
F_{Fx}	Total friction drag

F_{Px}	Total form drag
h	Distance from the wall at the boundary layer
$i, j = 1, 2, 3$	directions
k_s	Seabed roughness
p	Pressure
p_∞	Pressure in the free stream
P_b	Body force to generate one-dimensional precursor flow
Re	Reynolds number
S	Invariant of the strain rate
u^*	Friction velocity
U_*	Friction velocity
U_∞	Freestream current velocity outside the boundary layer
u_i, u_j	Velocity components
$u_i\prime, u_j\prime$	Velocity fluctuations
x_i, x_j	Spatial directions
y^+	Non-dimensional wall distance
y_w	Distance to the wall

SST Design Variables

α_C	SST Tailcone angle
σ_y	yield stress

A_f	SST frontal projected area
c_d	Axial drag coefficient
$C_{D\delta}$	Drag rate coefficient
c_{dc}	Cylinder's cross-flow drag coefficient
$C_{L\delta}$	Lift rate coefficient
$c_{yd\beta}$	Lift slope coefficient
D	SST beam
D_p	Propeller diameter
D_t	Tunnel thruster diameter
D_{out}	External diameter of the cylinder
G	Gap distance between the SST bottom and seabed
I_{yy}	Pitch moment of inertia
J	Advance number
K_{Tp}	Main propeller thrust coefficient
K_{Tt}	Tunnel thruster thrust coefficient
L	SST length
L_{tank}	Cargo tank length
$m_a(x)$	Added mass of a submerged body slice at point x
$M_{\delta c}$	Control plane pitch moment
n	Propeller rotational speed in RPM

N_B	Number of blades
$p_{internal}$	Cargo tank internal pressure
$R(x)$	Radius of cross section of point x
S_{hub}	Wetted surface area of the propeller hub
S_{hull}	Wetted surface area of the hull
S_{wet}	Wetted surface area
SF	Safety factor
t_{tank}	Cargo tank wall thickness
V_A	Advance velocity
V_{tank}	Cargo tank volume
w_T	Wake fraction
W_{tank}	Cargo tank steel weight
$X_{\dot{u}}$	Axial added mass
$X_{(\ )}$, $Z_{(\ )}$, $M_{(\ )}$	Hydrodynamic derivatives
$X_{\delta c}$	Control plane drag
x_{cp}	Viscous force centre x position
x_{ta}	Aft tunnel thruster position
x_{tf}	Forward tunnel thruster position
$Z_{\delta c}$	Control plane lift

Contents

Chapter 1

Introduction

1.1 Motivation

1.1.1 An Alternative for Future Sustainable Maritime Transportation and Decarbonisation

Most offshore oil and gas production is transported from floating production units (FPUs) to onshore facilities through subsea pipelines [1]. Over the years, subsea pipeline laying techniques have significantly advanced, becoming a mature technology [2]. However, this transportation method is restricted by some technical and economic factors. One major constraint is the high cost of deployment, especially for remote oil and gas fields with long transmission lengths. As pipeline lengths increase, the costs escalate significantly.

Furthermore, the task of inspecting deep-sea pipelines can be a complex and costly endeavour. Moreover, maintaining and repairing pipelines at such depths frequently require partial or complete shutdowns, which can be economically disadvantageous. As a result, subsea pipelines are better suited for expansive fields with substantial profit margins and shorter transportation distances [3]. For single remote marginal fields, this solution may not be economically attractive, leading to the frequent use of shuttle tankers [4].

Shuttle tankers provide a highly flexible solution that can be de-

ployed to different fields as needed. In vessel downtime, a replacement tanker can be readily deployed. However, tanker ships are floating structures exposed to significant dynamic load effects from wind and waves. Therefore, their operations depend highly on weather conditions and cannot be conducted in severe sea states to mitigate the risk of collision and damage to the hawser and flowlines.

The Subsea Shuttle Tanker (SST) concept is proposed as an innovative alternative to address these limitations. As displayed in Figure 1.1, the SST is an extra-large autonomous submarine for commercial transport. This concept combines the adaptability and cost-effectiveness of a shuttle tanker with the capability to function undersurface in all types of weather conditions.

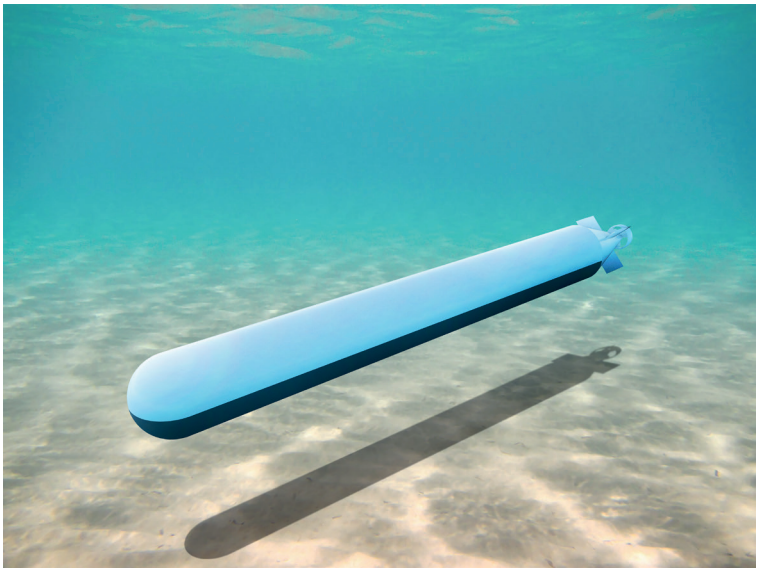

Figure 1.1: SST illustration.

The principal aim of the SST is the autonomous transport of CO_2 from offshore or land facilities to subsea wells for direct injection. Its role in the operations of the offshore carbon capture and storage (CCS) supply chain is depicted in Figure 1.2. The baseline SST is ex-

plicitly tailored for deployment in the Norwegian sector. According to the Norwegian Petroleum Directorate, three ongoing CCS projects are currently underway - Sleipner, Utgard, and Snøhvit [5]. These projects involve capturing CO_2 generated from hydrocarbon production and re-injecting it into the reservoir. In addition to these three projects, the Northern Lights project [6] is set to commence operations in 2024. Its objective is to transport CO_2 from land-based, non-petroleum-related industrial activities to the Troll field for injection into the Utsira formation. The locations of these CCS projects are outlined in Figure 1.3. The selected Norwegian fields align with the mission requirements as they are currently being used for CCS storage. However, the SST can be designed to function in diverse locations worldwide, each with its specific demands. While its primary cargo is CO_2, the SST can also transport other types of cargo, including hydrocarbons, electrical power (utilising batteries), and subsea tools.

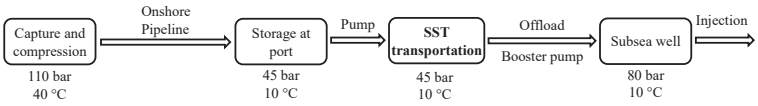

Figure 1.2: Offshore CCS process with SST transportation.

The SST offers several contributions to mitigating global warming. Firstly, it operates on fully electric power, resulting in zero emissions and contributing to sustainable shipping. Maritime transport currently contributes to roughly 3.3% of CO_2 emissions linked to fossil fuels [7]. Furthermore, the SST facilitates the transformation of marginal subsea fields into offshore CO_2 storage locations, thereby supporting the growing worldwide requirement for CCS. The Conference of the Parties 2021 (COP 21) agreement is a crucial international treaty on climate change, aiming to control the global mean temperature increase within 2 °C above pre-industrial levels and limiting it to 1.5 °C before mid-century [8].To achieve this ambitious target, substantial efforts from all countries are required. The Intergovernmen-

tal Panel on Climate Change (IPCC) has recommended a reduction of global CO_2 emissions by 50-85% from the 28.2 Gt/yr level in the 2000s [9]. However, recent reports indicate that the world is still falling short of these goals, with annual emissions reaching 35.9 Gt/yr in 2019 and slightly reduced to 33.6 Gt/yr in 2020 due to the COVID-19 pandemic's impact on economic activity [10]. In Europe, there is a growing consensus that CCS is a necessary solution to decarbonise various industries and achieve net-zero goals. CCS projects have shown significant potential, particularly in addressing emissions from hard-to-abate sectors such as waste incineration and cement production. Without CCS, decarbonising these industries would pose considerable challenges. These sectors currently emit approximately 319 million tonnes of CO_2 annually, accounting for around 9% of Europe's total CO_2 emissions. Considering the ongoing CCS projects, it is projected that by 2030, around 110 million tonnes of CO_2 per year will be captured [11]. Therefore, any economical solution that enhances the global CCS storage supply is crucial for mitigating the rising trend in global mean temperature, which is getting worse due to the increasing global energy demand, potentially doubling atmospheric CO_2 concentrations by 2100 compared to 1960 levels [12].

1.1.2 Design Challenges for the SST

In the ship design process, it is essential for naval architects to receive clear and comprehensive requirements from the client. These requirements should be systematically managed and continuously refined throughout the entire design spiral, starting from the conceptual design phase.

The SST is a unique type of submersible that primarily operates underwater, resurfacing only for occasional maintenance and repair. While smaller civilian submarines have been developed for ocean research and leisure purposes, submarines of comparable size to the SST

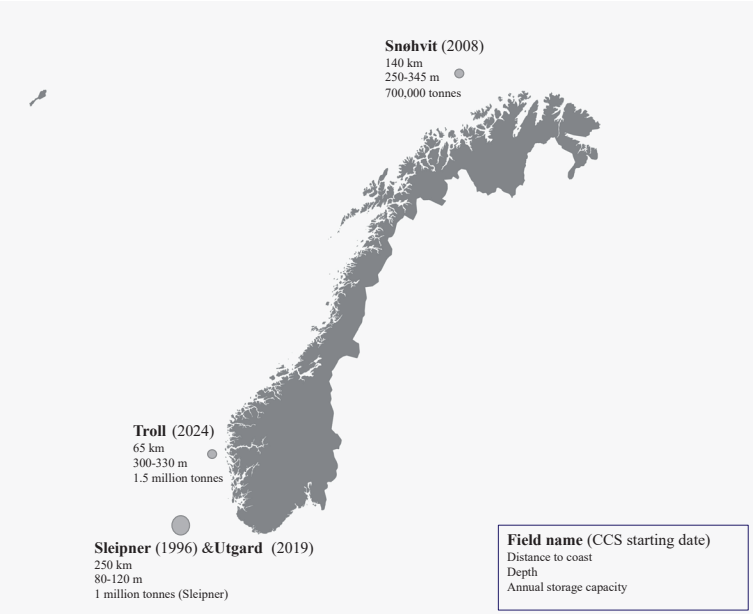

Figure 1.3: Map of ongoing and planned carbon dioxide storage sites in the Norwegian sector [5, 6].

(100 to 200 metres in length) have mainly been constructed for military applications. These large military submarines are typically designed to carry and launch ballistic missiles and torpedoes. As a result, the design of the subsea shuttle tanker will draw upon existing submarine experiences to a significant extent. Although detailed information about the exact design specifics of military submarines is limited due to the need to maintain operational and research secrecy, various studies have documented relevant design methods and principles [13–18].

Designing an SST with a high cargo capacity presents a significant challenge. Unlike military submarines, which prioritise heavy structures and have limited payload capacities, the SST must maximise its available space for payload. Xing et al. (2021) [19] have established a design target where the dry weight of the SST accounts for 52% of the total payload, ensuring its economic viability. To provide context,

it is worth noting that the payload capacity of an aircraft like the Boeing 747-400F is approximately 28% of its weight [20], while a ship tanker can have a payload capacity of up to 80% of its weight [21]. However, this payload capacity significantly surpasses that of military submarines, which typically carry a payload of less than 10% of their dry weight. Figure 1.4 provides a visual comparison of the dry weight distribution target between the SST and Albacore submarines.

Nuclear-powered and diesel-electric submarines typically have payload capacities of approximately 8% and 9%, respectively. In the case of the aforementioned military submarines, nearly half of the dry weight comprises structural components. This emphasis on structure arises from the need for submarines to withstand collapse depths significantly greater than their maximum operating depth. Consequently, the structural design of military submarines often incorporates expensive high-strength steels, thick plates, and closely arranged stiffeners.

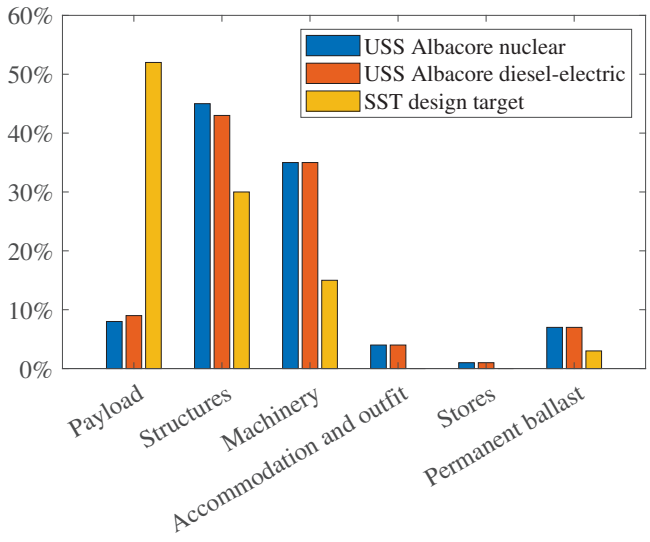

Figure 1.4: Dry weight distribution of USS Albacore submarines [15] and the SST design target [19].

Conversely, the SST's primary objective is to transport cargo in the most cost-efficient manner, necessitating an efficient structural design. The challenge lies in finding a balance between payload capacity and structural integrity to meet the economic requirements of the SST.

Achieving low drag resistance is another significant design challenge for the SST. A tear-drop-shaped hull form offers approximately half the relative drag compared to a cylindrical hull. However, the tear-drop shape entails curvature in both horizontal and vertical directions, making it more complex to fabricate at shipyards. The construction of plates with such intricate geometries necessitates multiple line heating forming processes, which can result in reduced geometric accuracy. Moreover, submarines' collapse pressure capacity is susceptible to imperfections. Even a tiny imperfection of just 1% in geometry can lead to a more than 50% reduction in collapse capacity [22]. This highlights the difficulty of manufacturing a hydrodynamically efficient hull with a high collapse pressure capacity.

This thesis aims to provide a new starting point for optimising and analysing the SST for CO_2 transport or general subsea operation. A baseline design of the SST for liquid carbon dioxide transport is presented. Main design parameters such as the following are covered to answer the key design questions:

- Design requirements.
- CO_2 treatment.
- General arrangement.
- Hydrostatic properties.
- External hull configuration.
- Cargo and ballast tank configuration.
- Hydrodynamic, propulsion, and powering estimation.

- Key features include the pressure compensation system (PCS) and offloading method.

1.1.3 Dynamic Analysis Serves for an Efficient SST Design

A thorough understanding of the dynamic response of the SST is essential to answer some of the most critical design questions. It can help naval architects figure out the depth ranges during voyages, hovering, and emergencies.

Hovering Analysis

Performing offloading dynamic analysis is crucial for the SST design. The SST is connected to the subsea well with a flowline. The SST is subjected to various environmental loads during the offloading process. Figure 1.5 depicts the key environmental loads comprising hydrostatic pressure, waves (if it offloads in shallow waters), buoyancy, and currents. Among these, current disturbances exert the most substantial impact on the SST, given that these load effects are non-uniform, time-dependent, and predominantly drag-induced.

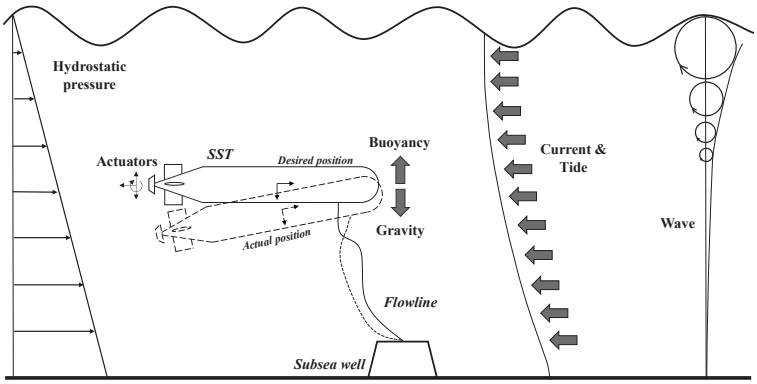

Figure 1.5: Environmental loads acting on the SST.

During this procedure, the SST's surge motion influences the necessary hose length to mitigate the potential hazards of overstretching or sudden loads on the connection junction. The hover system's design significantly influences the SST's efficiency, as it could potentially consume excessive energy if not thoughtfully configured to handle the prevailing environmental conditions. Furthermore, safe operation, collision avoidance, and maintaining position in the presence of currents should all be considered when sizing the thrusters.

Moreover, the efficiency of the SST is directly influenced by its hovering system, which can lead to unnecessary energy consumption if not thoughtfully designed to handle varying environmental conditions during operation. Moreover, the controller design must also address safety aspects, such as collision avoidance and effective station-keeping in the presence of currents. These factors ensure the SST's optimal performance and safe operation during offloading.

In addition to the regular hovering responses, an additional investigation is carried out regarding the SST's extreme positional responses, specifically in terms of extreme surge and heave motions. This study aims to assess the maximum depth excursion and identify the extreme hydrostatic loads that the SST may encounter during its operations. Obtaining a thorough grasp of the behaviour in extreme currents is crucial for the design of the SST. Given the slender nature of such structures, it's important to note that side-way current drag can reach up to 80 times the force exerted by the heading current [23]. Consequently, the SST is required to face the current head-on while offloading continuously.

Near-seabed Operation

Furthermore, it depends on the SST's mission requirement. It is unavoidable that the SST may be required to hover or voyage near the seabed. A thorough understanding of seabed boundary effects is crucial to successfully conduct near-seabed operations, as they can am-

plify drag-dominated loads in the vertical direction. Depending on the operational scenario, these load effects may significantly affect the pressure drag in the horizontal direction [24] and result in vertical forces pointing at the seabed [25]. The first scenario occurs when the subsea shuttle operates near the seabed in still water. As the shuttle approaches the seabed, the flow velocity increases between the bottom of the subsea shuttle and the seabed, creating a downward-pointing vertical force and a pitch moment around the transverse axis.

As a result, the subsea shuttle is expected to descend more rapidly and experience significant trim motion. Effective thruster responses or hydroplane deflections are necessary to maintain clearance from the seabed and avoid collisions with subsea structures. This phenomenon is akin to the well-known squatting effect experienced by ships when sailing through canal banks or interacting with other ships [25, 26].

Evaluating near-bottom loads enables more efficient sizing of auxiliary actuators and control surfaces. Combining environmental loads and actuation forces provides the contact force during subsea shuttle docking, making accurate predictions of this force is crucial for reliable structural design.

Accidents

Accidents involving SSTs have the potential to result in the loss of the vessel, CO_2 or hydrocarbon leaks, and damage to offshore facilities or third parties. These outcomes could lead to property damage, environmental contamination, or even casualties. Hence, prioritising safety during operations is paramount in the SST's design.

1.2 Related Work

1.2.1 Early Commercial Submarine Concept

The blueprint for utilising large underwater vehicles for freight, especially hydrocarbon transportation, is not new and was initially proposed in the 1970s. Jacobsen (1971) and Taylor et al. (1977) suggested the use of nuclear-propelled submarines of various sizes ranging from 20,000 to 420,000 deadweight tonnage (DWT) for transporting Arctic crude oil [27, 28]. In 1974, the US National Maritime Research Centre studied the concepts and problems regarding the use of nuclear-powered submarine tankers for the transportation of oil from the Arctic regions. The problems and advantages are compared with surface tankers, tug-barges and pipelines. The report focused on the deck department and highlighted the challenge of required skill sets and techniques for the onboard officers and crew members [29]. In the 1980s, Jacobsen et al. (1983) proposed two massive submarine Arctic liquefied natural gas (LNG) tanker concepts: a 660,800 DWT nuclear-powered version and a 727,400 DWT non-nuclear-powered version [30]. The 660,800 DWT nuclear submarine LNG tanker is illustrated in Figure 1.6. More recently, Brandt et al. (2015) presented a 3,500 DWT multi-purpose submarine designed for various subsea operations, including installation, inspection, maintenance, and repair in water depths of up to 1,500 m in the Arctic region [31]. Ahmad et al. (2022) further proposed a 1,500 DWT subsea cargo glider with an average power consumption of less than 10 kW [32].

1.2.2 Equinor Subsea Shuttle System

Equinor ASA unveiled a subsea “cargo-train” concept, or the Subsea Shuttle System, in a defensive research disclosure in 2019 [33]. One possible design is shown in Figure 1.7. The research disclosure pro-

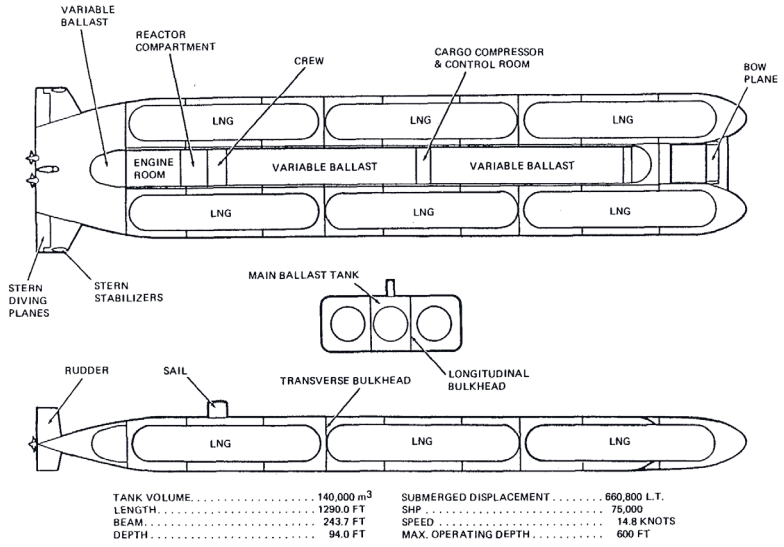

Figure 1.6: A general arrangement plan for a nuclear submarine LNG tanker designed in Jacobsen et al. (1983) [30].

posed a series of extra-large autonomous submersibles powered using non-fossil energy sources with a length between 100 and 200 metres and a beam from 10 to 20 metres. This system was primarily designed for voyaging at a constant depth following a fixed route in the water.

The system was designed to serve as a general transportation tool in the offshore oil and gas sector. It aimed to carry a wide range of cargo, including but not limited to oil, gas, power banks, monoethylene glycol, chemicals, separation units, and carbon dioxide (CO_2). Moreover, it was believed that this system could be configured to carry tools, structures and modules required for subsea construction and invention. Additionally, the system has the capability to transport electricity to subsea equipment by storing it in battery banks and transferring it during docking. As a subsea vehicle, the SST is not subject to weather conditions, allowing it to operate in even severe weather without relying on surface vessels.

Additionally, it can take advantage of the external hydrostatic pressure and temperature as part of its design. The ability to operate re-

motely or autonomously enhances safety compared to conventional manned marine operations. This innovative system has the potential to significantly reduce field development costs by eliminating or minimising the need for subsea pipelines, umbilicals, storage tanks, offshore loading systems, tankers, and related marine operations. The reduction of these components also contributes to a decreased carbon footprint and environmental impact associated with field development.

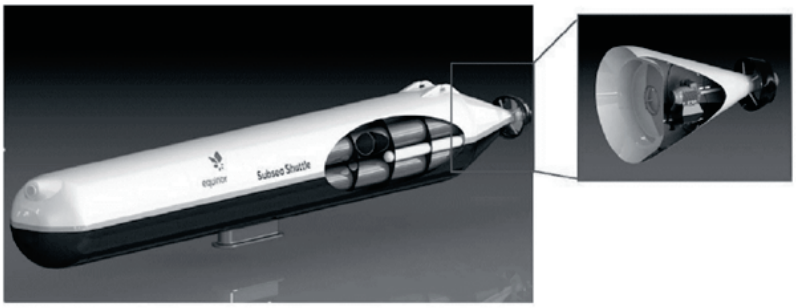

Figure 1.7: A possible design of the Equinor "cargo train" [33].

Its main propulsion system consists of an aft main propeller, complemented by a directional thruster at the bow for direction control. The machinery and ballast tanks are strategically located at the shuttle's bow and aft sections, while heavy components, including a large battery pack and a docking interface, are situated at the bottom to increase hydrostatic stability. These structures can be potentially integrated inside the hull to minimise drag. The docking interface facilitates the transfer of fluids and electrical power through hydraulic and electrical connectors when the shuttle docks onto subsea equipment or a riser base. The shuttle generally operates at low velocities to minimise drag forces and reduce energy consumption.

A follow-up disclosure published by Ellingsen et al. (2020) provided more entailed considerations on the design, type, and application of the subsea shuttle system [34]. Some of the different tank ar-

rangements are exemplified in Figure 1.8. In the disclosure, an innovative maritime freight option—a subsea composed of interconnected subsea train-like tanks with independent propulsion units located at the vessel bow or aft. An ultra-efficient large subsea transport glider was also proposed.

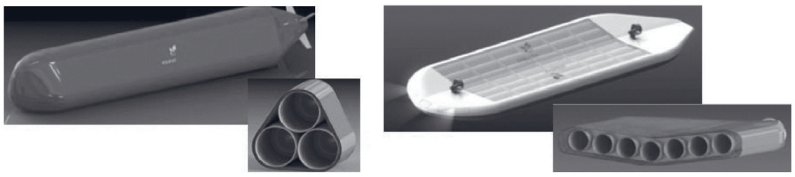

Figure 1.8: Different Equinor subsea shuttle system tank arrangements [34].

1.3 Aim and Scope

This thesis aims to address the existing knowledge gap by providing a detailed global design specification for the baseline SST and conducting dynamic analyses of its operation. The document is structured into two main parts. In the first part, a conceptual SST is proposed, addressing crucial design considerations outlined in [19], including pressure hull design, pressure compensation system, and power estimation; the second part of the thesis adapts the baseline SST and conducts dynamic analysis based on different operation scenarios.

This thesis consists of nine chapters. Chapter 1 overviews this work's motivation, aim and scope. It also presents the past merchant submarine design and the history of the Equinor subsea shuttle, which significantly influenced the scope of this thesis and served as background information. The detailed delineation of the theories used in this study follows in Chapter 2.

Chapter 3 concludes the work from Paper 1 [23], providing an in-

depth exposition of the baseline design of a 34,000-tonne SST. The baseline SST is fully electric-powered and has a length and beam of 164 m and 17 m, respectively. It possesses a cargo-carrying capacity of 16,362 m^3, enabling it to meet the annual storage demands of ongoing CCS projects in Norway. This chapter covers critical design parameters, including general arrangement, structural design, cargo properties, hydrostatic properties, and power estimation. Key features, such as the pressure compensation system (PCS) and offloading methods, are also presented.

Chapter 4 evaluates the key challenges of using such a vessel for CO_2 transportation based on the baseline SST configurations. It discusses essential properties, such as thermodynamic properties, purity, and hydrate formation of CO_2 at different vessel-transportation states and their relation to cargo sizing, material selection, and energy consumption. The results are peer-reviewed and published in Paper 2 [35].

In Chapter 5, the work is published in Paper 3 [36]. A linear quadratic regulator is employed to address the SST's hovering challenge in the presence of stochastic currents. The chapter includes case studies where the SST's trajectory envelopes are analysed under average current velocities of 0.5 m/s, 1.0 m/s, and 1.5 m/s. The numerical findings demonstrate that the provided hovering control system effectively maintains the SST's stability during offloading.

Chapter 6 examines the SST's behaviour during hovering in extreme ocean currents. The results are documented in Paper 4 [37]. This analysis focuses on surge, heave, and pitch motions. The averaged conditional exceedance rate (ACER) method is applied to forecast the potential maximum and minimum depth excursions. The outcomes of this extreme value prediction are crucial in realising a cost-effective design for the SST and offering valuable guidance to decision-makers regarding its operational considerations.

Chapter 7 documents the work from Paper 5 [38] - the Safe Operating Envelope (SOE) identification for the SST, encompassing the

safety operation zones. Standard operating procedures for recovery actions are established to address potential malfunctions. Free-running simulations are conducted to explore three failure scenarios of SST recovery responses. Eventually, the established SOE defines feasible speed and depth excursion ranges for the SST from an operational safety perspective.

In Chapter 8, the hydrodynamic performance of the SST during near-seabed operations is studied. The results are presented in Paper 6 [39]. A three-dimensional (3D) Reynolds-Averaged Navier-Stokes (RANS) method, combined with the $k-\omega$ shear stress transport ($k-\omega$ SST) model, is employed to predict pressure, skin friction, drag, and lift forces acting on the SST. The numerical model is verified and validated against experimental and numerical data from the SUBOFF-1 project, a standard submarine model developed by the Defence Advanced Research Projects Agency. The study considers two operational scenarios: (1) the subsea shuttle travelling near the seabed with forward speed; and (2) the subsea shuttle hovering close to the seabed and experiencing incoming current flow. The analyses consider a representative seabed boundary layer profile generated using one-dimensional (1D) simulations and implemented as the inlet boundary condition in the 3D simulations.

Finally, the results are summarised in Chapter 9, which also provides some suggestions for future work in this field.

Chapter 2

Methodology

2.1 Design Methodology

The design methodology used for the Subsea Shuttle Tanker (SST) is presented in Figure 2.1 as a design flowchart and briefly discussed in this section. The design process starts with identifying the mission requirements, including the depth, range, cargo capacity, and environmental data in Section 3.2. Based on these mission requirements, the properties of the CO_2 cargo, expected load-effects, required speed, and range are determined (see Section 3.3).

The expected load-effects are used to define the structural properties of the SST (see Section 3.6). These load-effects result from various factors, including water depth, offloading operations (see Section 3.9), and the CO_2 cargo. The structural properties encompass the definition of the external hull, the inner tank, and the materials used. Additionally, a pressure compensation system (PCS) (see Section 3.8) is proposed to handle large collapse pressure loads. The PCS is a design innovation specific to the SST and integrated into all mission requirements.

The required speed and range of the SST influence the hydrodynamics and propulsion design. These aspects are also affected by the vessel's manoeuvrability and the resulting external hull geometry defined by the structural properties. Section 3.7 addresses drag and

power considerations, propeller design, energy consumption, and battery selection.

The hydrostatic properties of the SST (see Section 3.5) are calculated based on the general arrangement and component weights (see Section 3.4), determined as described above. The hydrostatic properties are then checked against stability criteria, including transverse and longitudinal hydrostatic stabilities. If the stability criterion is met, the baseline design is obtained. Otherwise, adjustments are made to the structural properties, and the design is iterated until stability requirements are fulfilled.

Chapter 3 will delve into individual aspects of the baseline design in greater detail.

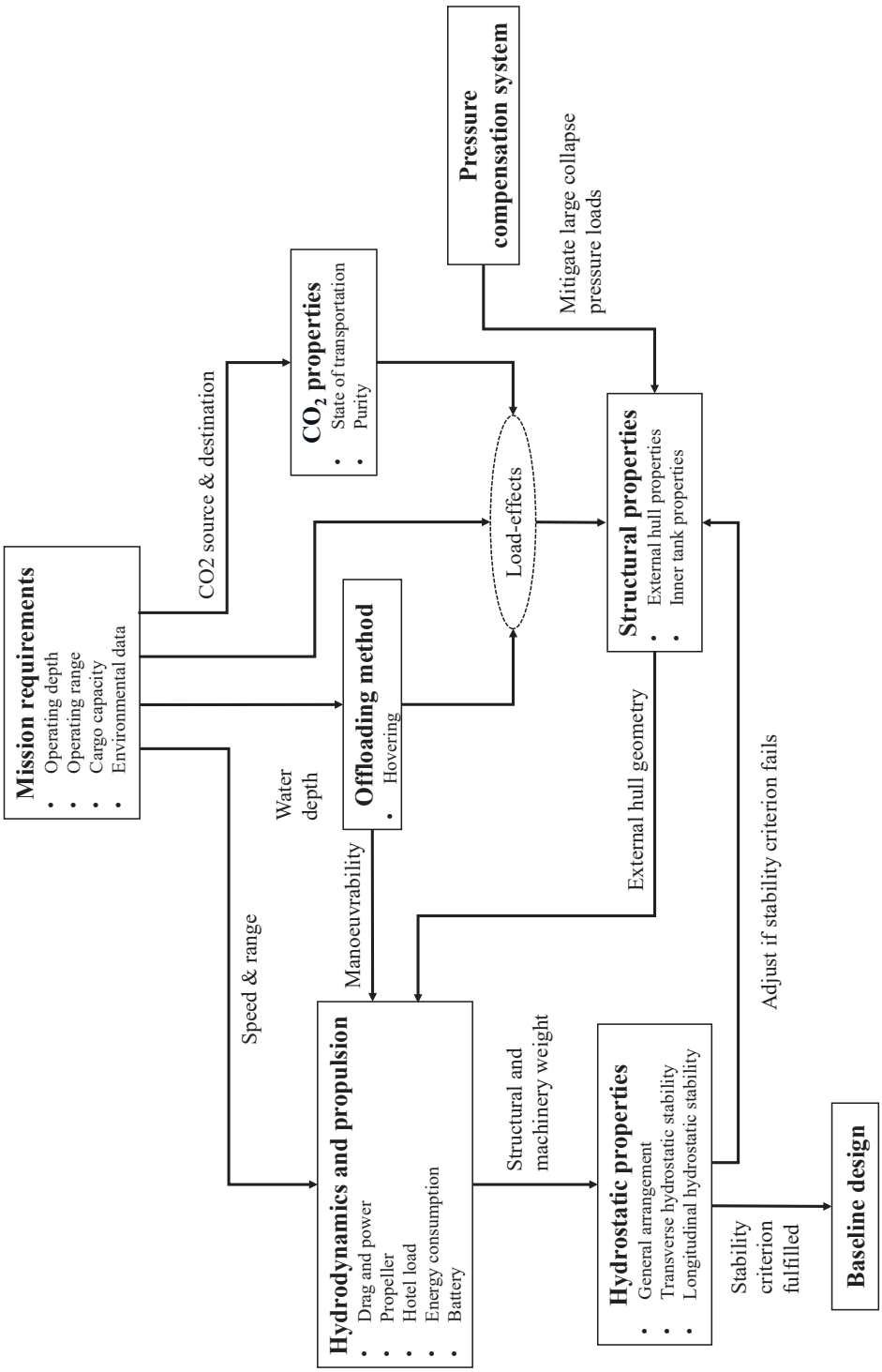

Figure 2.1: Flow chart of the design methodology of the baseline SST.

2.2 Manoeuvring Model Derivation

The SST manoeuvring model is implemented in the MATLAB Simulink environment [40]. The model is designed to be versatile and can be adapted to solve various problems, such as depth control [41, 42] and hovering [43, 44]. Instead of using a fully coupled 6 degrees of freedom (DoF) model, a decoupled 3 DoF planar model is proposed for the emergency recovery action, sufficient to represent the required manoeuvres. This approach aligns with Ross's findings [45], where a submersible can be decoupled into a longitudinal and a lateral subsystem. This subdivision applies to port-starboard symmetric slender bodies, including underwater robotics and submarines [46].

The coordinate system utilised for the manoeuvring analysis in this thesis follows a North-East-Down (NED) framework. This NED system originates from the Earth's reference point, while a body-fixed reference frame is positioned at the SST's centre of buoyancy (CoB). The coordinate system is presented in Figure 2.2.

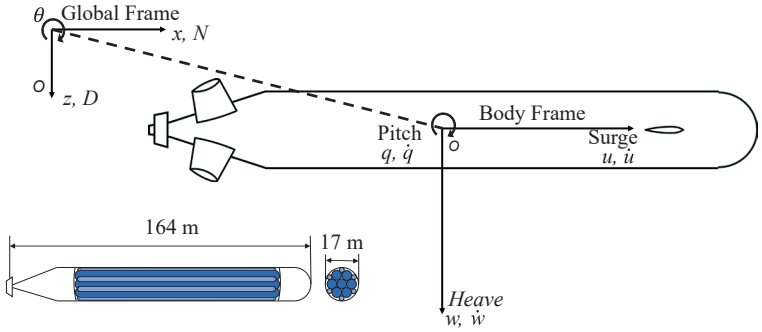

Figure 2.2: SST coordinate system demonstration.

2.2.1 Plant Model

Longitudinal subsystem equations of motion considering surge, heave, and pitch expressed as kinematic equations Eq. (2.1) and dynamic equations Eq. (2.2) in a vectorial format using Fossen notation

are presented as [47]:

$$\dot{\boldsymbol{\eta}} = \boldsymbol{J}_{\boldsymbol{\Theta}}(\boldsymbol{\eta})\boldsymbol{\nu} \tag{2.1}$$

$$\boldsymbol{M}\dot{\boldsymbol{\nu}} + \boldsymbol{C}_{\boldsymbol{c}}(\boldsymbol{\nu})\boldsymbol{\nu} + \boldsymbol{D}_{\boldsymbol{d}}(\boldsymbol{\nu})\boldsymbol{\nu} + \boldsymbol{g}(\boldsymbol{\eta}) = \boldsymbol{\tau} \tag{2.2}$$

where $\boldsymbol{\eta}$ is a vector consisting of NED position and Euler angles, $\boldsymbol{\nu}$ is the linear and angular velocity in the body-fixed system, $\boldsymbol{J}_{\boldsymbol{\Theta}}(\boldsymbol{\eta})$ is the Euler transformation matrix, $\boldsymbol{M}$ is system mass matrix consists of SST mass and added mass, $\boldsymbol{C}_{\boldsymbol{c}}(\boldsymbol{\nu})$ is the Coriolis-centripetal matrix, $\boldsymbol{D}_{\boldsymbol{d}}(\boldsymbol{\nu})$ is the damping matrix, $\boldsymbol{g}(\boldsymbol{\eta})$ is the force vector considering gravitational and buoyancy forces, $\boldsymbol{\tau}$ is the control force vector.

Expand Eq. (2.1) into the component form using the Euler angle representation:

$$\underbrace{\begin{bmatrix}\dot{N}\\ \dot{D}\\ \dot{\theta}\end{bmatrix}}_{\dot{\boldsymbol{\eta}}} = \underbrace{\begin{bmatrix}\cos\theta & \sin\theta & 0\\ -\sin\theta & \cos\theta & 0\\ 0 & 0 & 1\end{bmatrix}}_{\boldsymbol{J}_{\boldsymbol{\Theta}}(\boldsymbol{\eta})} \underbrace{\begin{bmatrix}u\\ w\\ q\end{bmatrix}}_{\boldsymbol{\nu}} \tag{2.3}$$

In Eq. (2.2), the mass matrix M, Coriolis-centripetal matrix $\boldsymbol{C}_{\boldsymbol{c}}(\boldsymbol{\nu})$, and damping matrix $\boldsymbol{D}_{\boldsymbol{d}}(\boldsymbol{\nu})$ are expressed as:

$$\boldsymbol{M} = \begin{bmatrix} m - X_{\dot{u}} & 0 & mz_g \\ 0 & m - Z_{\dot{w}} & -Z_{\dot{q}} \\ mz_g & M_{\dot{w}} & I_{yy} - M_{\dot{q}} \end{bmatrix} \tag{2.4}$$

$$\boldsymbol{C_c}\left(\boldsymbol{\nu}\right) = \begin{bmatrix} 0 & 0 & 0 \\ 0 & m - Z_{\dot{w}} & -\left(m - X_{\dot{u}}\right) u \\ 0 & \left(Z_{\dot{w}} - X_{\dot{u}}\right) & 0 \end{bmatrix} \tag{2.5}$$

$$\boldsymbol{D_d}\left(\boldsymbol{\nu}\right) = \begin{bmatrix} X_{|u|u}|u| & X_{wq}q & X_{qq}q \\ Z_{uq}q & Z_{|w|w} + Z_{uw}u & Z_{q|q|} \\ M_{uw}w & M_{|w|w} & M_{uq}u + M_{|q|q} \end{bmatrix} \tag{2.6}$$

where m is the SST mass and z_g is the location of the centre of gravity vertical (CoG) position.

2.2.2 Hydrodynamic derivatives

The applied hydrodynamic coefficients were estimated following Prestero's study on REMUS AUV [48].

Blevins (1979) [49] provided an empirical formula to estimate the added mass of an ellipsoid object. It is used to calculate the axial added mass $X_{\dot{u}}$:

$$X_{\dot{u}} = -\frac{4\alpha\pi\rho}{3}\left(\frac{L}{2}\right)\left(\frac{D}{2}\right)^2 \tag{2.7}$$

where $\alpha = 0.021$ is an empirical parameter, L is SST (object) length, D is SST diameter.

The added mass of a circular slice submerged in water can be calculated as [50]:

$$m_a(x) = \pi\rho R(x)^2 \tag{2.8}$$

where $R(x)$ is the cross-section radius.

The cross-flow added mass hydrodynamic coefficients are obtained from integrating the added mass of circular slices along the SST:

$$Z_{\dot{w}} = -\int_{x_{tail}}^{x_{bow}} m_a(x)dx \tag{2.9}$$

$$M_{\dot{w}} = \int_{x_{tail}}^{x_{bow}} x m_a(x)dx \tag{2.10}$$

$$Z_{\dot{q}} = M_{\dot{w}} \tag{2.11}$$

$$M_{\dot{q}} = \int_{x_{tail}}^{x_{bow}} x^2 m_a(x)dx \tag{2.12}$$

where x_{tail}=-75.3 m and x_{bow} = 88.7 m. They are the positions of the tail end and bow, respectively.

$$X_{|u|u} = -0.5\rho c_d A_f \tag{2.13}$$

c_d = 0.145 is the axial drag coefficient. The SST frontal projected area A_f=227.0 m^2.

The cross-flow damping terms are calculated by:

$$Z_{|w|w} = -0.5\rho c_{dc} \int_{x_{tail}}^{x_{bow}} 2R\left(x\right) dx \tag{2.14}$$

$$M_{|w|w} = 0.5\rho c_{dc} \int_{x_{tail}}^{x_{bow}} 2xR\left(x\right) dx \tag{2.15}$$

$$Z_{|q|q} = 0.5\rho c_{dc} \int_{x_{tail}}^{x_{bow}} 2x|x|R\left(x\right) dx \tag{2.16}$$

$$M_{|q|q} = -0.5\rho c_{dc} \int_{x_{tail}}^{x_{bow}} 2x^3 R\left(x\right) dx \tag{2.17}$$

where c_{dc}=1.1 is the a cylinder's cross-flow drag coefficient [51].

The rest cross-terms are calculated as:

$$X_{wq} = Z_{\dot{w}} \tag{2.18}$$

$$X_{qq} = Z_{\dot{q}} \tag{2.19}$$

$$Z_{uq} = -X_{\dot{u}} \tag{2.20}$$

$$M_{uq} = -Z_{\dot{q}} \tag{2.21}$$

$$M_{uw_a} = -\left(Z_{\dot{w}} - X_{\dot{u}}\right) \tag{2.22}$$

SST body lift Z_{uw} and lift-induced pitch moment M_{uw_l} hydrodynamic derivatives are obtained as:

$$Z_{uw} = -0.5\rho d^2 c_{yd\beta} \tag{2.23}$$

$$M_{uw_l} = -0.5\rho d^2 c_{yd\beta} x_{cp} \tag{2.24}$$

where $c_{yd\beta}$=0.003 is the lift slope coefficient [48] and x_{cp}=-31.6 m is the viscous force centre [51].

Finally, the total cross-term pitch moment hydrodynamic deriva-

tive is expressed as a summation of added mass contribution and body lift contribution:

$$M_{uw} = M_{uw_a} + M_{uw_l} \tag{2.25}$$

2.3 Control System Design

2.3.1 Proportional–Integral–Derivative (PID) Controller

The proportional-integral-derivative (PID) control is computed by taking into account that the error $e(t) = x_d - x$ is changing over time. The control input of a PID controller is computed as follows:

$$\mathbf{u}(t) = \mathbf{u}_{ff}(t) + \mathbf{K}\left(\mathbf{e}(t) + \frac{1}{T_i}\int_0^t \mathbf{e}(\tau)d\tau + T_d\dot{\mathbf{e}}(t)\right) \tag{2.26}$$

where $\mathbf{u}$ is the control input. $\mathbf{K}$ is the controller gain matrix. T_i; T_d > 0 are positive constants that give a different weight to the different parts.

2.3.2 Linear Quadratic Regulator (LQR)

The SST hovering control is addressed using the Linear Quadratic Regulator (LQR) [52]. LQR is an optimal full-state feedback controller that determines feedback gains to achieve specific optimality criteria for a given system. It optimises a cost function $\boldsymbol{L}(\boldsymbol{x}(t), \boldsymbol{u}(t))$ which includes a weighted combination of performance and controller effort. LQR has been successfully applied in various marine crafts, such as heading autopilots, rudder-roll damping systems, and dynamic positioning systems [47]. Mendes et al. [53] evaluated the waypoint tracking problem using both a Proportional-PID controller and an LQR. They found that LQR exhibited superior responsiveness compared to

PID. Tiwari and Sharma [54] also analysed the hovering control of an AUV with LQR, observing that it enabled the AUV to maintain desired depth with minimal undesired oscillations and low power consumption.

Optimal control is concerned with finding a control law for a given system to achieve a specific optimality criterion, typically represented by a cost function that depends on state and control variables. The optimal control law consists of differential equations that minimize the cost function and can be obtained through either Pontryagin's maximum principle (a necessary condition) or by solving the Hamilton–Jacobi–Bellman equation (a sufficient condition). For our discussion, we will focus on linear systems with quadratic cost functions, which fall under the category of linear quadratic (LQ) optimal control theory [55].

One fundamental design problem in this category is the regulator problem, which aims to regulate the system's outputs $\boldsymbol{y}$ to zero or a constant value while meeting specific time-response specifications. An LQR can be employed to address this. The LQR approach involves considering the state-space model and designing the control law accordingly.

$$\begin{aligned} \dot{\boldsymbol{x}} &= \boldsymbol{A}\boldsymbol{x} + \boldsymbol{B}\boldsymbol{u} \\ \boldsymbol{y} &= \boldsymbol{C}\boldsymbol{x} \end{aligned} \tag{2.27}$$

where $\boldsymbol{x} \in \Re^n$, $\boldsymbol{u} \in \Re^r$ and $\boldsymbol{y} \in \Re^m$. To design an LQR, the system ($\boldsymbol{A}$, $\boldsymbol{B}$ and $\boldsymbol{C}$) must be controllable and observable.

As an optimal control strategy, the state feedback control law for the system is found by optimising a quadratic cost function J [56]:

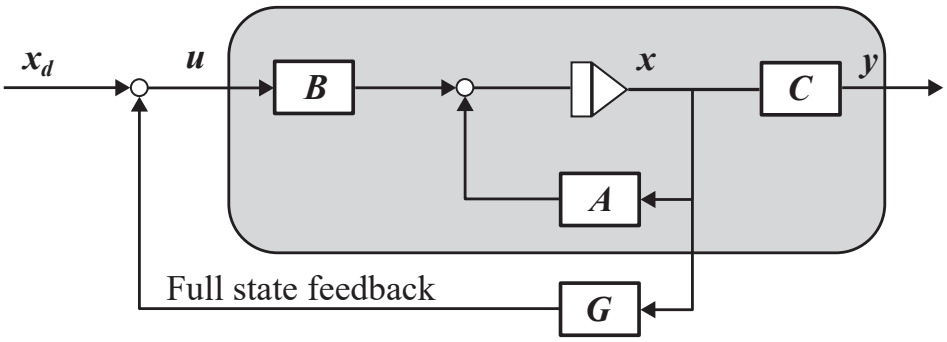

Figure 2.3: Block Diagram of the LQR.

$$\begin{aligned} J &= \min_{\boldsymbol{u}}\{\frac{1}{2}\int_0^T (\boldsymbol{y}^\intercal \boldsymbol{Q}\boldsymbol{y} + \boldsymbol{u}^\intercal \boldsymbol{R}\boldsymbol{u})dt \\ &= \frac{1}{2}\int_0^T (\boldsymbol{x}^\intercal \boldsymbol{C}^\intercal \boldsymbol{Q}\boldsymbol{C}\boldsymbol{x} + \boldsymbol{u}^\intercal \boldsymbol{R}\boldsymbol{u})dt\} \end{aligned} \tag{2.28}$$

where $\boldsymbol{Q}$ and $\boldsymbol{R}$ are state and effort weight matrices, respectively. They are both positively defined.

The steady-state solution of the system is [55]:

$$\begin{aligned} \boldsymbol{u} &= -\boldsymbol{R}^{-1}\boldsymbol{B}\boldsymbol{P}_\infty \boldsymbol{x} \\ &= \boldsymbol{G}\boldsymbol{x} \end{aligned} \tag{2.29}$$

where $\boldsymbol{G}$ is the gain matrix. $\boldsymbol{P}_\infty = \lim_{t\to\infty} \boldsymbol{P}(t)$ is a positively defined symmetric matrix obtained by solving the algebraic Riccati equation:

$$\boldsymbol{P}_\infty \boldsymbol{A} + \boldsymbol{A}^\intercal \boldsymbol{P}_\infty - \boldsymbol{P}_\infty \boldsymbol{B}\boldsymbol{R}^{-1}\boldsymbol{B}^\intercal \boldsymbol{P}_\infty + \boldsymbol{C}^\intercal \boldsymbol{Q}\boldsymbol{C} = \boldsymbol{o} \tag{2.30}$$

From Figure 2.3, the time derivative of the state can be calculated as:

$$\dot{\boldsymbol{x}} = (\boldsymbol{A} + \boldsymbol{B}\boldsymbol{G})\boldsymbol{x} \tag{2.31}$$

In this work, the LQR design can be achieved by the embedded Matlab function lqr [57].

2.3.3 Controllability

To design an LQR, it is essential for the system to possess controllability. This implies that both the linear state matrix $\boldsymbol{A}$ and the linear input matrix $\boldsymbol{B}$ must meet the controllability criteria, which signifies that the controllability matrix $\boldsymbol{Con}$ should have full row rank, in other words, it should possess a right inverse [58]. The controllability matrix is determined as Eq.(2.32):

$$\boldsymbol{Con} = \left[\boldsymbol{B}|\boldsymbol{AB}|\cdots|\boldsymbol{A}^{n-1}\boldsymbol{B}\right] \tag{2.32}$$

2.3.4 Luenberger Observer

Creating an LQR entails the application of a state variable feedback law, wherein an optimal control technique leverages the observation of all components of state variables to compute the control input [59]. One way to achieve such measurement is by implementing a Luenberger observer [60] to represent sensors and provide state measurements to the system. The Luenberger observer functions as a simple fixed-gain observer, reconstructing the estimated state $\hat{\boldsymbol{x}}$ from the control input $\boldsymbol{u}$ and system output $\boldsymbol{u}$. The estimated state vector $\hat{\boldsymbol{x}}$, instead of the actual state vector $\boldsymbol{x}$, is then employed as the state feedback to compute the control input for the next time step. The following differential equation can describe the continuous-time Luenberger observer:

$$\dot{\hat{\boldsymbol{x}}} = \boldsymbol{A}\hat{\boldsymbol{x}} + \boldsymbol{Bu} + \boldsymbol{K}_L + (\boldsymbol{y} - \hat{\boldsymbol{y}}) \tag{2.33}$$

where $\boldsymbol{K}_L$ is the observer gain, $\hat{\boldsymbol{y}}$ is the estimated output vector. The observer gain is obtained by placing the close loop poles on the negative side of the real axis.

2.3.5 Observability

The model must be observable to implement the Luenberger observer. The observability refers to the ability to estimate the real-time state $\boldsymbol{x}$ from the actuator input $\boldsymbol{u}$ and system output $\boldsymbol{y}$. Similar to the controllability matrix, the observability matrix $\boldsymbol{Obs}$ is a matrix that consists of the transpose of the state matrix $\boldsymbol{A}$ and the output matrix $\boldsymbol{C}$.

$$\boldsymbol{Obs} = \left[\boldsymbol{C}^\intercal | \boldsymbol{A}^\intercal \boldsymbol{C}^\intercal | \cdots | (\boldsymbol{A}^\intercal)^{n-1} \boldsymbol{C}^\intercal\right] \tag{2.34}$$

2.4 Extreme Value Predictions

2.4.1 Average Conditional Exceedance Rate Method

The Average Conditional Exceedance Rate (ACER) method is utilised in predicting and analysing extreme values and distributions. Introduced by Næss and Gaidai [61], this method involves constructing a series of non-parametric functions diverging from traditional asymptotic sample theory. ACER has been successfully applied to stationary and non-stationary stochastic processes, encompassing all global maximum peaks. Notably, ACER avoids the need for data declustering to ensure independence [62].

Traditionally, the Gumbel distribution is often appropriate in the context of marine structures' response processes [63]. However, the Gumbel distribution lacks an upper limit in its prediction, which can lead to over-conservatism and overprediction of extreme values in engineering problems. Xing et al. (2022) [64] conducted a comparative study between the ACER method and Gumbel when investigating the SST hovering problem under low current speed conditions with aft thruster failure. This study demonstrated the robustness of the ACER method in novel scenarios and highlighted its capability to estimate extreme values without relying on asymptotic assumptions.

Compared to other techniques for estimating extreme values, such as the Generalised Extreme Value distribution and the Peaks-Over-Threshold method, ACER stands out by not mandating that observations be independently and identically distributed. This means that each random variable doesn't affect others (independence), and all samples originate from the same distribution (identical). The ACER method employs non-parametric functions of various orders to approximate the actual extreme value distribution. The ACER method is concerned with determining the distribution function of the extreme value, denoted as $M_N = max\{X_j;\, j = 1,\ \cdots,\ N\}$. Precise estimation of $P_\eta = Prob\,(M_N \leq \eta)$ is sought for large values of η. This probability, denoted as P_η, represents the likelihood of the extreme value η occurring, and it follows:

$$P_\eta = Prob\,(M_N \leq \eta) = Prob\,(X_1 \leq \eta,\ \cdots,\ X_N \leq \eta) \tag{2.35}$$

A succession of conditional approximation $P_k(\eta)$ is used to solve Eq. (2.35). where $P_k(\eta)$ tends to be close to P_η as k increases. For $N \gg 1$ and $k = 1, 2,\ \cdots, P_k(\eta)$ is represented as [61]:

$$P_k\,(\eta) \approx exp(-\sum_{j=k}^{N} \alpha_{kj}(\eta)) \tag{2.36}$$

where $\alpha_{kj}\,(\eta) = Prob\,(X_1 > \eta | X_{j-1} \ll \eta,\ \cdots,\ X_{j-k+1} \leq \eta)$ and it represents the exceedance probability (only counted if proceeded by non-exceedances). The notion described in Eq. 2.36 and will be calculated by ACER as follows:

$$\varepsilon_k\,(\eta) = \frac{1}{N-k+1} \sum_{j=k}^{N} \alpha_{kj}\,(\eta), k = 1, 2, \cdots \tag{2.37}$$

where N represents the number of sample points for a specific moment X_n. For $k \geq 2$, $\widetilde{\varepsilon}_k(\eta)$ is used instead of $\varepsilon_k(\eta)$, as it is easier to use

for non-stationary or long-term statistics [63], and it is calculated as:

$$\widetilde{\varepsilon}_k(\eta) = \lim_{N\to\infty} \frac{\sum_{j=k}^{N} a_{kj}(\eta)}{N-k+1} \tag{2.38}$$

where

$$\lim_{N\to\infty} \frac{\widetilde{\varepsilon}_k(\eta)}{\varepsilon_k(\eta)} = 1 \tag{2.39}$$

The ACER (for both stationary and non-stationary time series) sample is estimated as:

$$\hat{\varepsilon}_k(\eta) = \frac{1}{R}\sum_{r=1}^{R} \hat{\varepsilon}_k^{(r)}(\eta) \tag{2.40}$$

where R is the number of samples or realisations.

$$\hat{\varepsilon}_k^{(r)}(\eta) = \frac{\sum_{j=k}^{N} a_{kj}{}^{(r)}(\eta)}{N-k+1} \tag{2.41}$$

where r denotes the specific realisation number.

When sufficient and independent numbers of realisations are achieved, the 95% confidence interval (CI) for the $\varepsilon_k(\eta)$ can be estimated as:

$$CI(\eta) = \hat{\varepsilon}_k(\eta) \pm \frac{1.96\hat{s}_k(\eta)}{\sqrt{R}} \tag{2.42}$$

where $\hat{s}_k(\eta)$ refers to the standard deviation of samples and can be estimated by:

$$\hat{s}_k(\eta)^{\,2} = \frac{1}{R-1}\sum_{r=1}^{R} \left(\hat{\varepsilon}_k^{(r)}(\eta) - \hat{\varepsilon}_k(\eta)\right)^2 \tag{2.43}$$

The above equations for estimating the average exceedance rate are based on direct numerical simulations. In contrast, an extrapolation technique can reduce the computational time. Assuming the mean exceedance rate in the tail behaves similarly to $exp\{-a(\eta-b)^c\}$ $(\eta \geq$

$\eta_0 \geq b$) where a, b and c are suitable constants. The ACER will therefore be assumed by:

$$\varepsilon_k(\eta) \approx q_k(\eta)\, exp\left\{-a_k(\eta - b_k)^{c_k}\right\} \tag{2.44}$$

where $\eta \geq \eta_1 \geq b_k$ and the function $q_k(\eta)$ varies slowly compared to the exponential function $exp\left\{-a_k(\eta - b_k)^{c_k}\right\}$ in the tail region. Continuously, this can be replaced by a constant for a fitting choice of the tail marker η_0. In the end, the Levenberg-Marquardt least-squares optimisation method can be used to determine the constants a_k, b_k, c_k and q_k. Næss and Gaidai (2009) [61] expressed their experience that this damped least-squares method is well suited for this assignment. Chai et al. (2018) [65] concluded that the extrapolation scheme applied to capture the tail behaviour of the ACER functions was satisfactory for the extreme value predictions.

2.5 RANS $k-\omega$ SST Modelling

The governing equation of the 3D steady RANS equations are expressed as:

$$\frac{\partial \overline{u_i}}{\partial x_i} = 0 \tag{2.45}$$

$$\overline{u_j}\frac{\partial \overline{u_i}}{\partial x_j} = -\frac{1}{\rho}\frac{\partial \overline{p}}{\partial x_i} + \nu\frac{\partial^2 \overline{u_i}}{\partial x_j \partial x_j} - \frac{\partial \overline{u_i\prime u_j\prime}}{\partial x_j} \tag{2.46}$$

where i, j=1,2,3 and denote the directions. Overline ($\bar{}$) represents the Reynolds average of the physical variables; x_i and x_j are the spatial directions, while $\overline{u_i}$ and $\overline{u_j}$ are the corresponding Reynolds averaged velocity components; $\overline{u_i\prime u_j\prime}$ represents the Reynolds stress which is the Reynolds averaged value of the product of velocity fluctuations $u_i\prime$ and $u_j\prime$; ν is the kinematic viscosity; ρ is the fluid density.

The $k-\omega$ shear stress transport ($k-\omega$ SST) model [66] is used in

Chapter 8 to resolve the unknown Reynolds stress tensor. The $k-\omega$ SST model combines the $k-\varepsilon$ [67] and $k-\omega$ [68] models by using two blending functions F_1 and F_2. It applies the $k-\omega$ model as a low Re model close to the wall in the viscous sub-layer due to its better performance in predicting flow separation. The standard $k-\varepsilon$ model, which is less sensitive to the freestream inlet turbulence, is used in the outer free stream region. The dissipation rate equation and turbulence kinetic energy equation, according to Menter's updated model formulation [69], are expressed as:

$$\begin{aligned}\frac{D}{Dt}(\rho\omega) =& \alpha\rho\, S^2 - \beta\rho\omega^2 + \frac{\partial}{\partial x_j}\left[(\mu+\sigma_\omega\mu_t)\frac{\partial\omega}{\partial x_j}\right] \\ &+ 2(1-F_1)\,\rho\sigma_{\omega 2}\frac{1}{\omega}\frac{\partial k}{\partial x_j}\frac{\partial\omega}{\partial x_j}\end{aligned} \tag{2.47}$$

$$\frac{D}{Dt}(\rho k) = \widetilde{P}_k - \beta^*\rho\, k\omega + \frac{\partial}{\partial x_j}\left[(\mu+\sigma_k\mu_t)\frac{\partial k}{\partial x_j}\right] \tag{2.48}$$

where the first blending function F_1 is:

$$F_1 = \tanh\left\{\left\{\min\left[\max\left(\frac{\sqrt{k}}{\beta^*\omega y_w}, \frac{500\nu}{y_w^2\omega}\right), \frac{4\rho\sigma_{\omega 2}k}{CD_{k\omega}y_w^2}\right]\right\}\right\} \tag{2.49}$$

$$CD_{k\omega} = \max\left(2\rho\sigma_{\omega 2}\frac{1}{\omega}\frac{\partial k}{\partial x_j}\frac{\partial\omega}{\partial x_j}, 10^{-10}\right) \tag{2.50}$$

where y_w is the distance to the wall and $CD_{k\omega}$ is the positive part of the cross-diffusion term. $F_1 = 0$ to activate the $k-\varepsilon$ model in the wake region and $F_1 = 1$ inside the boundary layer to switch to the $k-\omega$ model.

Moreover, the production limiter term avoids turbulence build-up in the stagnation region.

$$\widetilde{P}_k = \min\left[\mu_t \frac{\partial U_i}{\partial x_j}\left(\frac{\partial U_i}{\partial x_j} + \frac{\partial U_j}{\partial x_i}\right), 10\beta^* \rho k\omega\right] \tag{2.51}$$

The turbulent eddy viscosity ν_t is expressed as:

$$\nu_t = \frac{a_1 k}{\max\left(a_1\omega, SF_2\right)} \tag{2.52}$$

where S is the invariant of the strain rate. F_2 is the second blending function and is expressed as:

$$F_2 = \tanh\left[\left[\max\left(\frac{2\sqrt{k}}{\beta^*\omega y_w}, \frac{500\nu}{y_w^2\omega}\right)\right]^2\right] \tag{2.53}$$

where in the equations above, constants α, β, σ_ω and σ_k are computed from the corresponding constants in the $k-\varepsilon$ and $k-\omega$ models following Eq. 2.54. In Eq. 2.54, α is an example, but the same principle applies to β, σ_ω and σ_k.

$$\alpha = \alpha_1 F_1 + \alpha_2\left(1 - F_1\right) \tag{2.54}$$

The constants in the model are: $\beta^* = 0.09$, $\alpha_1 = 5/9$, $\alpha_2 = 0.44$, $\beta_1 = 3/40$, $\beta_2 = 0.828$, $\sigma_{\omega 1} = 0.5$, $\sigma_{\omega 2} = 0.856$, $\sigma_{k1} = 0.85$ and $\sigma_{k2} = 1$.

Chapter 3

SST Baseline Design

3.1 Baseline SST Main Parameters

The key parameters of the baseline design have been detailed in [23] and are summarised in Table 3.1. These parameters, established following the design procedure clarified in Section 3.1, characterise the SST as a 33,619-ton submarine featuring dimensions of 164 meters in length and 17 metres in beam. Its cargo capacity extends to 16,362 m^3 of CO_2, with an operational range of up to 400 km while cruising at 6 knots.

3.2 SST Mission Requirements

Defining mission requirements is essential for establishing the design premises and is discussed in this section.

3.2.1 Operating Depth Range:

The SST is defined with the following depth specifications:

- **Safety Depth**: 40 m. The safety depth is the minimum diving depth that prevents collisions with surface ships or floating installations.

Table 3.1: Summary of the main design parameters of the baseline design of the SST [23]. Detailed design configurations are presented later in this chapter.

Parameter	Value	Unit
Length	164	[m]
Beam	17	[m]
Displacement	33,619	[tonnes]
Collapse depth	190	[m]
Operating depth	70	[m]
Operating speed	6	[knots]
Maximum range	400	[km]
Cargo volume	16,362	[m^3]
Current speed	1	[m/s]
Cargo pressure	35 - 55	[bar]
Cargo temperature	0-20	[°C]

- **Nominal Diving Depth**: 70 m. The SST is designed to operate at a constant 70 m depth. Appendix A provides the determination process for the nominal diving depth.
- **Test Diving Depth**: 105 m. The SST's test diving depth is 105 m, 1.5 times the nominal diving depth, following DNVGL-RU-NAVAL-Pt4Ch1, Table 1 [70].
- **Collapse Depth**: 190 m. The SST is designed not to collapse at depths up to 190 m, 2.7 times the nominal diving depth, following DNVGL-RU-NAVAL-Pt4Ch1, Table 1 [70].

In accordance with these explanations, the operational depth range of the SST spans from 40 metres (considered as the safety depth) to 70 metres (defined as the nominal diving depth). In the event that the hydrostatic pressure surpasses the tank pressure, necessitating measures to avert cargo tank failure, emergency procedures employing the pressure compensation system (PCS) will be initiated (as detailed in Section 3.8). Figure 3.1 provides a visual representation of these depth definitions in relation to the depths of the CCS storage sites under con-

sideration in this investigation.

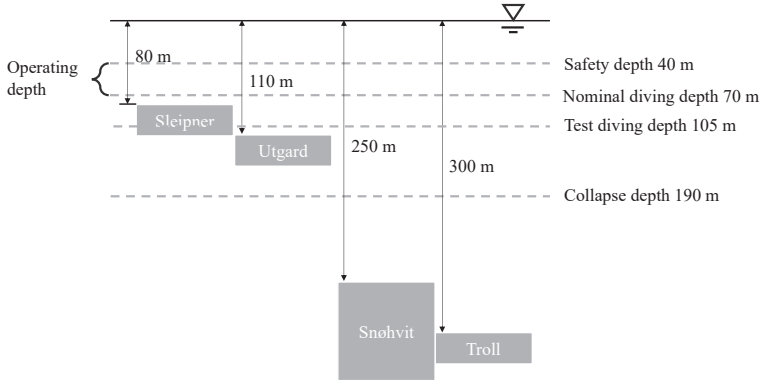

Figure 3.1: Important depth ranges for SST operation. Existing offshore carbon storage sites shown in Figure 1.3 are also included.

3.2.2 Voyage Range

The SST is engineered to encompass a 400 km operational range, affording it the capability to undertake a round-trip voyage to Snøhvit and Troll, or, alternatively, a unidirectional journey to Sleipner and Utgard. In the latter scenario, the SST has the potential to be charged using the pre-existing offshore infrastructure situated at the Utsira High, which is powered from the mainland.

3.2.3 Cargo Capacity

The SST's cargo capacity is established at 15,000 tonnes, matching the maximum annual carbon storage capacity of the CCS projects under examination in this research, which amounts to 1.5 million tonnes (as indicated in Figure 1.3) [5, 6]. Achieving this capacity is attainable through a bi-weekly scheduling of SST voyages.

3.2.4 Environmental Data:

The following environmental conditions are defined:

- Design minimum and maximum environmental temperatures: 0 °C and 20 °C, respectively.
  - The SST will operate in the Norwegian Sea (0 °E - 10 °E, 60 °N - 70 °N), where seawater temperatures range from 2 °C to 12 °C (NCEI 2020). The minimum temperature of 0 °C accounts for a slight temperature margin during winters, as seawater temperatures typically do not fall below 0 °C. The maximum temperature of 20 °C allows for surface operations during summers.
- Design seawater density: 1,025 kg/m^3.
  - This corresponds to the minimum seawater density based on the specified seawater temperatures. A conservative minimum density value ensures sufficient buoyancy force during neutral-buoyancy design calculations. An insufficient buoyancy force during the later stages of the design or construction process could result in costly vessel lengthening.
- Design current speed: 1 m/s.
  - In the Norwegian Sea, the observed seasonal average current speed is around 0.2 m/s, while the highest seasonal average speed is approximately 1 m/s for the North Atlantic Current and Norwegian coastal current [71–73].

3.3 CO_2 Transportation Consideration

The preliminary consideration of CO_2 transportation is discussed in this section. A more detailed evaluation is presented in Chapter 4.

3.3.1 State of Transportation

CO_2 transportation typically involves either the supercritical or saturated liquid states, using pipelines and ships, respectively. The SST employs the saturated liquid state for CO_2 transport, maintaining a pressure and temperature range of 35 - 55 bar and 0 - 20 °C, respectively. In this state, the environment passively regulates temperature and pressure, eliminating the need for external energy to maintain set points. Consequently, the pressure of the liquid CO_2 varies along the boiling line during transportation, making it an energy-efficient and cost-effective solution.

This approach differs from existing gas carriers, where semi-refrigerated and refrigerated types require re-liquefaction systems, which are both cost- and energy-intensive to operate. These carriers must maintain low temperatures of -50 °C and -15 °C, respectively (will be discussed later in Chapter 4). To achieve this, re-liquefaction systems with compressors capture the boil-off gas [35]. By transporting saturated liquid CO_2 at environmental temperatures, the SST avoids using these energy-intensive systems.

Additionally, at 45 bar, the liquid CO_2 can be directly injected into the reservoir using a single-stage booster pump (wellhead pressures are approximately 80 bar in Sleipner & Utgard). This approach is notably more efficient than gas carriers, which necessitate multi-stage booster pumps and inter-heaters to elevate the pressure from 8 bar to 80 bar and raise the temperature from -15 °C to 25 °C.

3.3.2 Purity

CO_2 purity is a critical consideration for the SST's structural design, as impurities can lead to corrosion and hydrate formation risks. The most undesirable impurity for the SST is free water (H_2O). Free water dissolves CO_2 and H_2S, forming highly corrosive carbonic and sulphuric acids, with the latter formed together with oxygen [74, 75].

These acids can cause severe corrosion issues in the SST. Additionally, hydrate formation in the cargo tanks may result in blockages and sealing problems, particularly affecting the seals in the pistons of the PCS (Ref. Section 3.8).

Table 3.2: CO_2 impurity limits for storage. Limits from the Northern Lights project are used [23].

Component	SST allowable (Northern Lights)
Water, H_2O	30 ppm
Sulphur oxides, SO_x	10 ppm
Nitrogen oxides, NO_x	10 ppm
Hydrogen sulphide, H_xS	9 ppm
Carbon monoxide, CO	100 ppm
Oxygen, O_2	10 ppm
Amines	10 ppm
Ammonia, NH_3	10 ppm
Hydrogen, H_2	50 ppm
Formaldehyde, HCHO	20 ppm
Acetaldehyde, CH_3CHO	20 ppm

To avoid free water in the SST, measures are taken to ensure that the water concentration remains lower than its solubility, meaning that all water dissolves in CO_2, leaving no free water. The baseline design adheres to impurity limits from the Northern Lights project [76], as the baseline SST is intended to operate in the Norwegian sector. These impurity limits, presented in Table 3.2, set the free water limit at 30 ppm, significantly lower than the lowest solubilities of H_2O presented in Xing et al. (2021) [19], i.e., 200 ppm and 1200 ppm considering CO_2 gas and liquid at -10 °C, respectively. This ensures that no free water will be present in the CO_2 cargo. Note that certain limits are placed on nitrogen oxides (NO_x), sulphur oxides (SO_x), and hydrogen sulphide (H_2S) in the Northern Lights project due to safety and health considerations, which may not be mandatory for the uncrewed SST.

3.4 General Arrangement

3.4.1 Compartments

The general arrangement of the SST, depicted in Figure 3.2, consists of three compartments separated by two watertight bulkheads:

- **Free flooding aft compartment:** This compartment houses moisture-sensitive equipment, including the motor, gearbox, rudder controls, battery, aft trim tank, and aft compensation tank.
- **Free flooding bow compartment:** Sensors, sonar, radio, control station, offloading pumps, fwd trim tank, and fwd compensation tank are located in this compartment.
- **Flooded mid-body:** The largest compartment, containing buoyancy tanks, cargo tanks, and piping.

3.4.2 Distribution of Weights and Spaces

Table 3.3 provides details of the weights, volumes, and centres of gravity (CoG) for the major components of the SST. The coordinate system's origin is set at the centroid of the cylindrical mid-body. To check the disposition of volumes, the Flounder diagram (Figure 3.3) is employed, representing the spatial distribution of the SST along its length without considering the exact layout. Each area in the diagram signifies the space requirement of the corresponding volume component.

The following components are defined:

- **Compensation Tanks:** Two 800.0 m^3 compensation tanks are equipped on the SST, providing trimming moment and weight for

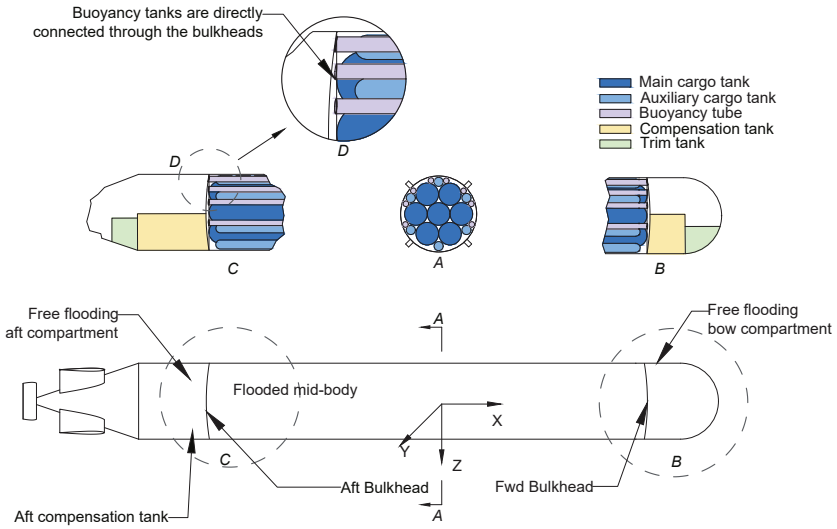

Figure 3.2: SST general arrangement. A: mid-vessel cross-section. B: front bulkhead. C: aft bulkhead. D: Buoyancy tank-bulkhead connections.

neutral buoyancy under different hydrostatic load cases. Their capacity is determined in accordance with Burcher and Rydill (1994) [15] and ensures neutral buoyancy under all design hydrostatic load cases.

- **Trim Tanks:** Two 200.0 m^3 trim tanks in the bow hemisphere and aft cone bring the CoG vertically beneath the centre of buoyancy (CoB) for neutral trim. They achieve this by pumping water between each other and need to be in communication with the open sea.

- **Permanent Ballast:** Used to assist in achieving neutral buoy-

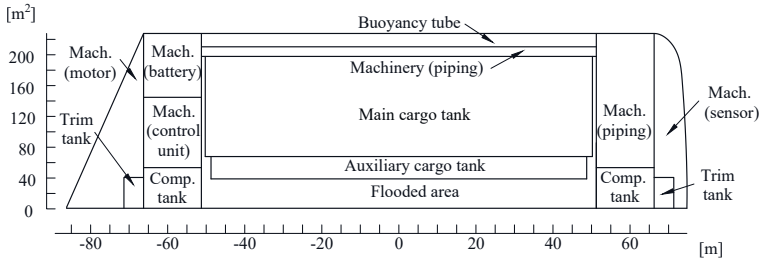

Figure 3.3: Flounder diagram of the SST. The lateral axis presents the longitudinal position on the SST; the vertical axis is the cross-section area.

ancy, equalise the longitudinal position of the centre of gravity and centre of buoyancy for neutral trim and increase hydrostatic stability. The estimated weight is 4% of the SST's dry weight, approximately 997 tonnes.

- **Machinery:** Estimated to be 1,000 tonnes, the machinery includes moisture-sensitive equipment and piping. The USS Albacore, with similar power levels to the SST (below 2 MW), has machinery weighing 638 tonnes [15].

Table 3.3: SST tank arrangement.

Component	CoG (x, y, z) [m]	Weight [ton]	Space [m³]	Component	CoG (x, y, z) [m]	Weight [ton]	Space [m³]
External hull	(-7.1, 0.0,0.0)	2,666	32,799	Buoyancy tank 4	(0.0, -1.9, -7.5)	46	123
Main cargo tank 1	(0.0, 0.0, 0.0)	681	1,931	Buoyancy tank 5	(0.0, 1.9, -7.5)	46	123
Main cargo tank 2	(0.0, 5.0, 0.0)	681	1,931	Buoyancy tank 6	(0.0, 5.6, -5.4)	46	123
Main cargo tank 3	(0.0, 2.5, 4.3)	681	1,931	Buoyancy tank 7	(0.0, 7.5, -2.1)	46	123
Main cargo tank 4	(0.0, -2.5, 4.3)	681	1,931	Buoyancy tank 8	(0.0, 7.5, 2.1)	46	123
Main cargo tank 5	(0.0, -5.0, 0.0)	681	1,931	Fwd comp. tank	(65.3, 0.0, 5.0)	100	800
Main cargo tank 6	(0.0, -2.5, -4.3)	681	1,931	Aft comp. tank	(-65.3, 0.0, 5.0)	100	800
Main cargo tank 7	(0.0, 2.5, -4.3)	681	1,931	Fwd trim tank	(67.8, 0.0, 5.0)	35	200
Auxi. cargo tank 1	(0.0, -7.1, 0.0)	171	475	Aft trim tank	(-67.8, 0.0, 5.0)	35	200
Auxi. cargo tank 2	(0.0, 6.2, -3.6)	171	475	Fwd bulkhead (watertight)	(50.0, 0.0, 0.0)	147	-
Auxi. cargo tank 3	(0.0, 6.2, 3.6)	171	475	Aft bulkhead (watertight)	(-50.0, 0.0, 0.0)	147	-
Auxi. cargo tank 4	(0.0, 7.1, 0.0)	171	475	Mid-body bulkhead 1	(25.0, 0.0, 0.0)	10	-
Auxi. cargo tank 5	(0.0, -6.2, 3.6)	171	475	Mid-body bulkhead 2	(25.0, 0.0, 0.0)	10	-
Auxi. cargo tank 6	(0.0, -6.2, -3.6)	171	475	Machinery	(-33.7, 0.0, 6.0)	1,000	8,288
Buoyancy tank 1	(0.0, -7.5, 2.1)	46	123	Permanent ballast	(4, 0.0, 8.0)	997	-
Buoyancy tank 2	(0.0, -7.5, -2.1)	46	123	Sum	(-4.6, 0.0, 0.9)	11,200	32,799
Buoyancy tank 3	(0.0, -5.6, -5.4)	46	123				

3.5 Hydrostatics

3.5.1 Hydrostatic Load Cases

The SST's hydrostatic stability is assessed according to DNVGL-RU-NAVAL-Pt4Ch1, Section 3.5.2.3 [70], which requires a minimum distance between the centres of buoyancy and gravity (BG) and a minimum metacentric height (GM) for vessels exceeding 2,000 DWT. The BG must be greater than 0.35 m during submerged, and the GM must be greater than 0.22 m in the surfaced condition. The hydrostatic load cases are detailed in Figure 3.4 and described as follows:

- **Submerged (CO_2 filled):** The SST is fully submerged with all 13 tanks filled with liquid CO_2, and the mid-body flooding area is filled with seawater. Compensation tanks ensure neutral buoyancy under this fully loaded condition.
- **Submerged (SW filled):** The SST is submerged with all 13 tanks filled with seawater, and seawater ballast fills the mid-body flooding area. Compensation tanks remain empty. This occurs after offloading at a subsea well.
- **Surfaced (CO_2 filled):** The SST floats on the surface with all 13 tanks filled with liquid CO_2, and the mid-body flooding area is not filled with seawater. Compensation tanks are empty. This situation arises during loading at the port.
- **Surfaced (SW filled):** The SST floats on the surface with five main tanks and three auxiliary tanks filled with seawater ballast at the bottom while the remaining tanks are empty. The mid-body flooding area is not filled with seawater. Compensation tanks are empty. This occurs when the SST returns to the port after its operation.

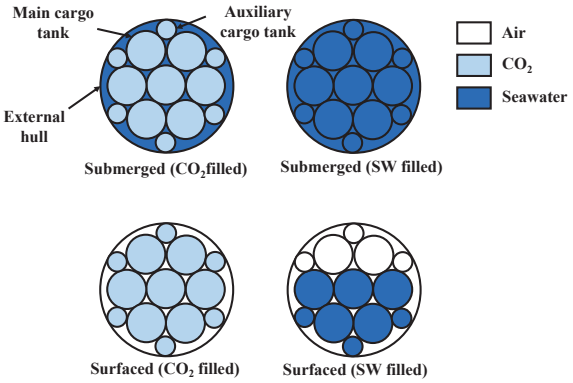

Figure 3.4: Illustration of the cargo tank cross-sectional views of liquid distributions for given hydrostatic load cases.

Table 3.4: Hydrostatic stability check of the baseline SST.

	Submerged (CO_2 filled)	Submerged (SW filled)	Surfaced (CO_2 filled)	Surfaced (SW filled)
CoB (x, y, z) [m]	(-1.43, 0.00, 0.00)	(-1.43, 0.00, 0.00)	(-1.75,0.00,1.36)	(-1.78, 0.00, 2.18)
CoG (x, y, z) [m]	(-1.43, 0.00, 0.78)	(-1.43, 0.00, 0.57)	(-1.75, 0.00, 0.50)	(-1.78, 0.00, 1.35)
M (x, y, z) [m]	(0.00, 0.00, 0.00)	(0.00, 0.00, 0.00)	(0.00, 0.00, 0.00)	(0.00, 0.00, 0.00)
GM [m]	0.78	0.57	0.50	1.35
BG [m]	0.78	0.57	-0.86	-0.83
Result	BG > 0.35 m, OK	BG > 0.35 m, OK	GM > 0.22 m, OK	GM > 0.22 m, OK

3.5.2 Metacentres and centres of buoyancy and gravity

The metacentre (M), CoB, and CoG for the SST under different hydrostatic load cases are tabulated in Table 3.4. These values affect the hydrostatic stability, as represented by BG and GM when the SST is submerged and floating, respectively. The lowest BG and GM values are 0.57 m and 0.50 m, respectively, and satisfy the criteria of 0.35 m and 0.22 m from DNVGL-RU-NAVAL-Pt4Ch1, Section 3.5.2.3 [70].

3.5.3 Weight and Space Composition

Table 3.5 presents the weight and space composition with respect to the designed hydrostatic load cases. The SST's dry weight composition is provided in Table 3.6. The double hull design and pure electric propulsion system contribute to a structural weight of 35% and machinery weight of 3% of the dry weight, respectively, enabling a high payload capacity of 46% of its displacement and 50% of its volume.

Table 3.5: Weight and space components of the baseline SST. Sub: submerged; Surf: surfaced; SW: cargo tank filled with seawater; CO_2: cargo tank filled with liquid CO_2

Component	Weight (tonnes)				Space [m^3]
	Sub (CO_2)	Sub (SW)	Surf (CO_2)	Surf (SW)	
Cargo tank	15,381 (46 %)	16,772 (49 %)	15,381 (57 %)	11,354 (50 %)	16,362 (50%)
Structure	9,413 (28%)	9,413 (28%)	9,413 (35%)	9,413 (41%)	1,169 (4%)
Machinery	1,000 (3%)	1,000 (3%)	1,000 (3%)	1,000 (3%)	8,288 (26%)
Mid-body seawater	5,152 (15%)	5,152 (15%)	0 (0%)	0 (0%)	5,027 (15%)
Compensation ballast	1,469 (4%)	1,469 (4%)	0 (0%)	0 (0%)	1,600 (4%)
Trim ballast	205 (1%)	205 (1%)	205 (1%)	205 (1%)	400 (1%)
Permanent ballast	997 (3%)	997 (4%)	997 (4%)	997 (4%)	-
Sum	33,619 (100%)	33,619 (100%)	26,996 (100%)	22,969 (100%)	32,799 (100%)

3.5.4 Equilibrium Polygon

During CO_2 offloading, seawater is pumped into one side of the cargo tank to displace CO_2 from the other end, causing changes in the longitudinal CoG positions and individual cargo tank weights due to the different densities of CO_2 (940 kg/m^3) and seawater (1,025 kg/m^3). This affects the global SST's longitudinal stability and weight. Eight cargo tank loading conditions are studied and listed in Table 3.7, with their corresponding equilibrium polygon plot in Figure 3.5. The equilibrium polygon shows the maximum compensating ballast weight and trimming moment achievable through compensation and trim tanks. All load cases lie within the polygon, indicating that the SST remains longitudinally stable, with sufficient trimming moments for stability in all conditions. Additionally, the x and y values of each point repre-

Table 3.6: SST dry weight composition.

Component	SST [tonnes]	SST [% dry weight]
Payload	15,381	57
Structure	9,413	35
Machinery	1,000	4
Permanent ballast	997	4
Total dry weight	26,791	100

Table 3.7: Cargo tank loading conditions considered in hydrostatic longitudinal stability check. In percentage of cargo tank volume.

Cargo tank loading condition	Liquid in the forward side of the tank	Liquid in the aft side of the tank
C0W100	100% SW	-
C30W70	30% CO_2	70% SW
C50W50	50% CO_2	50% SW
C70W30	70% CO_2	30% SW
C100W0	100% CO_2	-
W70C30	70% SW	30% CO_2
W50C50	50% SW	50% CO_2
W30C70	30% SW	70% CO_2

sent the required trimming moment for neutral trim and the required ballast for neutral buoyancy, respectively. The largest trimming moment occurs when the SST is 50% offloaded, and the most significant weight change occurs when the SST is 100% offloaded.

3.6 Structural Properties

3.6.1 External Hull Structural Design

Slenderness Ratio

The geometric properties of the external hull of the SST are summarised in Table 3.8 and briefly discussed in this section. The SST employs a torpedo-shaped hull design featuring a hemispherical bow, a 130.5 m long cylindrical mid-body section, and a 25 m long conical

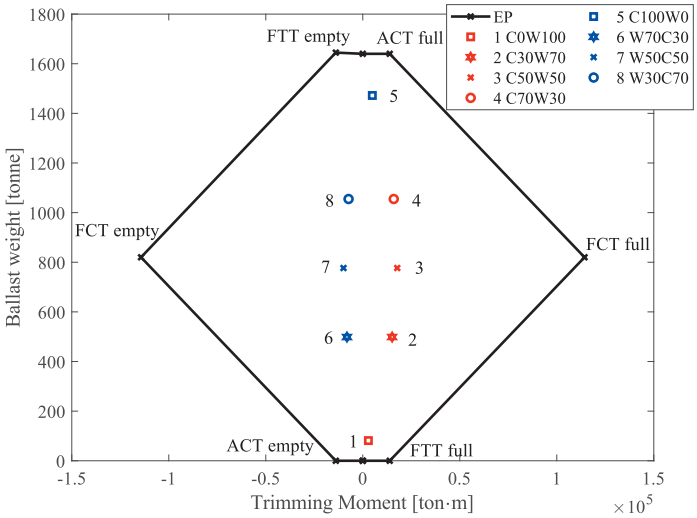

Figure 3.5: The Equilibrium polygon of the baseline SST. Cases are specified in Table 3.7. Abbreviations in the figure are: EP - equilibrium polygon, LC - loading condition, FTT - fwd trim tank, FCT - fwd compensation tank, ATT - aft trim tank, ACT - aft compensation tank.

aft. The hull has a diameter of 17 m. The choice of a torpedo shape is based on its simple geometry and low drag resistance, which enhances the vessel's hydrodynamic efficiency. The design's simplicity is advantageous because the cylindrical mid-body section requires steel plates bent in a single direction, making fabrication relatively straightforward. In contrast, plates bent in two directions are more complex to fabricate accurately. Although the bow and aft portions of the hull have curvatures in two directions and necessitate doubly bent plates, they contribute only 23% of the total steel external hull weight. However, they are crucial in achieving low drag resistance. The cylindrical mid-body section's design also facilitates the efficient arrangement of cargo tanks inside the hull, maximising the vessel's cargo capacity. Moreover, the slenderness ratio of the vessel, chosen to be 9.7, results in a drag resistance value that is very close to the theoretical minimum, with just about 5% more resistance than the minimum value associ-

ated with a slenderness value of 5.7. The plot of total resistance against the slenderness ratio, shown in Figure 3.6, illustrates this behaviour. Detailed calculations supporting the plot are provided in Appendix B.

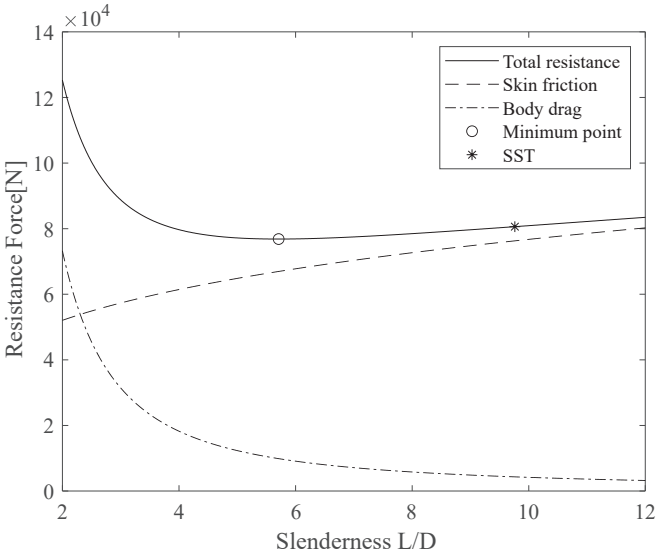

Figure 3.6: Total resistance of the streamlined body as a function of its slenderness ratio with a fixed displacement.

Hull Structural Properties

Designing large submarines to withstand collapse in deep waters presents significant challenges and costs. Large-diameter, thin-walled structures used in submarines are susceptible to geometric imperfections, which are difficult to control in large structures where steel plates and beams are welded together. As mentioned in Section 1.1.3, even a tiny imperfection of 1% in the diameter can lead to a 50% reduction in the collapse pressure capacity [22]. To achieve the required collapse capacities in deep waters, large military submarines often resort to heavy and closely spaced ring-stiffened structures and high-strength steels in their external hulls [77]. However, such designs result in limited payload capacity, which is undesirable for a cargo trans-

port vehicle like the SST.

To address these challenges and optimise the design, the baseline SST adopts a double hull design for the cylindrical mid-body, as shown in Figure 3.7. This approach eliminates the need for collapse pressure design for the mid-body, as it is flooded and experiences no hydrostatic pressure differential loading. The mid-body external hull becomes non-pressure loading, while the smaller internal pressure hulls, such as cargo tanks and buoyancy tubes, are designed to handle both burst and collapse pressures. This approach can achieve significant weight savings, as the mid-body constitutes a major part of the external hull's structural weight. Using high-strength VL D47 steel material, with a yield strength of 460 MPa and a tensile strength of 550 MPa, enhances the hull's structural capacity and buckling resistance [78]. This material is widely used in large container ship hull structures and provides a cost-efficient yet high-quality construction [79].

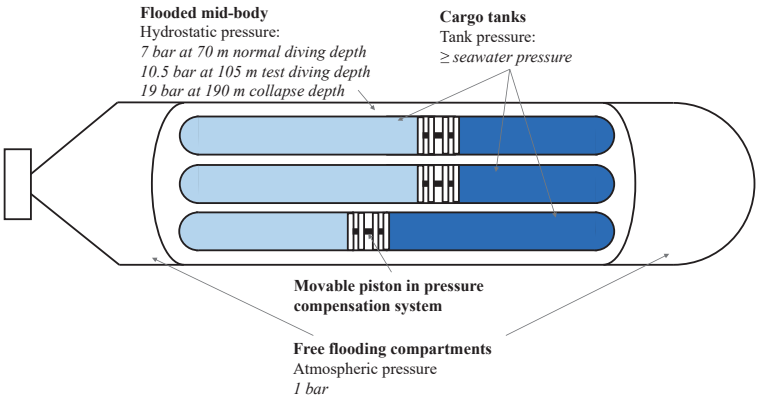

Figure 3.7: SST double hull design with the pressures in all tanks and compartments.

The hemispherical bow and conical aft are free flooding compartments, and they are checked for different conditions such as nominal diving pressure, test diving pressure, and collapse diving depth. These compartments also house the machinery and auxiliary equipment. Stiffeners with specific dimensions are applied to all compart-

ments to increase their structural and buckling capacities. The final external hull properties are summarised in Table 3.8, and detailed design calculations are presented in Appendix C.

Table 3.8: Baseline SST external hull structural properties.

Parameter	Free flooding bow compartment	Flooded mid-body	Free flooding aft compartment
Length [m]	23.75	100.0	40.25
Thickness [m]	0.041	0.025	0.041
Frame spacing [m]	1.0	1.5	1.0
Steel weight [ton]	521	1374	771
Material type	VL D47	VL D47	VL D47
Yield strength [MPa]	460	460	460
Tensile strength [MPa]	550	550	550
Design collapse pressure [bar]	20	7	20

Bulkhead Properties

The SST has four bulkheads that separate the flooded mid-body from the free flooding compartments and support internal cargo tanks and buoyancy tubes. Two watertight bulkheads at the forward and aft vessel divide the SST into three compartments, as shown in Figure 3.7. These bulkheads are subjected to internal hydrostatic pressure and are designed against burst pressure, as they act as pressure vessel heads. The geometry and steel plates used for these bulkheads are presented in Figure 3.8. The thickness of the steel plates for the watertight bulkheads is 53 mm, and they are checked against nominal diving pressure, test diving pressure, and collapse pressure, as detailed in Appendix C. On the other hand, the two non-watertight bulkheads, located in the flooded mid-body, are not subjected to hydrostatic pressures. Their primary function is to support the internal cargo tanks and buoyancy tubes. For these bulkheads, 25 mm thick steel plates with penetrations to accommodate the cargo tanks and buoyancy tubes are used.

Similar to the watertight bulkheads, the non-watertight bulkheads are made from VL D47 steel. The locations and weights of all bulkheads are provided in Table 3.3.

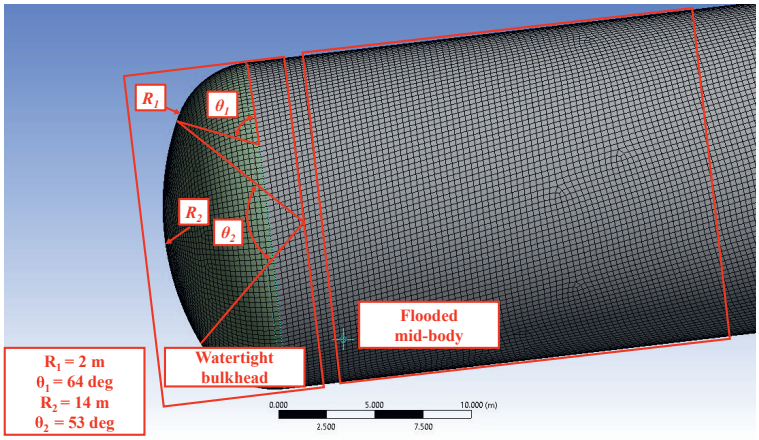

Figure 3.8: SST forward (aft) ellipsoidal watertight bulkhead geometry definition.

3.6.2 Internal Tank Structural Design

The design of all internal tanks in the SST follows the guidelines of ASME BVPC Sec.VIII-2, Chapter 4.3 for shells under internal pressure and Chapter 4.4 for shells under external pressure, considering allowable compressive stresses [80]. It is required that the pressure vessel material listed in ASME BPVC Sec. II is used, so SA-738 Grade B is chosen for the pressure vessel material [81]. SA-738 Grade B is a high-strength carbon steel commonly used in welded pressure vessels operating at moderate or lower temperatures and is readily available from manufacturers like JFE Steel [79]. Detailed design calculations are provided in Appendix D.

There are five types of internal pressure tanks in the SST, as shown in the general arrangement drawing in Figure 3.2. These include main cargo tanks, auxiliary cargo tanks, buoyancy tubes, compensa-

tion tanks, and trim tanks. The properties of these internal tanks are presented in Table 3.9 and discussed as follows:

Cargo Tanks

Tank properties: The SST contains 13 cylindrical cargo tanks (seven main and six auxiliary tanks) with hemispherical ends, symmetrically distributed in the flooded mid-body. The main cargo tanks have a diameter of 5 m, while the auxiliary cargo tanks have a diameter of 2.5 m. This variation in diameter allows for a more efficient arrangement of the tanks, maximising space utilisation and payload capacity. These cargo tanks are used for CO_2 storage and are designed with a burst pressure of 55 bar, the worst-case scenario when the SST is floating on the sea surface. The cylindrical shells of the main cargo and auxiliary cargo tanks have 57 mm and 29 mm thicknesses, respectively.

Table 3.9: Baseline SST internal hull structural properties.

Parameter	Main cargo tank	Auxiliary cargo tank	Compensation tank	Trim tank	Buoyancy tube
Number of tanks	7	6	2	2	8
Length [m]	100	97.5	15	5	100
Diameter [m]	5	2.5	8	7	1.25
Cylinder wall thickness [m]	0.057	0.029	0.015	0.015	0.015
Hemisphere head wall thickness	0.029	0.015	-	-	-
Total volume [m^3]	13,515	2,847	1,600	400	1,030
Steel weight [ton]	4,769	1026	200	70	368
Material type	SA-738 Grade B	SA-738 Grade B	SA-738 Grade B	SA-738 Grade B	SA-738 Grade B
Material allowable stress [MPa]	244	244	244	244	244
Yield strength [MPa]	414	414	414	414	414
Tensile strength [MPa]	586	586	586	586	586
Allowable burst pressure [bar]	55	55	8	10	29
Allowable collapse pressure [bar]	2.6	2.6	0.7	0.6	7
Design pressure type	Burst	Burst	Burst	Burst	Collapse
Burst pressure UF [-]	2.4	2.4	2.4	2.4	2.4
Collapse pressure UF [-]	2.4	2.4	2.4	2.4	2.4

Table 3.10: SST cargo tank pressure during operation. Emergency ascent (descent) are the recoverable emergency cases when the SST has to ascent (descent). PCS initiate depth is where the hydrostatic pressure exceeds the liquid CO_2 pressure, and PCS start functioning. An accidental case is when the SST descents exceed its collapse depth, and sinking might happen.

Depth [m]	Cargo	Season	Temperature [°C]	Tank pressure [bar]	Hydrostatic pressure [bar]	Pressure difference [bar]	PCS used	Note
0	CO_2	Summer	20	55.0	0.0	55.0	No	Operating (Surfaced)
		Winter	0	34.9	0.0	34.9	No	
	Water	-	-	0.0	0.0	0.0	Yes	
40	CO_2	Summer	15	50.9	4.0	46.9	No	Uncontrolled ascent
	Water	-	-	4.0	4.0	0.0	Yes	
70	CO_2	Summer	10	45.0	7.0	38.0	No	Operating (Submerged)
		Winter	1	35.8	7.0	28.8	No	
	Water	-	-	7.0	7.0	0.0	Yes	
175	CO_2	Winter	1	35.8	17.5	18.3	No	Uncontrolled descent (Collapse depth)
>358	CO_2	Winter	1	>35.8	>35.8	0.0	Yes	Uncontrolled descent (Accidental case)

Burst pressure design: To avoid collapse pressure design for the cargo tanks, a pressure compensation system (PCS) is utilised Section 3.8. As shown in Figure 3.7, the cargo tanks experience both external hydrostatic and internal tank pressure. Table 3.10 quantifies these pressures during normal operating, emergency, and accidental scenarios. The PCS ensures that the cargo tank pressure always remains greater than the hydrostatic pressure, preventing negative pressure differences. More details about the PCS system are presented in Section 3.8.

Buoyancy Tank Design

Eight empty buoyancy tanks, each with a diameter of 1.25 m, are positioned at the upper part of the SST to achieve neutral buoyancy. These buoyancy tanks, with a length of 100 m, are directly connected to the forward and aft bulkheads (Figure 3.2 Subview B, C, and D). As they are free flooding and not exposed to water, allowing for the arrangement of moisture-sensitive equipment inside. The buoyancy tubes are supported along their length, with an unsupported length of 4 m, corresponding to twice the flooded mid-body frame spacing. These tanks are designed to handle 7 bar hydrostatic pressure, corresponding to the SST's 70 m nominal diving depth. The resulting thickness of the buoyancy tubes is 15 mm.

3.7 Hydrodynamics and Propulsion

3.7.1 Resistance and Propulsive Power

The SST is designed to operate at slow speeds to ensure maximum energy efficiency and minimise resistance. At the operating speed of 6 knots, the resistance is calculated to be 82 kN, requiring a propulsive power of 253 kW. These values are graphically depicted against different operating speeds in Figure 3.9. The resistance and propulsive

power calculations are based on the ITTC-57 correlation line for skin friction [82] and empirical drag pressure data [51]. It should be noted that resistance and propulsive power increase exponentially with operating speed, making higher speeds economically less favourable for the SST. Further details of these calculations can be found in Appendix B.

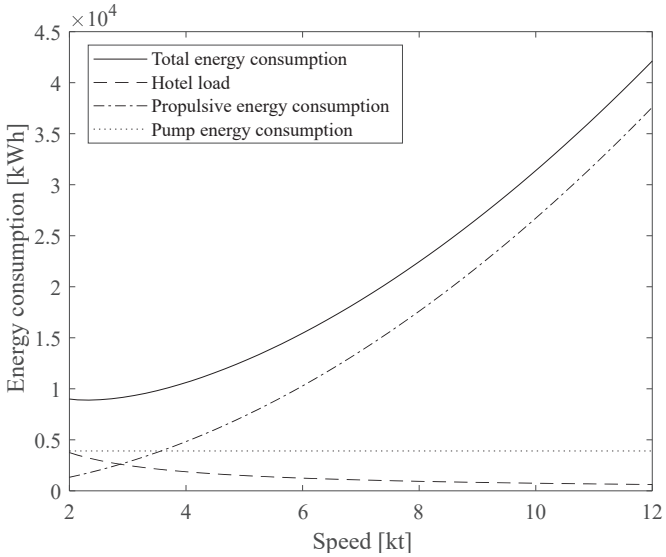

Figure 3.9: Baseline SST energy consumption at different speeds with a range of 400 km.

3.7.2 Propeller Design

The SST has a three-bladed Wageningen B-series propeller [83]. This propeller boasts a large diameter of 7 metres, a small blade area ratio of 0.3, and a slow rotational speed of 38 rpm, contributing to its high quasi-propulsive coefficient (QPC) of 0.97. Submarine propellers with large diameters, slow rotations, and single-screw configurations generally exhibit high efficiencies [19], with QPC values ranging from 0.8 to 1.0 [84]. The propeller's thrust and torque coefficients are 0.17 and 0.010, respectively. The design parameters are listed in Table 3.11.

The detailed calculations are presented in Appendix E.

Table 3.11: Propeller characteristics.

Parameter	Symbol	Value	Unit
Prop. diameter	D_p	7	[m]
Number of blades	N_B	3	[-]
Prop/hull ratio		0.4118	[-]
Propeller pitch/diameter		0.8	[-]
Tailcone angle	α_C	37.56	[◦]
Propeller speed	n	38	[RPM]
Advance velocity	V_A	2.66	[m/s]
Wake fraction	w_T	0.4722	[-]
Thrust deduction	t_D	0.1518	[-]
Advance number	J	0.37	[-]
Thrust coefficient	K_T	0.17	[-]
Torque coefficient	K_Q	0.010	[-]
Open water efficiency	η_O	0.60	[-]
Hull efficiency	η_H	1.61	[-]
Relative rotative efficiency	η_R	1.05	[-]
Quasi-propulsive coefficient	QPC	0.97	[-]

3.7.3 Propulsion Efficiency

The propulsive efficiency of the propeller is calculated to be 88% following Eq. (3.1).

$$\eta_p = QPC \cdot \eta_M \cdot \eta_G \tag{3.1}$$

where η_M and η_G represent the motor and gearbox efficiencies, respectively. In this case, η_M is set to 94 % and η_G to 96 %. These values are typically used for most electrical drives and gearboxes, such as the ABB IE2 motor and corresponding gearbox, employed as ship azimuth thrusters [85, 86]. With these efficiency values, the calculations indicate that the SST's propulsion system provides a propulsive power of 289 kW at a speed of 6 knots.

3.7.4 Hotel Load

The SST's hotel load refers to the power consumption of all systems on board, excluding propulsion and pumps. This includes control units, sensors, and the navigation system, among others. To estimate the hotel load, we use the typical hotel-load-to-propulsion-power ratio observed in modern ships. Specifically, we consider the Wartsila LR2 product tanker and the MUNIN reference container ship, which have hotel-load-to-propulsion-power ratios of approximately 20% [87–89].

Additionally, the reduction in power consumption due to the SST being an autonomous vessel is considered, meaning it does not require crew support systems. This results in a 40% reduction in power consumption compared to conventional crewed vessels [89].

With a propulsive power of 289 kW at the operating speed of 6 knots (Ref. Section 3.7.3), the estimated hotel load for the SST is 35 kW.

$$(propulsive\ power) \times \frac{(hotel\ load)}{(propulsive\ power)} \times (auto.\ reduction) = 289\ kw \times 0.2 \times 0.6 = 35\ kw \quad (3.2)$$

3.7.5 Pump Energy Consumption

The SST's pump energy consumption is significant during the loading and offloading. The calculation of pump energy consumption is as follows:

The SST allows for two load cycles in each trip - one for loading at the port and the other for offloading at the well. Each cycle takes four hours to complete. A conservative value of 75% is used to estimate the pump efficiency based on the efficiency range of large centrifugal pumps and centrifugal compressors, as reported in Elsey (2020) [90] and Chapter 8 of Hall (2017) [91], respectively. For cargo pumps,

they can provide a pressure of 3 bar at a flow rate of 4000 m^3/h. The compensation tank ballast pumps, on the other hand, provide 3 bar pressure at a flow rate of 400 m^3/h to compensate for weight changes during loading and offloading. With this information, the estimated total loading & offloading energy consumption for the SST is calculated by Eq. 3.3 to be 3,911 kWh.

$$\begin{aligned}
&(time) \times (load\ cycle) \times \\
&\frac{(flow\ pressure)_{cargo} + (flow\ pressure)_{ballast}}{3.6 \times 10^6 \times (pump\ efficiency)} \\
&= 4\ h \times 2 \times \frac{\left(4000\ m^3/h \times 3 \times 10^5\ Pa\right) + \left(400\ m^3/h \times 3 \times 10^5\ Pa\right)}{3.6 \times 10^6 \times 75\%} \\
&= 3.91 \times 10^3\ kWh
\end{aligned} \tag{3.3}$$

3.7.6 Total Energy Consumption

At the operating speed of 6 knots, the total energy consumption is the sum of the hotel load (35 kW) and propulsion power (289 kW), resulting in 324 kW. Additionally, the pump energy consumption is fixed at 3,911 kWh. For a range of 400 km (as shown in the power consumption plot in Figure 3.9), the total energy consumption is calculated to be 15,527 kWh. This is significantly lower than conventional ships, such as the WSD50 30K LNG carrier, which would consume 160,827 kWh for the same voyage [92]. The SST's low energy consumption enables it to be fully electrically propelled and emission-free.

3.7.7 Battery

The SST uses a Li-ion battery due to its high energy density, high specific energy, steady power output, and long service time. Li-ion batteries have been successfully utilised in submarines, and their technological advancements are expected to increase energy density significantly

in the next decade [93, 94]. Based on the Sion Power 2022 forecast, which predicts a specific energy of 500 Wh/kg (2.5 times the current typical specific energy of 250 Wh/kg) with a 20% margin, the total battery capacity is estimated to be 20,000 kWh [95]. Consequently, the SST's battery weight is estimated to be 40 tonnes, mounted at the aft of the vessel. Charging can occur at the port and subsea well during loading and offloading. The charging time using a 2,000-kW class charger would be around 10 hours, and the battery has a life of 1,000 discharge cycles or approximately 8.3 years if two 400 km trips are performed weekly. The battery properties of the SST are presented in Table 3.12.

Table 3.12: Battery properties.

Parameter	Value
Specific energy [Wh/kg]	500
Energy density [Wh/l]	1,000
Capacity [kWh]	20,000
Weight [ton]	40
Volume [m^3]	20
Life cycle	1,000 discharge cycles 8.3 years

3.8 Pressure Compensation System

The Pressure Compensation System (PCS) is an essential feature of the SST and ensures the integrity of the cargo tanks by equalising internal and external pressures under various operating conditions (as demonstrated in Table 3.10). The PCS consists of a movable piston with seals inside the cargo tank, which separates the CO_2 and seawater. These piston seals can be made from materials like polyurethane, similar to those used for batching pigs in pipelines. Additionally, intelligent pigging sensors can be incorporated into the pistons to monitor critical data, such as tank pressure, cargo temperature, and corrosion

status. As illustrated in Figure 3.10, the PCS functions in the following manners to maintain pressure balance within the cargo tanks:

3.8.1 Normal Operating Case

In the normal operating case (70 m, summer, liquid CO_2 in Table 3.10 and Figure 3.10, a), the SST is typically submerged at a depth of 70 metres, transporting liquid CO_2 at a pressure of 35 to 55 bar, depending on the seawater temperature. The piston seals ensure that the pressure of seawater on one side of the piston is equal to the pressure of the CO_2 on the other. This pressure compensation equalises the internal and external pressures within the cargo tanks, ensuring stability during normal operations.

3.8.2 Uncontrolled Descent Case

In an accidental uncontrolled descent scenario, where the SST descends to a depth exceeding 358 metres, the external hydrostatic pressure can increase significantly (e.g., 50 bar at a depth of 500 metres). This corresponds to Figure 3.10 (b). The PCS addresses this situation by allowing seawater to flow into one end of the cargo tank, pushing against the piston and ultimately equalising the internal pressure with the increased external pressure. This feature prevents excessive pressure differentials and ensures the cargo tanks' integrity in non-recoverable accidents.

3.8.3 Uncontrolled Ascent Case

As shown in Figure 3.10 (c), during an uncontrolled ascent case, where the SST rises to a shallower depth (e.g., 40 metres), the external hydrostatic pressure decreases (e.g., 4 bar). In response, the CO_2 pressure increases inside the cargo tanks due to the temperature rise. The PCS maintains pressure balance by allowing the CO_2 pressure to push

against the piston towards the seawater, increasing the seawater pressure until it is equal to the internal CO_2 pressure. This process prevents excessive pressure differentials and ensures the structural integrity of the cargo tanks.

3.8.4 Seawater Filled Cases

In situations where the cargo tanks are entirely filled with seawater (Figure 3.10, d), such as after the SST is offloaded at a subsea well, the PCS allows the valves to open, allowing seawater to flow in and increase the internal pressure until it is equalised with the external hydrostatic pressure. This feature ensures that the cargo tanks do not need to be designed to withstand the full external hydrostatic pressure, reducing structural costs.

3.9 Offloading

The offloading process for the SST involves transferring CO_2 through a flexible flowline connected to the subsea well while the vessel hovers at its operating depth in the vicinity. The procedure is described in the following steps and depicted in Figure 3.11:

- **Step 1:** The SST approaches the subsea well and hovers nearby at its designated operating depth.
- **Step 2:** An ROV is deployed to carry the flexible flowline from the subsea well and connect it to the SST.
- **Step 3:** Liquid CO_2 is pumped out from one end of each cargo tank through the mated connection to the subsea well. Seawater is simultaneously pumped into the other end of each cargo tank to maintain tank pressure and fill the void left by the CO2. During this process, the compensation and trim tanks are also utilised to maintain the SST's trim and neutral buoyancy.

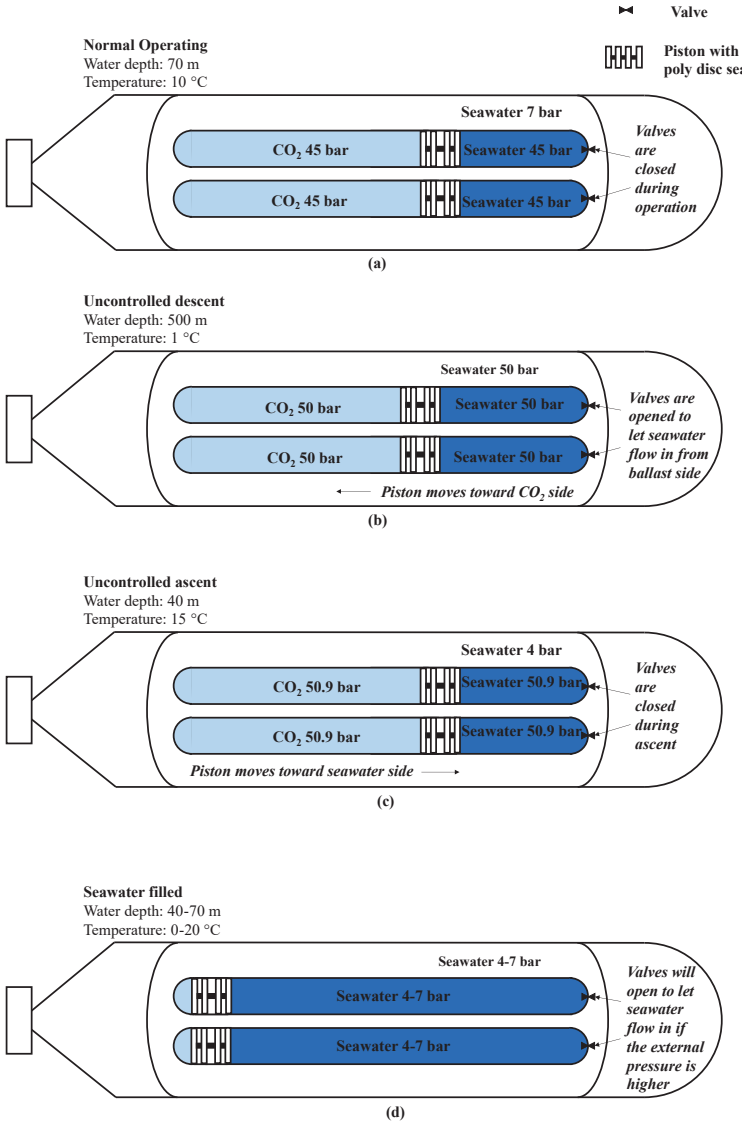

Figure 3.10: Illustration of the functionality of the pressure compensation system.

- **Step 4:** Once the offloading is completed, the ROV disconnects the flowline from the SST.

This offloading method offers several advantages. First, it allows the SST to offload at subsea wells at greater depths while maintaining

a constant operational depth (up to a maximum of 70 metres). As a result, the SST only needs to be designed to withstand pressures at a depth of 70 metres rather than the subsea wellhead's full water depth. Additionally, this method minimises the risk of collision between the SST and subsea facilities, as the vessel does not need to approach the wellhead closely during offloading. Using an ROV ensures precise and safe mating of the flowline to the SST, even in environmental loads. However, the SST requires a dynamic positioning system to maintain its position during offloading. A preliminary CFD analysis revealed that the drag force of a sideways current is significantly higher than when the SST is facing the current [96]. Therefore, it is essential for the SST to constantly face the current during offloading. The dynamic positioning system must be capable of limiting the maximum displacement to within 5 metres in a 1 m/s designed current. Based on previous studies on vessel station-keeping capabilities, the SST is expected to deliver similar performance, ensuring safe and efficient offloading operations.

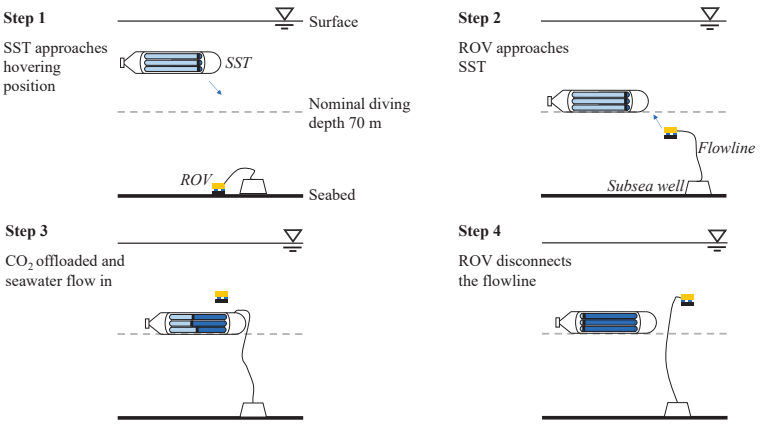

Figure 3.11: SST offloading sequence.

3.10 Concluding remarks

In this chapter, we introduce a baseline design for an SST, which has been developed to support research efforts in the field of large underwater cargo vehicles. The primary objective of this SST is the transportation of liquid CO_2 for direct injection into subsea wells. This SST is proposed as a potential alternative to conventional marine transportation methods like shuttle tankers, pipelines, and umbilicals. It offers the possibility of exploring remote marginal fields as offshore carbon storage sites. We provide a detailed overview of the key specifications and features of this SST, encompassing CO_2 properties, hydrostatic properties, structural properties, hydrodynamic properties, the pressure compensation system, and the offloading method.

One of the standout features of this SST is its double hull design, complemented by a pressure compensation system. This unique configuration allows the SST to circumvent the need for a collapse pressure design in the external hull's flooded mid-body section. Consequently, this design approach serves to reduce the SST's structural weight significantly while enhancing its payload capacity, accounting for approximately 46% of its total displacement. Notably, this substantial payload capacity, coupled with a deliberate emphasis on slow service speed, enables the SST to optimize its transportation efficiency while minimizing energy consumption.

Chapter 4

Critical Challenges of CO_2 SST Transportation

This Chapter continues the discussions in Section 3.3 on SST design challenges related to CO_2 transportation, including CO_2 thermodynamic properties, purity, cargo tank sizing, material selection, energy consumption, and hydrate formation. This Chapter aims to provide valuable insights into managing and reducing uncertainties associated with the CO_2 transportation aspect of the SST concept.

4.1 CO_2 Properties

4.1.1 Thermodynamic Properties

The thermodynamic properties of CO_2 have a critical impact on the design of the SST's cargo tanks, as impurities can lead to erosion and increase the risk of hydrate formation. These properties can be represented on a phase diagram, as shown in Figure 4.1. Depending on the pressure and temperature, CO_2 can exist in four phases: solid, liquid, vapour, and supercritical.

The triple point (5.1 bar, 56 °C) is where CO_2 exists simultaneously in vapour, liquid, and solid phases. Beyond the critical point (74 bar, 32 °C), CO_2 turns into a supercritical phase.

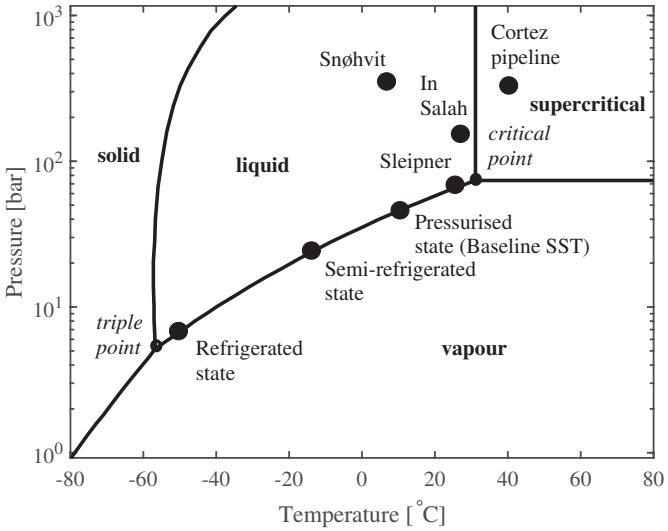

Figure 4.1: Carbon dioxide phase diagram with transportation and injection states.

Different transportation methods involve different states of CO_2. Pipelines transport CO_2 in a high-pressure, high-temperature supercritical phase. On the other hand, ships carry CO_2 as a saturated liquid, where CO_2 is constantly boiling, and the pressure and temperature are naturally maintained at a setpoint. CO_2 can be carried under one of the three states along the saturation line: refrigerated state (7 bar, -55 °C), semi-refrigerated state (15 bar, -30 °C), or pressurised state (45 bar, 10 °C) [97, 98].

For larger vessels like Very Large Gas Carriers (VLGC), refrigeration is used to transport CO_2 as a refrigerated liquid at very low temperatures, as constructing large pressure vessels with high pressure capacities would be uneconomical [99]. Smaller ships with capacities of around 10,000 m^3 prefer semi-refrigeration, e.g., the Northern Light CO_2 carrier [76]. Pressurised liquid CO_2 transportation is a more attractive option for offshore CCS or enhanced oil recovery (EOR) projects with moderate capacities. The SST transports CO_2 as

a pressurised liquid, eliminating the need for refrigeration. The cargo tanks are designed to handle higher pressures of 40 to 60 bar.

Figure 4.1 also presents the CO_2 wellhead injection states. For example, at Snøhvit, In Salah, and Sleipner fields, CO_2 is injected at an intermediate temperature and high pressure (10 - 30 °C, > 80 bar) [76, 100].

Figure 4.2 illustrates the main processes in CO_2 transportation, indicating that refrigerated, semi-refrigerated, and pressurised states present different challenges for SST. Transporting CO_2 as a pressurised liquid (Baseline SST) is more cost- and energy-efficient. No liquefaction and heating systems are required at the port, and no costly re-liquefaction system is needed during offloading at the wellhead. A single-stage booster pump can directly inject the liquid CO_2 into the reservoir [23].

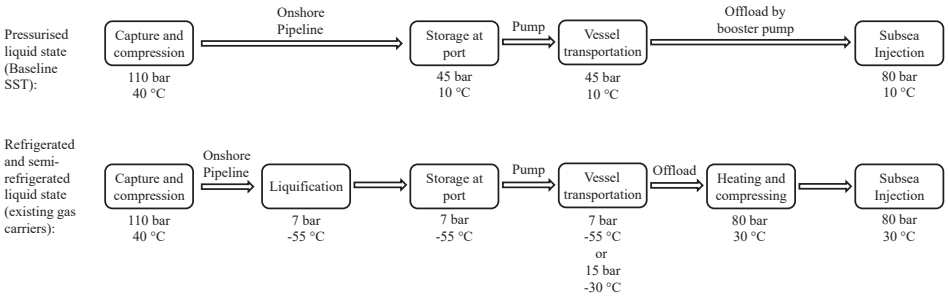

Figure 4.2: CCS/EOR life cycles when using baseline SST (also shown in Figure 1.2) and liquefied gas carrier transportation.

4.1.2 Impurities in CO_2

Fossil fuel combustion is the primary source of human-activity-related CO_2, contributing to 92.4% of the total CO_2 emissions in the US in 2008 [101]. Electricity generation and transportation are the major contributors, accounting for 34.5% and 32.6% of the total emissions, respectively. Besides CO_2, other common components in emitted gases include N_2, H_2O, and O_2 [102]. Additionally, carbon sources

like coal-fired power plants contain contaminants such as sulphur oxides (SO_x), hydrogen sulphide (H_2S), and nitrogen oxides (NO_x) [103].

The purity of captured CO_2 can vary significantly based on the carbon source and the capture and separation technology used. Figure 4.3 illustrates the purities of captured CO_2 from three different combustion methods. Table 4.1 provides CO_2 impurity limits in several CCS projects. The design limits for the SST adapt the levels from the Northern Light project. Common purity levels are above 95%, with some projects achieving CO_2 concentrations higher than 99.9%. However, extremely high purity levels may not be necessary for most transportation, storage, or EOR purposes. Optimising the purity level can help reduce energy consumption and purification costs [104].

While high purity levels may not be required for transportation purposes, it's essential to consider the impact of impurities on the SST's design. Higher impurity levels in liquid CO_2 can lead to increased pressure requirements on the cargo tanks to avoid the risk of hydrate formation and corrosion. Impurities can also affect the volume and compressibility of CO_2, potentially reducing the carrying capacities of the cargo tanks [19]. Therefore, finding the optimal purity level for SST is crucial to balance efficiency and safety.

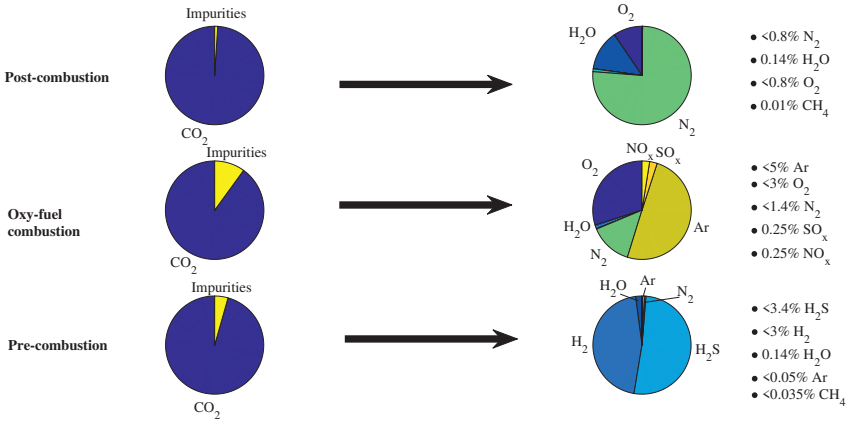

Figure 4.3: Expected impurity levels from different carbon capture methods [105].

Table 4.1: CO_2 impurity levels from different projects. The SST adapts the same value as the Northern Light project.

Component	North Lights [76] (Various sources)	Dynamis [75] (Hydrogen production)	Schwarze [104] (Power plant)	ICF [101] (Cement plant)
CO_2	>99.9%	>95.5%	>99.9%	99.8%
H_2O	30 ppm	500 ppm	<5 ppmv	640 ppmv
SO_x	10 ppm	100 ppm	1.3 ppmv	<0.1 ppmv
NO_x	10 ppm	100 ppm	3-10 ppmv	0.86 ppmv
H_2S	9 ppm	200 ppm	-	-
CO	100 ppm	200 ppm	<2 ppmv	1.2 ppmv
O_2	10 ppm	Aquifer <4 vol% EOR 100-1000 ppm	<0.001 vol%	35 ppmv
CH_4	-	Aquifer <4 vol% EOR <2 vol%	-	0.026 ppmv
Amines, RNH_3	10 ppm	Non-considerable gases <4 vol%	-	-
Ammonia, NH3	10 ppm		-	-
H_2	50 ppm		-	-
HCHO	20 ppm		-	-
CH_3CHO	20 ppm		-	-
N_2 & Ar	-		<0.01% vol%	904 ppmv

Free Water

The presence of free water is the most undesirable impurity in liquid CO_2 due to its potential to cause hydrate formation and corrosion. Water easily reacts with many acid gas components, posing risks to the transportation and storage processes. Figure 4.4, based on the study by Visser et al. [75], illustrates the solubility of water in CO_2 at different pressures and temperatures.

Water solubility in CO_2 is low at low pressures and temperatures. This indicates that transporting CO_2 in refrigerated or semi-refrigerated conditions would require higher purity levels, as less water can dissolve in CO_2, producing more free water. In contrast, the SST transports CO_2 in pressurised conditions where CO_2 solubilities exceed 2,000 ppm. This value of 2,000 ppm is higher than the requirements defined in many CCS projects, including those presented in Table 4.1. Therefore, if the SST is utilised in these projects, no free water would appear in the CO_2 transported, reducing the risk of hydrate formation and corrosion. This advantage further supports the suitability of the SST as an effective alternative for offshore CO_2 transportation.

SO_x and NO_x

In Dynamis project [75], limits on SO_x and NO_x are set because they are toxic to humans. For the SST, being an unmanned vessel, it may be postulated that no limits on these gases are required. Ahmad and Gersen [106] performed a study at pressures of 90-120 bar and temperature of 10 - 45 °C. Preliminary results demonstrated that these gases can affect water solubility and increase the risk of hydrate formation. However, further detailed investigations are necessary to fully understand the potential impact of SO_2 and NO_2 on water solubility and the risk of hydrate formation at the pressure and temperature ranges of SST transportation.

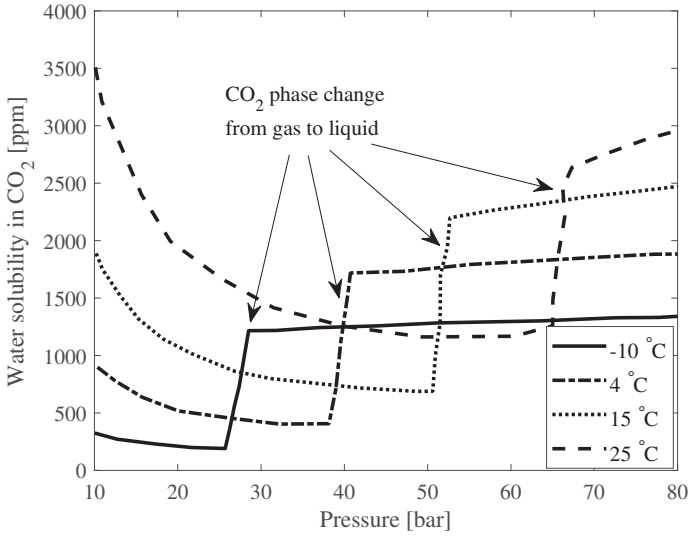

Figure 4.4: Water solubility in liquid CO_2 at different pressures and temperatures.

Other impurities

The SST limits other impurities like CH_4, N_2, and amines to mitigate hydrate formation. These impurities can reduce water solubility and increase the risk of hydrate formation [107]. Managing these impurities is crucial to ensure the safe transportation of CO_2 without compromising the integrity of the cargo tanks and the overall operation of the SST.

4.2 Challenges on Cargo Tank Design

4.2.1 Sizing

Most liquid CO_2 are transported by ships in the semi-refrigerated state [76, 97, 99, 108–110]. This allows the use of large cargo tanks of up to volumes of 4000 m^3 because of the low cargo pressure (about 6 to 22 bar at -50 to -15 °C). For instinct, the Northern Lights project [13] uses

a 7500 m^3 gas carrier with two 3750 m^3 type-C storage tanks. This is similar to liquefied petroleum gas (LPG) carriers that transport semi-refrigerated LPG. For example, the typical size range for a type-C LPG tank is between 4000 m^3 to 22,000 m^3 [111]. No VLGC are yet used for refrigerated CO_2 transportation for profit reasons. But they have been widely utilised for LNG. LNG carriers carry refrigerated LNG at 1 to 2 bars at -165 °C and utilise cargo tanks of up to 20,000 m^3. The SST transports liquid CO_2 at environmental temperature, leading to higher pressures of 40 to 60 bars and therefore requires a more demanding burst pressure design. For thin-walled cylinder-shaped pressure vessels, the burst failure is dominated by the yielding of the material. Following Barlow's formula, the internal pressure $p_{internal}$ that a thin-walled cylinder-shaped pressure vessel can withstand is calculated as:

$$p_{internal} = \frac{2 \cdot SF \cdot \sigma_y \cdot t_{tank}}{D_{out}} \tag{4.1}$$

where σ_y is the yield stress, t_{tank} is the wall thickness, D_{out} is the external diameter of the cylinder, and SF is the safety factor. Xing et al. [19] used this method to estimate the internal pressure capacity of the SST cargo tanks when stainless steel 304 (yield strength σ_y = 207 MPa) is applied. $1/SF$=0.72 is used. The results, i.e., internal pressure capacities, are presented in Table 4.2 for different vessel diameters and wall thicknesses. As observed in Table 4.2, the W_{tank}/V_{tank} ratios are the same for all cases. This is because W_{tank}/L_{tank} and V_{tank}/L_{tank} are directly proportional to (diameter)^2. This means designing larger cargo tanks does not save structural weight or increase cargo capacity. However, the bending and welding of thicker plates can be more complex. For this reason, the SST uses several smaller tanks instead of a single large tank. Seven 5 m diameter main cargo tanks and six 2.5 m diameter auxiliary cargo tanks are used [23]. The volumes are 1931 m^3 and 483 m^3, respectively, much smaller than the semi-refrigerated cargo tanks discussed above. However, the cargo weight still constitutes a large portion (53%) of the SST's total weight.

Table 4.2: Internal pressure capacities for the SST cargo tanks.

Diameter [m]	Wall thickness [mm]	Internal pressure capacity [bar]	Weight/length, W_{tank}/L_{tank} [kg/m]	Cargo volume/length, V_{tank}/L_{tank} [m³/m]	Ratio W_{tank}/V_{tank}
0.5	7.5	45	92	0.20	471.02
1	15.1	45	370	0.79	471.02
1.5	22.6	45	832	1.77	471.02
2.5	37.7	45	2,312	4.91	471.02
5	75.5	45	9,248	49.64	471.02
10	151.0	45	36,993	78.54	471.02
15	226.4	45	83,235	176.71	471.02

4.2.2 Material Selection

The SST cargo tanks operate at environmental temperatures. This allows the use of highly weldable carbon steels, such as SA-738 Grade B, commonly applied to welded pressure vessels subjected to moderate or low temperatures. This material choice suits the SST's operating conditions and ensures good weldability. However, for LNG and LPG carriers, which experience much lower service temperatures, DNVGL-RU-SHIP-Pt2Ch2 recommends using fine-grained carbon-manganese structural steels and nickel alloy steels [78]. They have higher manganese and nickel content to achieve lower design temperatures [112]. The DNV grade VL 4-4 suits semi-refrigerated CO_2 tanks. It has a manganese content between 0.7-1.6% and a high tensile strength between 490 and 610 MPa [78]. In addition, VL 2.25Ni is a potential choice for fully refrigerated cargo tanks due to its excellent strength and toughness at low temperatures (-65 °C design temperature). However, these materials are more expensive and complex to weld than the carbon steel used on the SST.

4.3 Challenges on SST Operation

4.3.1 Energy Consumption

In typical CO_2 transportation by vessels, energy consumption can be categorised into three main areas: cargo processing, propulsion, and pumping. Cargo processing includes liquefaction and cargo conditioning, which requires significant energy due to the multi-stage cooling and compression required for boil-off gas liquefaction. However, the SST transports CO_2 at environmental conditions. Therefore, it does not require cargo processing, resulting in substantial energy savings.

Table 4.3 compares the energy consumption per tonne of CO_2 by SST and ship for a 1,500 km trip. A fully refrigerated 20,000 m^3 vessel transporting CO_2 over a 1,500 km round trip has a specific energy consumption of 25 kWh/tonne CO_2 [108]. On the other hand, the SST's propulsion energy consumption at 6 knots speed is 289 kW as calculated in Section 3.7, resulting in 40,139 kWh for the 1,500 km trip. The pumping energy consumption for loading and offloading is calculated to be 3,900 kWh per trip. This means that the SST's transportation energy consumption is nearly 90% lower than that of the reference surface ship, making it a highly energy-efficient and environmentally friendly option for CO_2 transportation.

Table 4.3: SST CO_2 transportation energy consumption and comparison with ships.

Transportation method	**SST environmental temperature** [23]	**Ship with refrigeration at -52 °C [108]**
Propulsion	40,139 kWh	-
Pumping	3,900 kWh	-
Other hotel loads	4,861 kWh	-
Total energy consumption	48,900 kWh	-
Specific energy	3.19 kWh/tonne	25 kWh/tonne

4.3.2 Hydrate Formation

Hydrate formation in cargo tanks is a critical concern that must be carefully avoided. Operating the SST within the hydrate formation zone can lead to blockage and sealing issues in critical systems like piping and seals.

Figure 4.5 illustrates the hydrate phase equilibrium points of pure CO_2. It shows that hydrate formation is more likely to occur at very low temperatures ranging from -40 to 0 °C. Therefore, when transporting CO_2 with refrigeration, it is essential to ensure that the CO_2 liquid is properly dried to prevent hydrate formation.

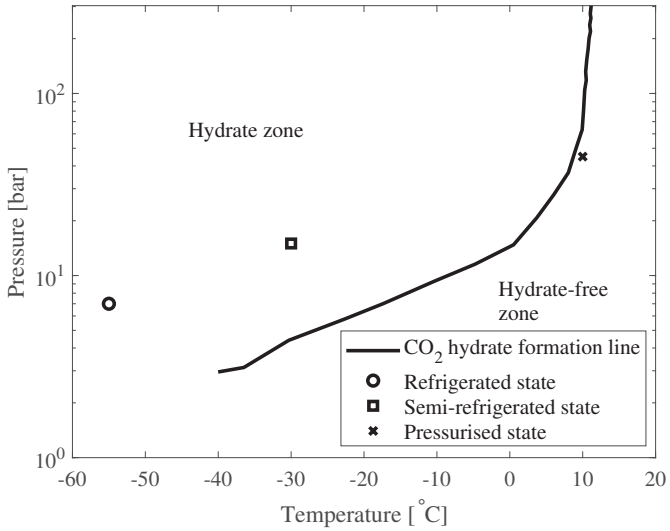

Figure 4.5: Hydrate formation zone of CO_2 and transportation states.

However, the risk of hydrate formation is unlikely when CO_2 is transported at environmental temperatures (>8 °C). This is a significant advantage of transporting CO_2 under a pressurised state at room temperature, as it reduces the need for extensive drying and refrigeration systems. Transporting CO_2 in this manner can also mitigate the risk of free water and corrosion due to the increased water solubility

in CO_2 at higher temperatures.

4.4 Concluding remarks

This chapter evaluates the most important challenges of CO_2 transportation with the SST. In theory, CO_2 may be transported by the SST as a saturated liquid under one of the 3 states: Refrigerated state (6 bar, -50 °C), semi-refrigerated state (22 bar, -10 °C), or pressurised state (45 bar, 10 °C). Thermodynamic properties, purity captured from the source facility, and hydrate formation are discussed. In conclusion, transporting CO_2 under a pressurised state at environmental temperatures offers several advantages. It significantly reduces energy consumption by eliminating the need for liquefaction requirements. Additionally, using carbon steel for cargo tank construction simplifies welding and reduces manufacturing costs. Moreover, the risk of hydrate formation is significantly lower at room temperature, reducing the likelihood of blockages in the piping and pumps. However, knowledge gaps still need to be addressed through further research, such as the actual effects of saturated CO_2 liquid with different purity levels under various pressure and temperature conditions specific to the SST's operation. Addressing these gaps will help ensure the safe and efficient transportation of CO_2 using the SST and gas carriers in general.

Chapter 5

Hovering Control and Analysis

This chapter introduces a comprehensive manoeuvring model and an LQR control system for stabilising the SST in stochastic current conditions. The flowchart of the model is depicted in Figure 5.1.

Initially, an SST manoeuvring planar model is presented in Section 5.1 based on the existing baseline design, wherein the SST utilises its main propeller and two vertical tunnel thrusters to manage external loads. Subsequently, a simplified state-space model is linearised from the planar model. This linear state-space model is utilised to determine the LQR controller gain and Luenberger observer gain. The sensitivity analyses of the linearisation point and observer gain are presented in Section 5.2.2 and 5.3, respectively.

The LQR controller calculates the hovering control input $\boldsymbol{u(t)}$. The incoming current is modelled as a first-order Gauss-Markov process in both current velocity and inflow angle. The SST states are measured using a Luenberger observer. The model developed in this thesis contributes valuable insights into manoeuvring and hovering analyses for future extra-large AUVs currently under development, aiming to reduce carbon footprint and optimise ocean exploration. Additionally, this model can address critical questions and enhance the conceptual design process for such vehicles.

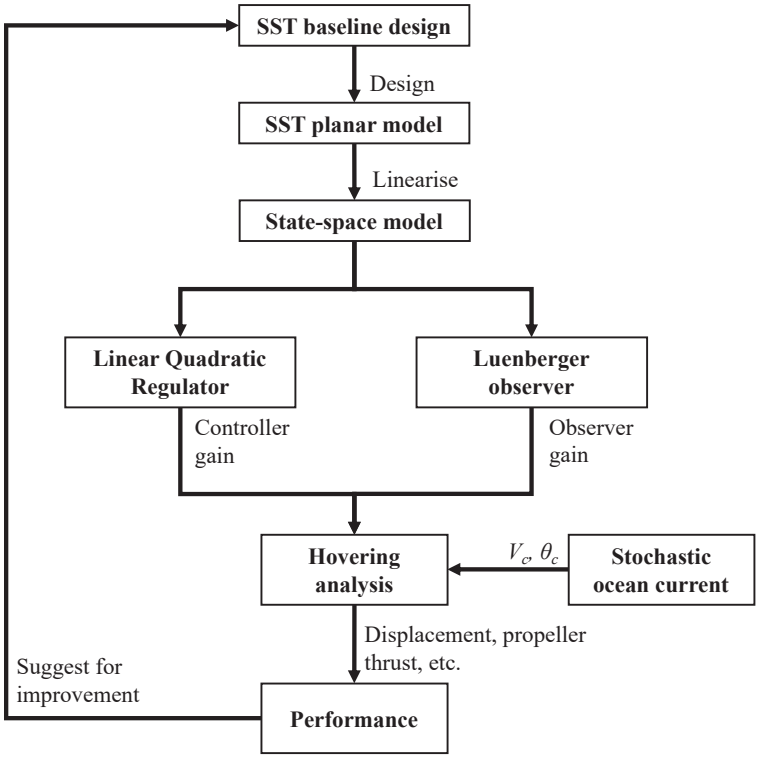

Figure 5.1: Hovering analysis flowchart.

5.1 Model Description

5.1.1 Coordinate System

The vehicle body-fixed coordinate system is positioned at the vehicle's CoG. This body-fixed frame of reference moves relative to an earth-fixed global reference frame, with its axes oriented as North, East, and Down. The CoB is located directly above the CoG at the geometric centre of the SST. The coordinate system is illustrated in Figure 5.2.

In Figure 5.2, N and D are translational motion in the earth-fixed coordinate system; is the pitch rotational motion; u, w, and q are surge velocity, heave velocity, and pitch velocity, respectively; $\dot{u}$, $\dot{w}$, and $\dot{q}$ are the corresponding accelerations.

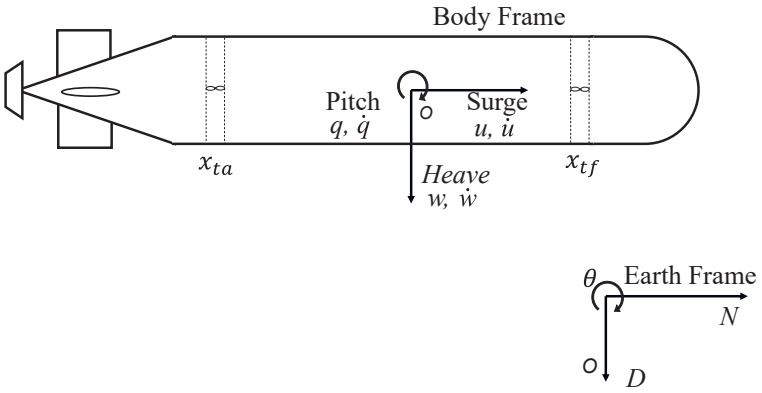

Figure 5.2: SST coordinate system setup used in Chapter 5.

5.1.2 Plant Model

The baseline SST presented in Chapter 3 is used to develop the SST manoeuvring model. The design configurations used in this study are presented in Table 5.1. The manoeuvring system setup is presented in Section 2.2 and the derived hydrodynamic derivatives are presented in Table 5.2.

Table 5.1: SST design parameters used in Chapter 5.

Parameter	Value	Unit
Length	164	m
Beam	17	m
Total mass	3.36×10^7	kg
Pitch moment of inertia I_{yy}	3.63×10^9	kg·m²
CoB $[x_b, y_b, z_b]$	[0, 0, -0.41]	m
Forward tunnel thruster position x_{tf}	60	m
Aft tunnel thruster position x_{ta}	-60	m
Tunnel thruster diameter D_t	2	m
Tunnel thruster thrust coefficient K_{Tt}	0.4	-
Main propeller diameter D_p	7	m
Main propeller thrust coefficient K_{Tp}	0.19	-

Table 5.2: SST hydrodynamic derivatives calculated following Section 2.2.

Parameter	Value	Unit	Parameter	Value	Unit
$X_{\dot{u}}$	-5.14×10^5	kg	$Z_{\|q\|q}$	4.79×10^9	kg·m
$Z_{\dot{w}}$	-3.29×10^7	kg	$M_{\|q\|q}$	-4.34×10^{12}	kg·m^2
$M_{\dot{w}}$	-4.40×10^8	kg·m	X_{wq}	-3.28×10^7	kg
$Z_{\dot{q}}$	-4.40×10^8	kg·m	X_{qq}	-4.40×10^8	kg·m
$M_{\dot{q}}$	-6.39×10^{10}	kg·m^2	Z_{uq}	5.14×10^5	kg
$X_{\|u\|u}$	-1.64×10^4	kg/m	M_{uq}	-4.40×10^8	kg·m
$Z_{\|w\|w}$	-1.42×10^6	kg/m	Z_{uw}	-2.42×10^5	kg/m
$M_{\|w\|w}$	1.67×10^7	kg	M_{uw}	-3.99×10^7	kg

5.1.3 Thruster

As illustrated in Figure 5.2, the SST is equipped with two identical tunnel thrusters: a forward thruster and an aft thruster. The specific locations of these thrusters are detailed in Table 5.1. The thrust exerted by each thruster, denoted as τ_t, is determined by Eq. (5.1). This equation is then applied to compute the thrust of the forward thruster (τ_{tf}) and the aft thruster (τ_{ta}).

$$\tau_t = K_{Tt} \cdot \rho \cdot n_t^2 \cdot d_t^4 \tag{5.1}$$

In the given equation, K_{Tt}=0.4 represents the thrust coefficient, n_t denotes the rotational speed of the thruster and d_t stands for the thruster diameter. The estimated diameter of the SST tunnel thruster is approximately 2 meters, closely resembling current Kongsberg marine tunnel thrusters [113]. Remarkably, a single designated propeller can generate a maximum thrust of 164 kN at a speed of 300 RPM, equivalent to the lateral drags experienced during heaving at a speed of 1 knot. The subsequent simulation results presented in Section 5.4 provide evidence that this design is proficient in delivering ample thrust for the intended current speed during hovering operations.

5.1.4 Main Propeller

A preliminary SST propeller design is documented together with the baseline SST [23]. A 3-bladed Wageningen B-series propeller is employed for the SST in this configuration. The propeller's diameter, denoted as d_p, is set at 7 meters, while its thrust coefficient K_{Tp} is determined to be 0.19. Similar to thrusters, the propeller thrust can be derived as:

$$\tau_p = K_{Tp} \cdot \rho \cdot n_p^2 \cdot d_p^4 \tag{5.2}$$

where n_p is the propeller's rotational speed (rotation per second).

5.1.5 Stochastic Ocean Current

Research studies and guidelines have previously addressed modelling stationary ocean currents [114–116]. However, these models are inadequate for investigating the SST's positioning challenges under time-varying currents. The stochastic ocean current model adopted in this study is based on the formulation introduced by Fossen [47] and Sørensen [117]. This model characterises the current velocity and direction as a first-order Gauss-Markov process. The representation of the current profile is provided as:

$$\dot{V}_c + \mu_1 V_c = \omega_1 \tag{5.3}$$
$$\dot{\theta}_c + \mu_2 \theta_c = \omega_2 \tag{5.4}$$

Here, V_c represents the current speed, and θ_c denotes the inflow angle. The constants μ_1 and μ_2 are associated with the time constant of the Gauss-Markov process, while ω_1 and ω_2 are Gaussian white noise terms.

The non-negative constants μ_1 and μ_2 significantly determine the rise time before a steady state is attained. This thesis selects a value of

1 for both constants to expedite the rise time and establish a steady-state current profile. Three mean current speeds are examined: 0.5 m/s, 1 m/s, and 1.5 m/s. The baseline SST design's designated current speed is set at 1 m/s. This value closely aligns with the highest seasonal current velocities of approximately 0.96 m/s, as observed in the northern North Sea [118]. Additionally, the Norwegian Petroleum Directorate [72] has indicated that the Norwegian Coastal Current, extending from northern Scotland to the eastern North Sea at depths up to 100 m, frequently exceeds speeds of 1 m/s. It is important to note that the current speed is initially defined within the global NED frame and is subsequently transformed into the SST's body-fixed frame. This converted value is then incorporated into the SST's velocity to calculate the hydrodynamic forces.

During the setup of the model in Simulink, the current speed is expressed in the global NED frame. It is then converted into the body-fixed frame and added to SST velocity to calculate the hydrodynamic forces.

5.1.6 Model Implementation

The mathematical concepts outlined above are translated into a Simulink model, visually represented in Figure 5.3. This model is compartmentalised into three distinct blocks, each contributing to the overall simulation:

- **Plant Model:** This block encapsulates the equations governing the SST's motion. It considers the SST's hydrodynamic characteristics, encompassing factors like added mass, damping, and the influence of body lift forces.

- **Actuators:** All actuator-related effects are consolidated within this block. This includes contributions from components such as the propeller, skeg (hydroplane), ballast tanks, and thrusters.

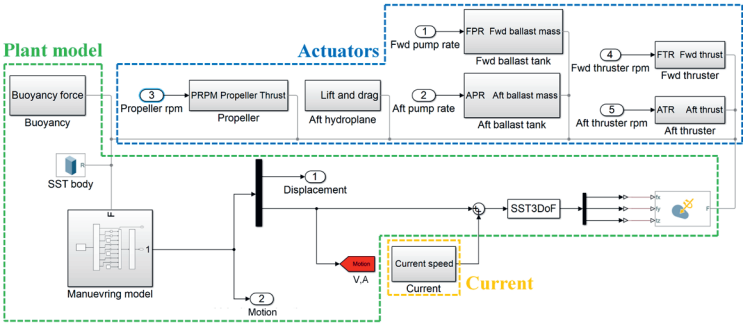

Figure 5.3: Simulink model implementation.

For this chapter, the ballast tank is simplified as a constant mass, ensuring the SST remains neutrally buoyant.

- **Current:** Ocean current is generated within this block. The current velocity is then integrated with the SST's velocity, providing the relative velocity between the SST and the surrounding flow.

5.1.7 Control System

The methodology regarding the controller and observer design is presented in Section 2.3. A block diagram that illustrates the control loop for the SST hovering problem is depicted in Figure 5.4. The configuration of this control diagram resembles that of a full-state feedback control system with an observation mechanism.

As indicated in the diagram, the initial step involves calculating the actuator control input $\boldsymbol{u}$ based on state feedback and a trajectory reference. This calculated input is then fed into the SST manoeuvring system, which interacts with current disturbances to generate the output $\boldsymbol{y}$. To measure the SST states, an observer is employed, which takes both the system control input $\boldsymbol{u}$ and the system output $\boldsymbol{y}$ as inputs and produces the estimated state $\hat{\boldsymbol{x}}$ as output. Subsequently, the estimated states are multiplied by the controller gain to derive the feed-

back, which is eventually employed to compute the final actuator control input $\boldsymbol{u}$.

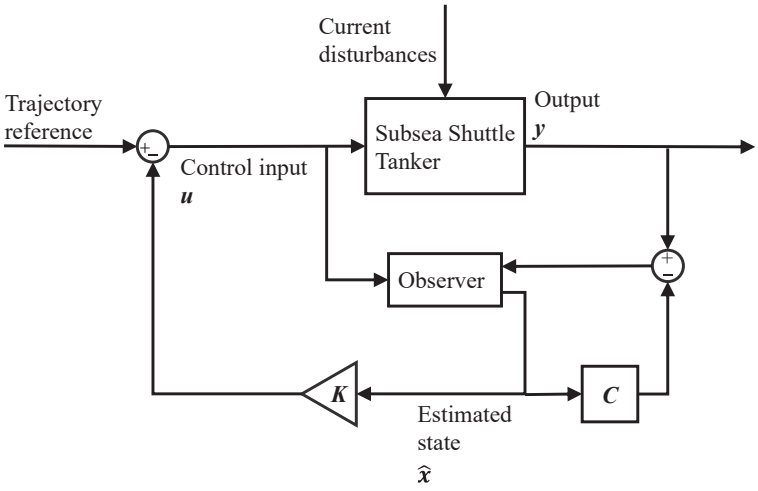

Figure 5.4: Simulink model implementation.

5.2 Model Linearisation

5.2.1 Linearisation Process

The SST manoeuvring model is complex due to its nonlinear, coupled, and time-dependent nature. However, to establish a controller gain, getting linearised time-invariant matrices $\boldsymbol{A}$ and $\boldsymbol{B}$ becomes necessary. This entails deriving a linear state-space representation through model linearisation, a process facilitated by the MATLAB model lineariser [119].

In this context, the input to the linearised model is defined as $\boldsymbol{u} = [n_{tf}; n_p; n_{ta}]$, representing the revolution speeds of the front tunnel thruster, main propeller, and aft tunnel thruster. Correspondingly, the model outputs are denoted as $\boldsymbol{y} = [N; D; \theta]$, signifying longitudinal, vertical, and pitch motions. This configuration leads to the determination of the state vector $\boldsymbol{x} = [N; D; \theta; \dot{N}; \dot{D}; \dot{\theta}]$.

The linearisation process is carried out at a specific operating point with a current velocity of 1 m/s (design current speed) and a heading angle of 1°. A subsequent sensitivity analysis is performed to validate the model's responsiveness. Consequently, the matrix dimensions are structured as follows: $\boldsymbol{A}$ is a 6 by 6 matrix, $\boldsymbol{B}$ is a 6 by 3 matrix, and $\boldsymbol{C}$ is a 3 by 6 matrix, as outlined below:

$$\boldsymbol{A} = \begin{bmatrix} 0 & 0 & 0 & 1 & 0 & 0 \\ 0 & 0 & 0 & 0 & 1 & 0 \\ 0 & 0 & 0 & 0 & 0 & 1 \\ 0 & 0 & 2.65 \times 10^{-5} & -1.00 \times 10^{-3} & -1.21 \times 10^{-4} & -1.45 \times 10^{-2} \\ 0 & 0 & 2.87 \times 10^{-6} & -1.32 \times 10^{-4} & -8.91 \times 10^{-3} & 5.18 \times 10^{-2} \\ 0 & 0 & -2.37 \times 10^{-2} & 6.21 \times 10^{-5} & 3.87 \times 10^{-3} & -5.96 \times 10^{-2} \end{bmatrix} \tag{5.5}$$

$$\boldsymbol{B} = \begin{bmatrix} 0 & 0 & 0 \\ 0 & 0 & 0 \\ 0 & 0 & 0 \\ 2.54 \times 10^{-10} & -8.80 \times 10^{-5} & 4.24 \times 10^{-10} \\ 3.84 \times 10^{-6} & -5.25 \times 10^{-9} & 6.40 \times 10^{-6} \\ 7.13 \times 10^{-7} & 0 & -1.19 \times 10^{-6} \end{bmatrix} \tag{5.6}$$

$$\boldsymbol{C} = \begin{bmatrix} 1 & 0 & 0 & 0 & 0 & 0 \\ 0 & 1 & 0 & 0 & 0 & 0 \\ 0 & 0 & 1 & 0 & 0 & 0 \end{bmatrix} \tag{5.7}$$

5.2.2 State-Space Model Linearisation Point Sensitivity Analysis

To create the linear state-space model, the selected current velocity and inflow angle influence the state and input matrices. To better understand these effects, a steady-state sensitivity analysis is conducted. This analysis allows a deeper understanding of how current velocity

and inflow angle variations influence the system's behaviour.

The SST manoeuvring model is linearised at four distinct steady points. Each controller gain is associated with an identity matrix for the $\boldsymbol{Q}$ matrix, while the $\boldsymbol{R}$ matrix is diagonal and the diagonal values are set to $\left[1 \times 10^{-2}; 1 \times 10^{-4}; 1 \times 10^{-4}\right]$ for the main propeller, front tunnel thruster, and aft tunnel thruster, respectively.

All linear state-space models are obtained with a constant current speed of 1 m/s. Additionally, four different current inflow angles (1°, 5°, 10°, and 15°) are selected to investigate the effects of different flow conditions on the system's linear behaviour.

The designed controllers are then put onto the nonlinear SST model for sensitivity study. Figure 5.5 exemplifies a current profile used in the study. A 500-second realisation of the incoming ocean current speed and inflow angle is presented. To test the LQRs designed by the linear models, the mean inflow velocity is defined as 1 m/s and the mean inflow angle is set to 0 rad.

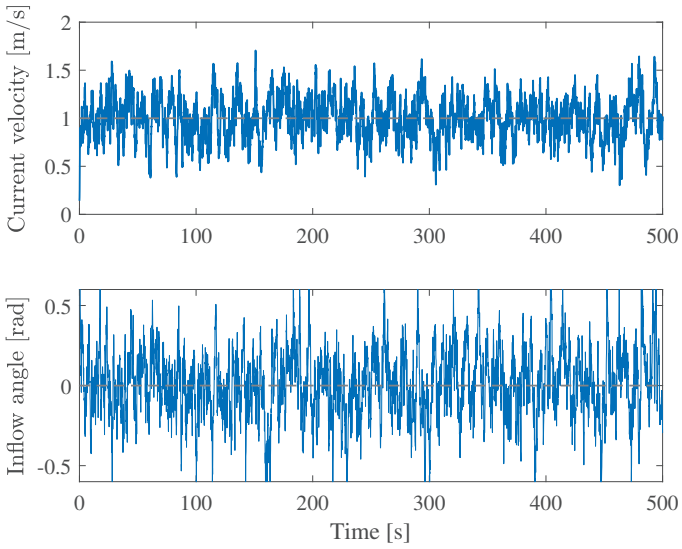

Figure 5.5: Inflow stochastic ocean current 500 s realisation.

Figure 5.6 illustrates the hovering performances of the SST using

the controller gains obtained from the linear state-space model based on the mentioned linearisation points. The same current profile is applied in all cases. Notably, despite the different controller gains, all systems remain stable, demonstrating that the SST effectively maintains its position while hovering. The stability of this closed-loop system does not show sensitivity to the selected linearisation points. However, the linearisation point does impact the heave and surge motions. In the surge motion results presented in Figure 5.6 (up), a transient time of approximately 200 s is observed, during which the current pushes the SST backwards. This steady offset is approximately 1.2 m and remains consistent across all four cases. The amplitude of fluctuation decreases with the linearisation inflow angle, and the minimum fluctuation is observed for $_c$=1°. Notably, linearising at 15° yields significantly worse results in surge motion compared to other cases.

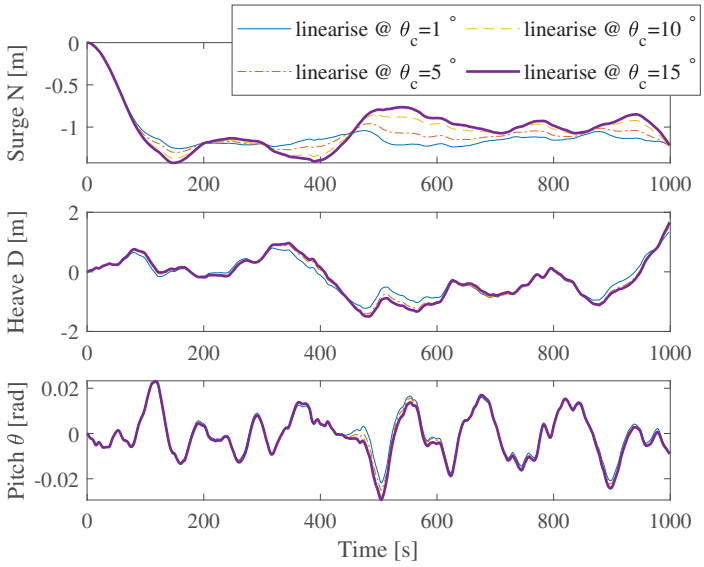

Figure 5.6: SST hovering control performance for LQR designed from state-space models obtained at different linearisation points.

Regarding the surge motion (shown in Figure 5.6), the variation in maximum offset is relatively moderate. Nonetheless, the 15° case

still exhibits the highest maximum response. Among the cases considered, linearising the model at a smaller inflow angle (1°) can result in a controller gain with superior performance in the heave direction.

The SST hovering problem exhibits negligible pitch motion due to the significant hydrostatic restoring force. However, in the 15° case, negative maxima can be observed at 500 s. It is essential to highlight that the SST linear model cannot be obtained when the linearisation point is at 0°. This is because a 0° angle of attack does not capture the contribution from tunnel thrusters. Hence, for this study, the linearised state-space model obtained from linearisation at a steady current speed of 1 m/s and an angle of attack of 1° is used.

5.3 Observer Pole Position Sensitivity Analysis

The SST linear state-space model's observability matrix (***Obs***) is non-singular, with a total column rank of 6. As a result, the poles of the error dynamics can be positioned in the negative half-plane to guarantee stability [47]. However, the desired closed-loop pole positions for the SST observer are not explicitly specified. Therefore, a sensitivity analysis is conducted to determine the observer pole position with minimal error. This section chooses four sets of pole positions, as outlined in Table 3. All closed-loop poles are located in the left half-plane but at varying distances from the origin.

Table 5.3: Observer pole position.

	N	D	θ	$\dot{N}$	$\dot{D}$	$\dot{\theta}$
Pole position 1 (P1)	-0.5	-0.5	-0.5	-0.2	-0.2	-0.2
Pole position 2 (P2)	-2	-2	-2	-1	-1	-1
Pole position 3 (P3)	-4	-4	-4	-2	-2	-2
Pole position 4 (P4)	-8	-8	-8	-4	-4	-4

The results of the four cases, including measurements and actual

motion, are displayed in Figure 5.7. For this simulation, the mean current speed is set to 1 m/s. The state-space model linearised at a 1° inflow angle is selected to provide the best performance. The $\boldsymbol{Q}$ matrix is set to the identity matrix, and the diagonal values in the $\boldsymbol{R}$ matrix are set to $\left[1\times10^{-2}; 1\times10^{-4}; 1\times10^{-4}\right]$ for calculating the controller gain. The Luenberger observer successfully provides measurements for all cases, as the simulation results indicate. However, smaller errors are observed for the observer whose poles are close to zero (Observer P1). On the other hand, the errors in cases P2, P3, and P4 are negligible. Moreover, even when the same pole position is used, a smaller measurement error is found in heave than surge or pitch, as shown in Table 5.3.

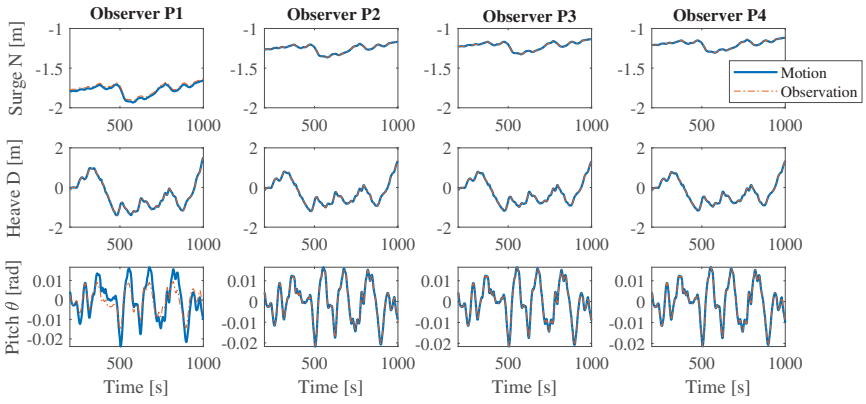

Figure 5.7: Observer performance of cases in Table 5.3.

The observer's closed-loop pole positions influence the performance of the controller. Placing the poles further to the left results in less offset induced in the system. As shown in Figure 5.7, cases P3 and P4 deliver slightly better surge performance compared to P2, with significantly smaller steady offsets than P1. All observer gains exhibit similar results for heave displacement in the same order. However, P2, P3, and P4 outcomes are consistently advantageous over P1. Regarding pitch motion, the differences between the four cases are negligible, as the SST's trim angle is balanced by hydrostatic restoring force

rather than tunnel thrusters.

Figure 5.7 also demonstrates that the performance gap between P3 and P4 is insignificant, indicating that placing pole positions further to the left does not substantially enhance the performance anymore. Consequently, the pole positions in case P3 are chosen to obtain the observer gain as they offer favourable outcomes.

5.4 SST Trajectory Envelope

The SST's designed current speed is set to 1 m/s [23], representing the highest seasonal average current speed observed in the North Atlantic and Norwegian Coastal currents [71–73].

The adapted linearisation is conducted at the operating point with a steady current velocity of 1 m/s design current speed and a fixed 1 ° small-angle heading.

In this study, the trajectory envelope of the SST is investigated under three different current conditions: 0.5 m/s, 1 m/s, and 1.5 m/s. These current speeds correspond to low, designed, and extreme current conditions, respectively. Each simulation is conducted for four hours, corresponding to the typical time span of a loading or offloading operation.

The performance weight matrix $\boldsymbol{Q}$ is set to identity, and the diagonal values in the $\boldsymbol{R}$ matrix are $\left[1\times10^{-2}; 1\times10^{-4}; 1\times10^{-4}\right]$. The time series of surge, heave, and pitch motions of the SST under current speeds of 0.5 m/s, 1 m/s, and 1.5 m/s are presented in Figure 5.8. It is evident from the figure that the closed-loop system is stable. The amplitudes of all motions increase with the mean inflow velocity. Specifically, the largest surge displacements for the three cases are -0.79 m, -1.38 m, and -2.04 m for 0.5 m/s, 1.0 m/s, and 1.5 m/s, respectively.

In terms of heave motion, the maximum observed value is 1.18 m for V_c=0.5 m/s, which increases to 1.70 m for V_c=1.0 m/s and 2.63 m for V_c=1.0 m/s. The pitch motions are not negligible for all three cases,

with maximum values of 0.016 rad, 0.032 rad, and 0.044 rad for 0.5 m/s, 1.0 m/s, and 1.5 m/s current speeds, respectively.

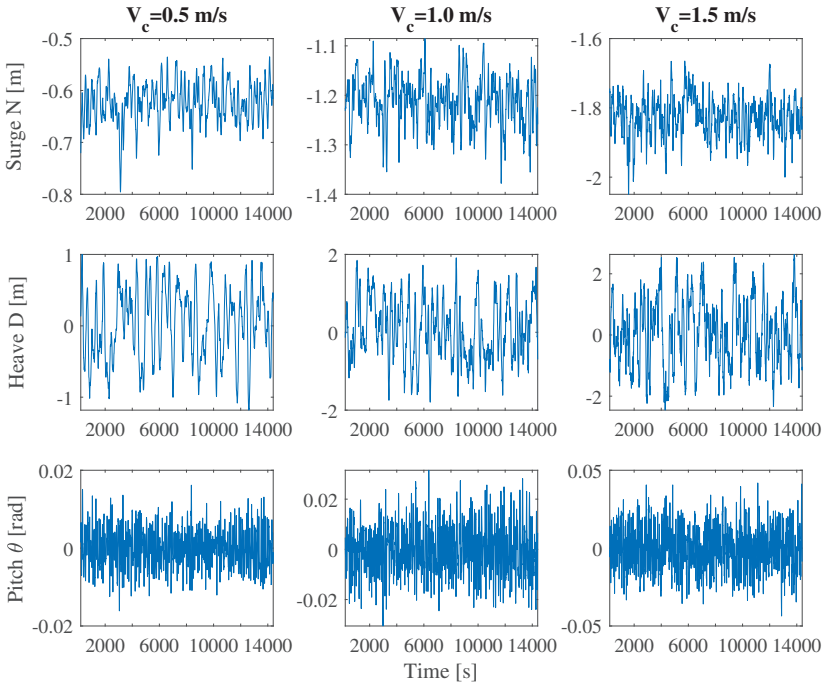

Figure 5.8: Time series of SST motion under three different current speeds.

Figure 5.9 illustrates the required propeller and thruster thrusts during the offloading operation. Due to the SST's slender body with a slenderness ratio of 9.65, its sideways drag is significantly higher than the drag in the heading direction. Consequently, the required thrusts for the tunnel thrusters are also higher than the thrust required for the main propeller.

Figure 5.10 provides a summary of the propeller thrust time series. In the case of a 0.5 m/s current speed, the mean thrust is 4.7 kN, while the maximum required thrust reaches 9.1 kN. When facing a mean inflow speed of 1 m/s, the mean thrust increases to 17.9 kN, with the maximum thrust reaching 37.9 kN. In the extreme current scenario of

1.5 m/s, the average thrust is 40.6 kN, while the maximum required thrust reaches 68.2 kN. These results highlight the substantial thrust demands experienced by the SST during offloading operations in varying current conditions.

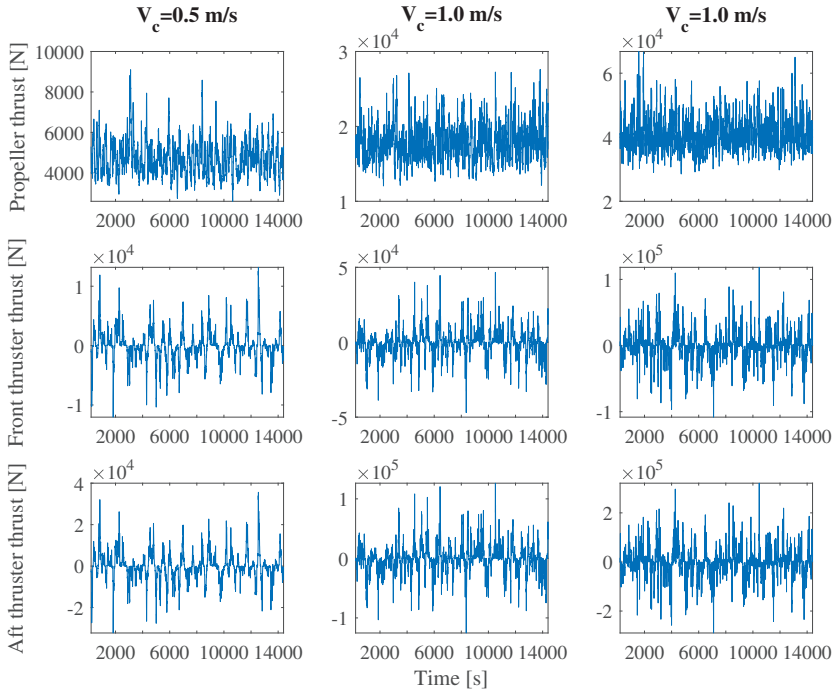

Figure 5.9: Time series of SST motion under three different current speeds.

The required thrusts for the front and aft tunnel thrusters are closely related, showing a high correlation. However, the aft thruster generally provides more thrust than the front thruster. In the four simulations conducted, the highest thrust values are 35.6 kN, 126.3 kN, and 320.1 kN for current speeds of 0.5 m/s, 1.0 m/s, and 1.5 m/s, respectively. The required thrust increases proportionally to the square of the inflow velocity. The existing tunnel thrusters used in other ships [113] are sufficient to meet the thrust requirements of the SST under its designed current speed conditions.

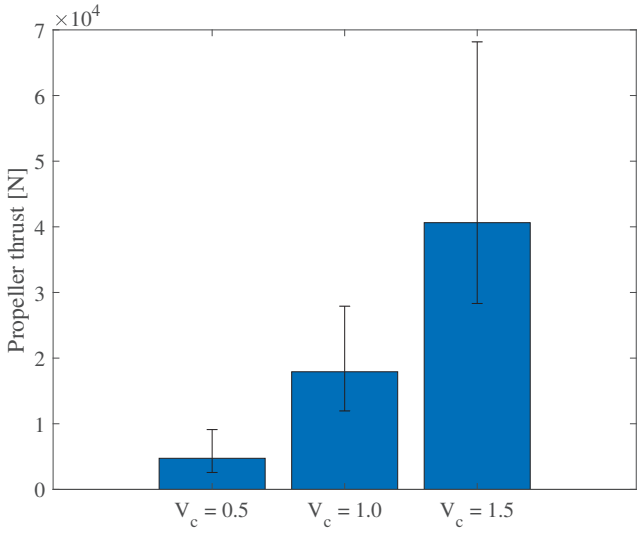

Figure 5.10: SST propeller and thruster mean thrust.

Finally, the trajectory envelope of the SST is presented in Figure 5.11, representing the footprint of the SST during the four-hour simulations. The area of the envelope expands as the mean current speed increases. The heave offset is 1 m, 2 m, and 2.5 m for current speeds of 0.5 m/s, 1 m/s, and 1.5 m/s, respectively. In comparison, the surge motions are relatively insignificant, with the maximum surge offset being -0.25 m for the 1.5 m/s current speed case. The observed motions in the presented cases are relatively negligible, given that the SST has a length of 164 m and a beam of 17 m. As a result, the SST remains stable throughout the entire offloading process.

5.5 Concluding remarks

This chapter applies the proposed SST manoeuvring model and designs an LQR controller for stable hovering. The planar model is developed based on the baseline design geometry to study the SST's vertical position keeping in a current using its propeller and two indepen-

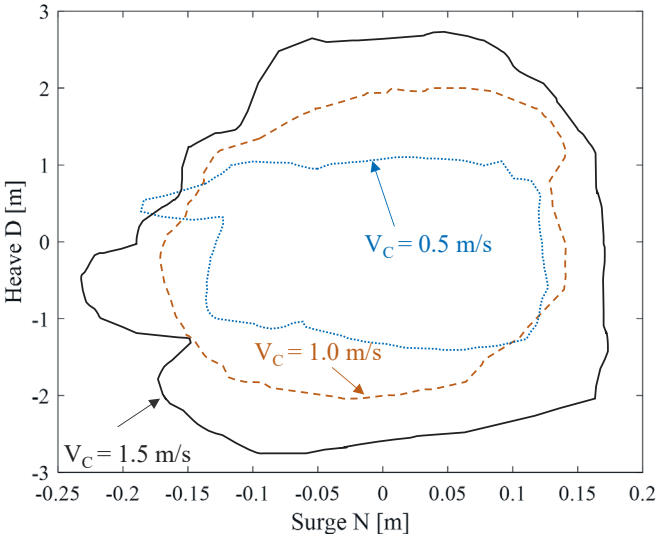

Figure 5.11: Observed trajectory envelope of the SST for four hours.

dent tunnel thrusters. The ocean current profile follows a first-order Gauss-Markov process. The SST motions are measured using a Luenberger observer and then used as input to an LQR controller to calculate the control input. The SST linear state-space model is obtained from four linearisation points, and it is confirmed that the selection of linearisation points does not affect the stability of the closed-loop system. However, choosing a smaller inflow angle of 1° leads to better controller gain performance, but it cannot be reduced to 0° as it does not capture thruster contributions.

The model's controllability and observability are confirmed, with a good measurement provided by the Luenberger observer on heave motion compared to surge and pitch motions. Placing the observer poles further to the negative real axis can reduce the error and improve hovering performance.

The model serves as a basis to address critical questions related to the design and operation of the SST and its associated facilities. Three four-hour time-domain simulations demonstrate that the SST

can maintain its position using its actuators. The tunnel thrusters provide sufficient thrust to cope with the designed current speed of 1 m/s. An envelope of the SST's trajectory during offloading under three different mean current velocities is outlined, with maximum surge and heave motions increasing with current speed.

The developed model opens up avenues for further research studies, including exploring system failure [64] or extreme current speed scenarios [37] and their impact on structural integrity. Extreme loading conditions can be predicted using probabilistic methods to ensure safety in SST design and operation. Additionally, the model can be coupled with dynamic tools like SIMA or OrcaFlex for offloading subsea flowline design [120]. This work enhances our understanding of manoeuvring and contributes to developing extra-large autonomous subsea vessels.

Chapter 6

Extreme Current Hovering Analyses

6.1 Extreme Current

The baseline SST design, intended for deployment in the Norwegian sector of the North Sea, utilises current data from the region. Insights from Pugh's study (1982) [121] are employed to determine extreme current velocities. Pugh's work applied joint tide-surge probability techniques to observational data from Inner Dowsing in the North Sea, resulting in estimates of extreme current distributions and velocities. The summary of the extreme current prediction outcomes is presented in Figure 6.1. The figure illustrates that the highest current velocity occurs in the South-West direction at 165°, corresponding to an extreme current speed of 1.6 m/s with a 50-year return period. This value is subsequently employed as the mean current velocity for generating stochastic current time-domain realisations.

The ocean current realisation is presented in Section 5.1. As depicted in Figure 6.2, a 500-second snapshot of the stochastic current realisation is showcased. The mean current velocity is meticulously set at 1.6 m/s, while the corresponding mean inflow angle remains fixed at 0 °.

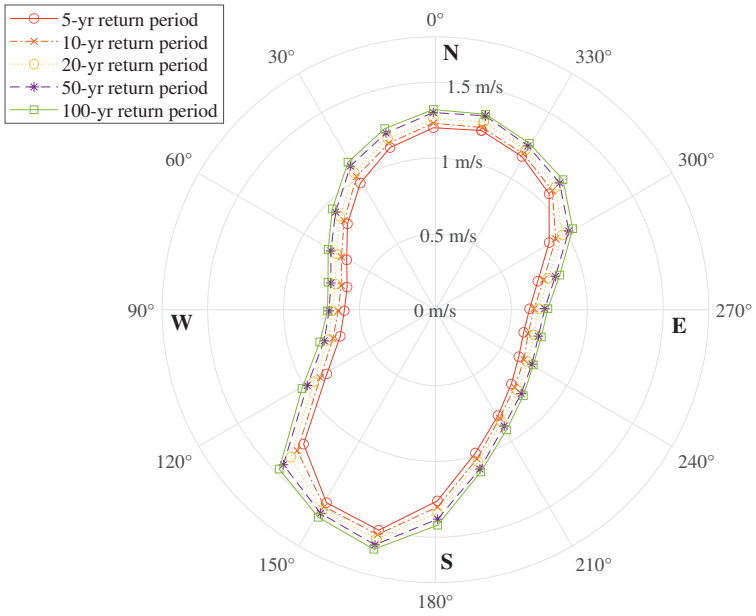

Figure 6.1: Extreme current velocity distribution at Inner Dowsing [116].

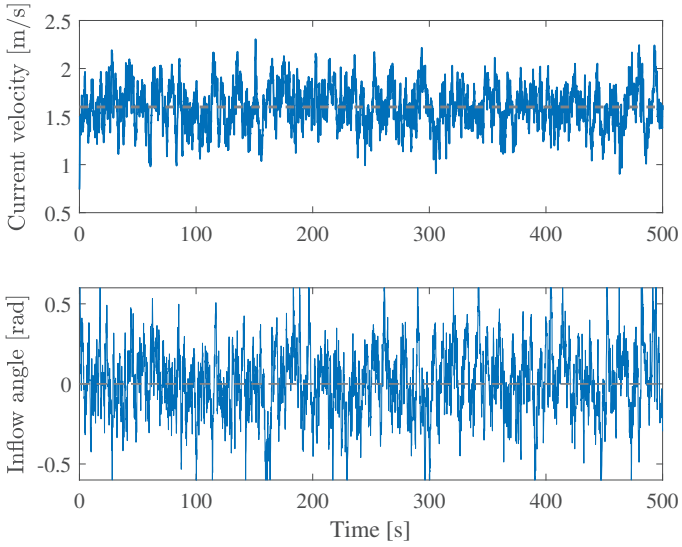

Figure 6.2: Exemplified extreme current realisation.

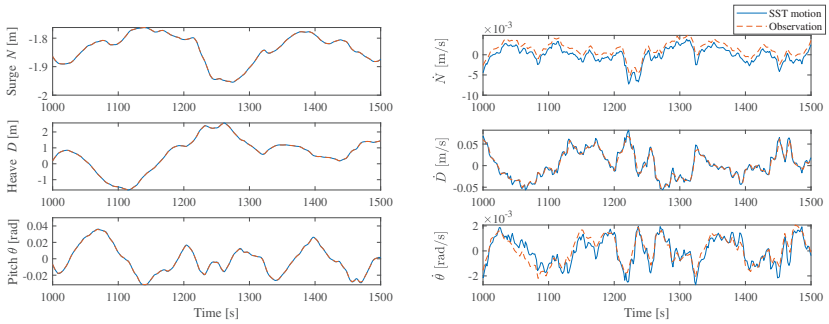

(a) SST Motion **(b)** SST velocity

Figure 6.3: SST response in 500 s realisation.

6.2 Time-Domain Response

An 80-hour realisation is conducted, encompassing 20 independent 4-hour simulations meticulously executed within the Simulink environment (model explained in Section 5.1). The response of the SST is described by the state vector $\boldsymbol{x} = \left[\boldsymbol{N}; \boldsymbol{D}; \boldsymbol{\theta}; \dot{\boldsymbol{N}}; \dot{\boldsymbol{D}}; \dot{\boldsymbol{\theta}}\right]$, is displayed in the global coordinate system, aimed at depicting the performance of both the controller and the observer. Figure 6.3 compares measured and actual states.

Observing Figure 6.3a, it becomes evident that the observer adeptly furnishes accurate measurements for the SST's surge, heave, and pitch displacements. Furthermore, Figure 6.3b illustrates the close correspondence between the observed and actual surge, heave, and pitch velocities. In the illustrated temporal sequence, the SST maintains a consistent surge offset of approximately 1.2 metres and a fluctuation amplitude of roughly 0.2 metres. In contrast, the heave motion of the SST showcases an amplitude of around 2 metres, significantly greater than the surge displacement. This substantial heave motion arises due to the formidable lateral drag force experienced. Meanwhile, the pitch motion of the SST in the presented scenario remains subdued, registering a value lower than 0.04 radians. Notably, this seemingly modest pitch motion can still translate to an over 2-

metre deviation both forward and backward along the vessel's length, given the substantial size of the SST (164 meters). Turning attention to Figures 6.4a and 6.4b, the power spectral density (PSD) of the heave and pitch motions are depicted, respectively. Notably, the heave motion exhibits its peak at a frequency of approximately 5×10^{-4} Hz, corresponding to an eigenperiod of roughly 30 minutes. Likewise, the pitch motion's peak frequency is around 0.017 Hz, equivalently coinciding with an eigenperiod of about 10 minutes. These spectral characteristics provide valuable insights into the dominant frequency components of the SST's heave and pitch motions.

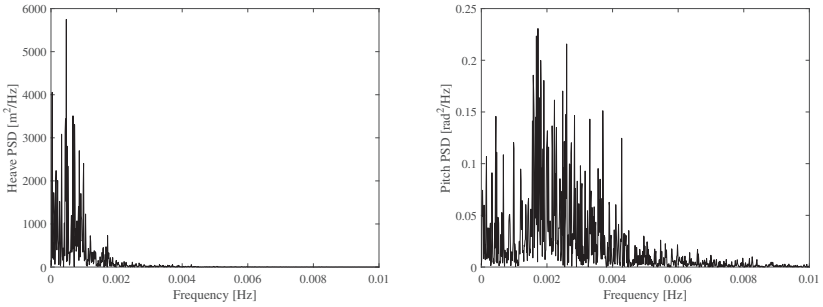

(a) Heave **(b)** Pitch

Figure 6.4: Power spectral density for the (a) heave and (b) pitch of the SST.

Analysing the SST's time series data reveals the responses observed at the five designated measurement points, as indicated in Figure 6.5. The resulting extremities of maximum and minimum depth excursions across 20 realisations are visually represented in Figures 6.6a and 6.6b, respectively. These parameters inherently provide crucial insights into the SST's depth excursion characteristics. Furthermore, they serve as foundational components for predicting the long-term extreme depth variations experienced by the SST. This predictive capability plays a pivotal role in optimising the vessel's design by identifying values contributing to a cost-effective and efficient solution.

The regions experiencing extreme depth excursions are primarily

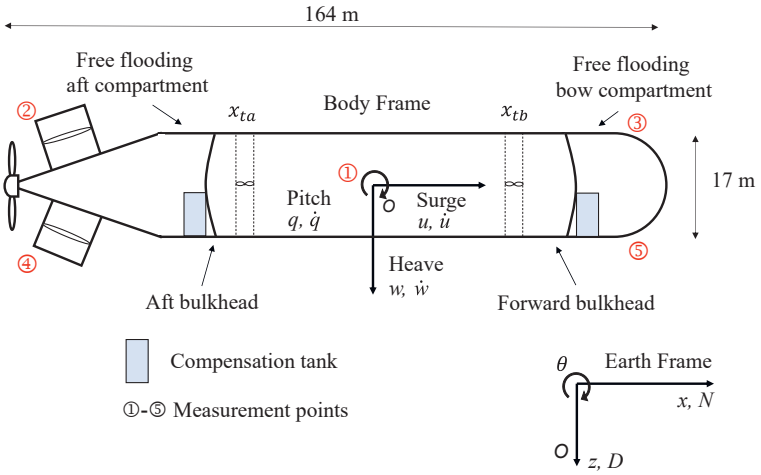

Figure 6.5: SST extreme depth excursion measurement points.

situated at the bow and aft sections of the vessel. This tendency is attributed to the substantial influence of pitch motion at these specific positions. As a result, it is anticipated that the minimum depth excursions will occur at the bow and aft of the upper boundary of the SST, namely Point 3 and Point 2, as delineated in Figure 6.6b. Conversely, the maximal depth excursions manifest at the bow and aft of the lower boundary, denoted by Point 4 and Point 5, as depicted in Figure 6.6a. Measurement Point 1 is strategically located at the centroid of the SST to provide a benchmark for comparison and analysis.

This comprehensive assessment of depth excursions across different vessel regions is invaluable in enhancing our understanding of the SST's behaviour. Furthermore, it guides the formulation of a robust and cost-efficient design strategy, ensuring the vessel's stability and performance throughout its operational lifespan.

6.3 k Value Selection

As discussed in Section 2.4.1 and in accordance with the principles outlined in Naess and Gaidai (2009) [61], the series of iterative condi-

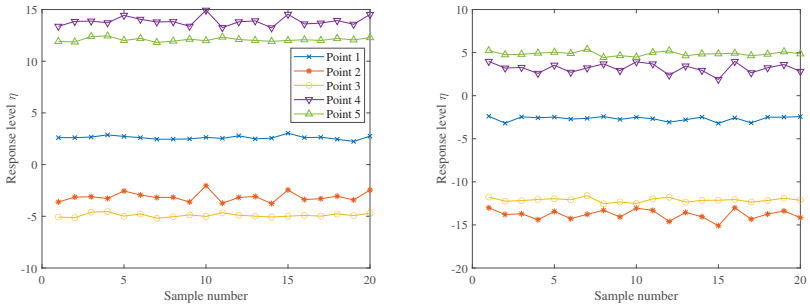

(a) Maximum depth excursion. **(b)** Minimum depth excursion.

Figure 6.6: Maximum and minimum depth off-site for the points of interest in each realisation. Points 1 to 5 are illustrated in Figure 6.5.

tioning approximations, denoted as $P_k(\eta)$, progressively converge towards the ultimate distribution $P(\eta)$ as the value of k increases. This iterative process is explored across varying k values ranging from 1 to 6, yielding insights into the behaviour of the extreme depth excursion for Point 4. The outcomes of this analysis are succinctly presented in Figure 6.7.

Notably, the response parameter η remains consistent across the range of k values from 1 to 6. However, with the same $ACER_k(\eta)$, η is more conservative (larger) for k=1 while the values for $k \geq$2 are very close. Therefore, it is concluded that applying k=2 returns an accurate prediction of the SST extreme depth excursion for the measured points.

6.4 Extreme Depth Excursion Predicted by ACER Method

Within this section, the SST measurement points' extreme depth excursions are studied using the ACER method within the context of the 80-hour simulations. The outcomes of this analysis are briefly showcased in Figure 6.8 and Figure 6.9, with the extrapolation results with

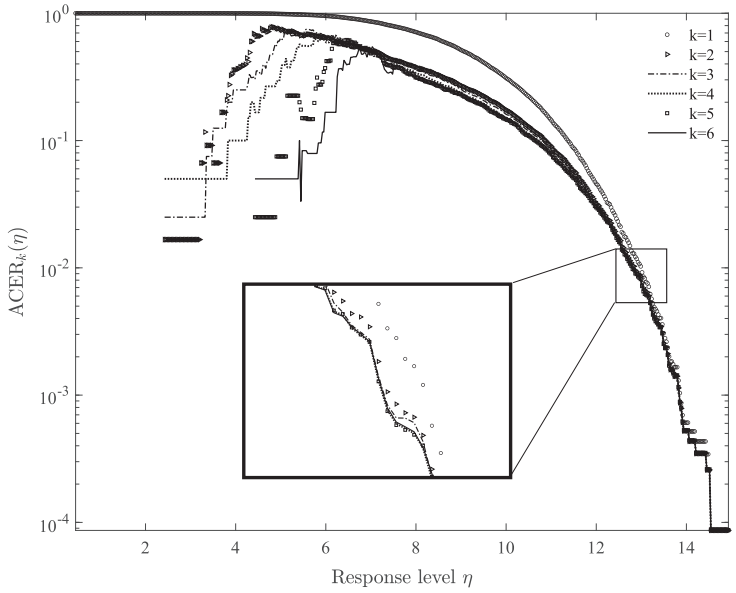

Figure 6.7: ACER functions for maximum depth excursion of Point 4 with different k values.

an exceedance rate of 1×10^{-6}, corresponding closely to a 50-year return period. In both figures, the 95% confidence interval (CI) is illustrated using dashed lines, while the fitted 95% CI is deftly depicted using dotted lines. An alignment with the simulation results is readily apparent when observing the ACER method's performance. This alignment confirms the method's robustness and efficacy.

The minimum extreme response of the SST is observed at Point 2, as shown in Figure 6.8b). The value with a 1×10^{-6} exceedance rate is -16.35 m from the reference offloading position, 2.75 m above the value for the SST bow. As a reference, this extreme value for the SST centroid (Point 1, Figure 6.8a) is -3.74 m. The results indicate that if the SST offloads at 40 m safety depth, the minimum extreme depth excursion is 23.65 m (upper bound).

Figure 6.9 presents the maximum depth excursion extrapolation results. The maximum positive off-site (lower bound) is also observed

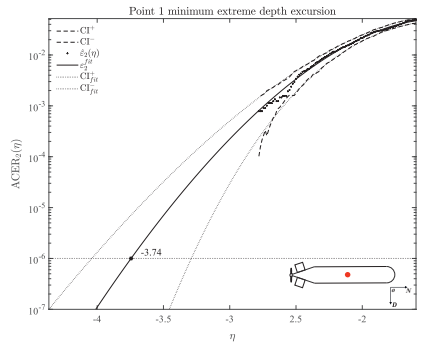

(a) Point 1

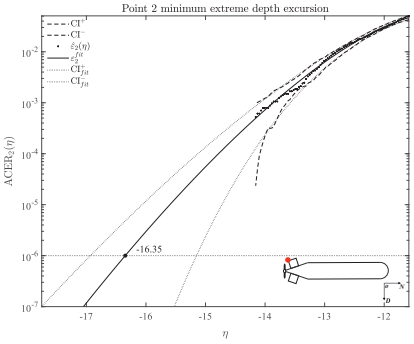

(b) Point 2

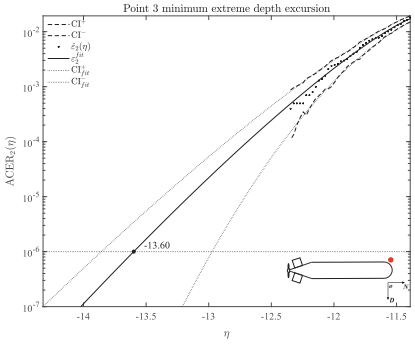

(c) Point 3

Figure 6.8: ACER extrapolation for minimum depth excursion. (a) Point 1. (b) Point 2. (c) Point 3.

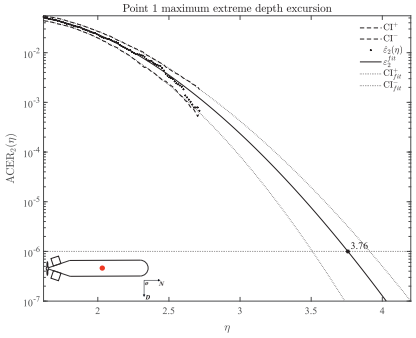

(a) Point 1

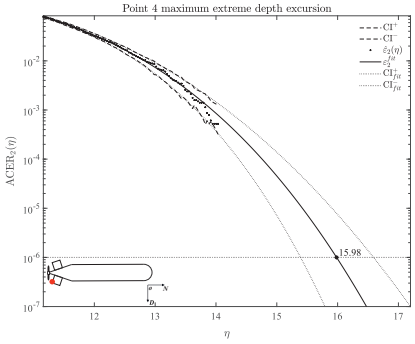

(b) Point 4

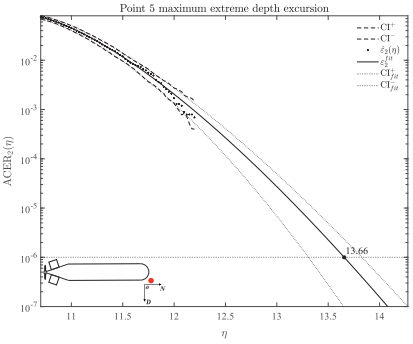

(c) Point 5

Figure 6.9: ACER extrapolation for maximum depth excursion. (a) Point 1. (b) Point 4. (c) Point 5.

at the aft (Point 4, Figure 6.9b). Its value is 15.98 m, slightly lower than the absolute minimum depth excursion (16.35 m). The maximum extreme depth at the SST bow (Point 5, Figure 6.9c) is 2.32 m smaller. The maximum extreme off-site for Point 1 is 3.74 m, as shown in Figure 6.9a, the same as the absolute minimum extreme. Therefore, when the SST is offloading at a 70 m water depth, the maximum depth excursion of the SST with a 1×10^{-6} exceedance rate is 86 m.

Finally, the summation of ACER prediction outcomes is listed in Table 6.1. Meanwhile, Table 6.2 imparts the outcome of extrapolation for 1-year and 5-year motions at designated points 1 and 4.

The key findings outlined in this paper are graphically summarised in Figure 6.10. Within this context, the approved range for offload-

ing depths for the SST comfortably spans from the secure 40 m safety depth to the stipulated 70 m nominal diving depth. To elaborate, the SST's permissible region for offloading depths is situated within 40 m (safety depth) and 70 m (nominal diving depth). However, in extreme current conditions, particularly at 1.6 m/s, the maximum depth excursion can extend to 86 m, while the minimum extreme depth reaches 23.65 m. From a design perspective, it's noteworthy that the maximum depth excursion falls significantly short of the 190 m collapse diving depth, implying that the existing guidelines tend to be overly conservative in delineating the SST's collapse pressure. With a more nuanced understanding of the SST, there is ample room to reduce this value substantially.

From an operational standpoint, several considerations arise. Firstly, when the SST is engaged in offloading operations, it should maintain a minimum distance of 16 m above the upper boundary of any subsea installations to mitigate collision risks. Additionally, the maximum draught of any surface or floating installations must not exceed 23 m, corresponding to the minimum depth excursion when the SST offloads at the lowest allowable operational depth within the SST's operational region. Similarly, in scenarios where the SST is conducting offloading operations in areas with substantial draught from floating structures, a minimum safety distance of 16 m should always be upheld.

Table 6.1: Extreme value responses using ACER method for an exceedance rate of 1×10^{-6}.

Extreme depth	Measurement point	Extrapolation value	95% CI-	95% CI+
Minimum depth	Point 1	-3.74431	-3.28976	-4.04082
	Point 2	-16.3476	-15.1519	-16.9326
	Point 3	-13.5987	-12.9733	-13.8570
Maximum depth	Point 1	3.75786	3.50877	3.91145
	Point 4	15.9833	15.3909	16.5901
	Point 5	13.6554	13.3068	13.8259

Table 6.2: SST depth excursion response predictions with 1-year and 5-year return period.

Point number	Exceedance rate	Equivalent return period	Extrapolation value
Point 2	3.7×10^{-5}	1-year	-15.1
	7.6×10^{-6}	5-year	-15.7
Point 4	3.7×10^{-5}	1-year	15.0
	7.6×10^{-6}	5-year	15.5

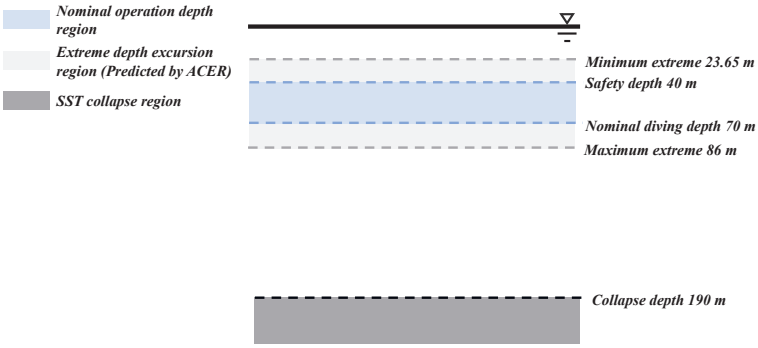

Figure 6.10: Depth region of SST offloading.

6.5 Concluding remarks

Current engineering codes often tend to be conservative, mandating substantial safety factors that lead to overly heavy structural designs. Consequently, obtaining knowledge about the SST's maximum response holds dual advantages in the study of such commercial subsea vehicles. Firstly, understanding the extreme depth excursion reveals the utmost potential deviation from the SST's designated offloading position. This insight reduces uncertainties and facilitates a more robust design approach, thereby decreasing the safety factor embedded in the structural design.

Moreover, the extreme depth excursion furnishes essential information for decision-makers involved in SST operations. This chapter delineates the SST's maximum and minimum deviations from its intended offloading reference point. In the context of offloading activities, it establishes the minimum safety distance for subsea installa-

tions and floating structures.

This chapter studies the extreme response of the SST hovering during offloading. The 2D planar model presented in Chapter 5 is used in this chapter. The mean current velocity is set to be 1.6 m/s, corresponding to observation data in the North Sea with a return period of 50 years. Twenty 4-hour simulations are performed to get the SST response. Then, the extreme responses with the exceedance rate of 1×10^{-6} from 5 measurement points located at the SST centroid, upper-aft, upper-bow, lower-aft, and lower-bow are studied using the ACER method. The main findings are summarised as follows:

- Effect of k value from 1 to 6 is studied, and the result shows that k can provide a very accurate prediction of the SST extreme response during hovering.
- The collapse design of the SST proposed by DNVGL-RU-NAVAL-Pt4Ch1 [70] is very conservative for the SST. The extreme depth excursion happens at the SST aft during hovering, and the maximum depth excursion is 86 m. This means the 19 bar (corresponds to 190 m water depth) collapse pressure can be significantly reduced.
- From an operational perspective, a minimum 16 m safety distance is suggested for the SST hovering. The SST should avoid any subsea or floating structures with a minimum 16 m distance to avoid a potential collision.
- When the SST offloads at a 40 m safety depth, the maximum draught of the floating structures in the vicinity should be less than 23 m.

Chapter 7

Safety Operational Envelope

Severe consequences, including leakage of CO_2 or hydrocarbon, loss of the vessel, and damage to offshore facilities and third parties, can be induced by SST accidents. These consequences can further lead to property loss, pollution or even casualties. Therefore, ensuring safety during SST operation is essential in the design phase. The concept that effectively combines safety and dynamic control for SSTs is the Safety Operating Envelope (SOE). This envelope comprises a set of manoeuvring limits that outline the safe operational boundaries of the system. Due to variations in manoeuvring limits across different systems, the appearance of the SOE can differ. The use of the SOE offers a straightforward approach to assessing the operational safety of various systems, and it has been successfully applied to a diverse range of vessels, including ships [122], submarines, and aeroplanes [123].

The SOE for SSTs draws inspiration from established practices in naval submarines. Its application has been a decades-long practice required by the state-of-the-art DNV naval submarine code [70]. This requirement presents manoeuvring limits on submarine operations, ensuring survivability despite credible failures. There are two ways to depict an SOE [124]. One method employs manoeuvring limitation diagrams, illustrating safety limits on control plane pitch angles. The

other method uses safe manoeuvring envelopes to outline safety limits based on initial trim conditions. This study predominantly presents the safe manoeuvring envelope.

Applying the SOE to submarines is not a novel practice. As far back as 1966, Giddings and Louis studied the emergency recovery of a 150-tonne submarine under conditions of surface jams and flooding [125]. The historical incident involving the INS Dakar submarine in 1968, which encountered an aft plane jam and exceeded collapse depth resulting in casualties [126], further highlights the necessity of the SOE. The impact of the SOE on submarine design and dynamics was explored by Burcher and Rydill [15], who concluded that it significantly influences submarine dynamics and control systems. British defence technology company QinetiQ's research [127] affirmed this impact and highlighted the efficacy of an X aft configuration in controller jams. Additionally, Park and Kim's investigations [128, 129] into submarine depth excursion led to the design of an SOE protection system during an aft control plane jam.

Illustrated in Figure 7.1, a typical SOE for a submarine takes the form of a depth versus velocity diagram. This diagram illustrates the submarine's capability to withstand credible failures, such as flooding or control plane malfunctions. In essence, the SOE acts as a safeguard, minimising operational risks by ensuring that the vessel maintains sufficient manoeuvrability even in the face of predefined failures. Applying this concept to the SST, its safety operating envelope can be delineated into six distinct zones, each with specific characteristics:

- **Jam-to-rise avoid zone:** In this zone, the SST faces the risk of surfacing uncontrollably in the event of a control plane malfunction.

- **Restricted operation zone:** The SST's manoeuvrability is reduced at higher speeds. This zone imposes restrictions on the maximum pitch and control plane angles to mitigate risks.

- **Unrestricted operation zone:** When the SST operates within this zone, it enjoys unrestricted freedom of movement in terms of depth and velocity.

- **Flood avoid zone:** Slow speeds coupled with the presence of water in free-flooding compartments can impede the SST's control planes from generating sufficient lift force. As a result, there is a risk of sinking and surpassing the collapse diving depth.

- **Jam-to-dive avoid zone:** This zone entails the danger of the SST exceeding its collapse diving depth due to a control plane malfunction.

- **Collapse diving depth avoid zone:** This zone pertains to scenarios where the SST operates above its designated nominal diving depth.

By mapping out these zones, the SOE empowers the SST with a clear operational framework that ensures safety and manoeuvrability across considered failure scenarios.

Conducting an SOE analysis proves instrumental for the SST in determining both its optimal service speed and operating depth. This analysis systematically evaluates the feasibility of the SST's service speed, considering potential emergency recovery scenarios. To illustrate, consider the baseline SST, engineered for a deliberate 6-knot slow speed to achieve a remarkable 90% reduction in energy consumption compared to conventional tanker ships [23]. Nonetheless, insights from Figure 7.1 suggest that such a slow speed could make the SST vulnerable during flooding. Consequently, implementing a minimum service speed becomes imperative to ensure operational resilience.

Moreover, the SOE reduces the safety factor currently applied to the SST's structural design, thereby granting the space for expanding its operational depth. In the case of the baseline SST, characterised

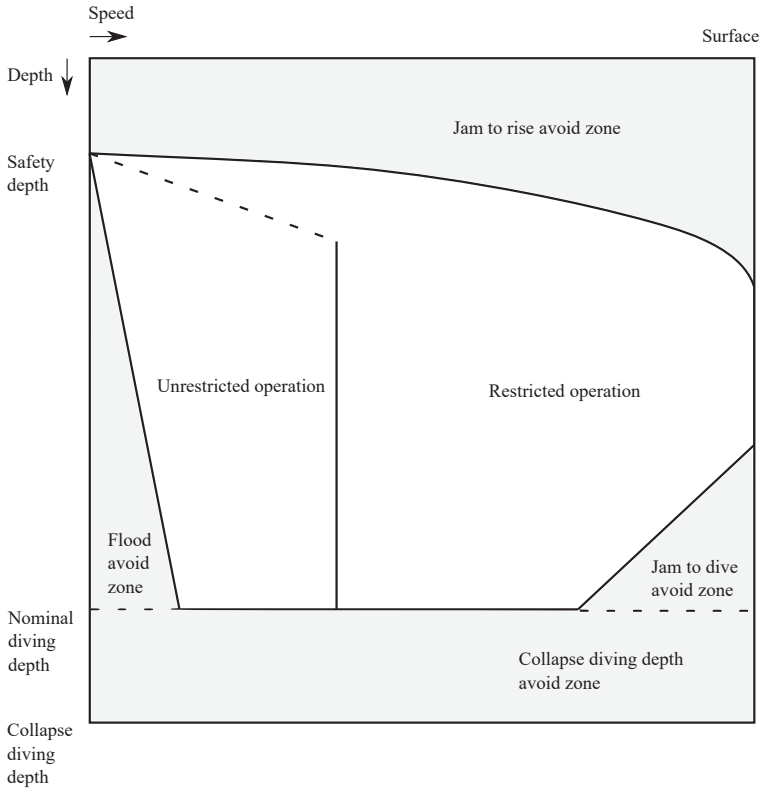

Figure 7.1: Safety Operational Envelope Example.

by a nominal diving pressure of 7 bar (equivalent to 70 metres), adhering to a safety factor of 2.7, as prescribed by the DNV naval submarine code [70], results in an exceptionally high collapse depth estimation of 190 metres – demanding a heavy and complex steel construction. Nevertheless, by comprehensively understanding the SST's recovery behaviour in the event of a malfunction, it becomes feasible to contemplate a reduction in the safety factor from an operational safety standpoint. It is noteworthy that the SOE design remains uninfluenced by the depth and seabed properties. Instead, it empowers decision-makers in determining the most suitable depth and seabed clearance for SST operations.

Contrasting the extensive history of SOE analysis in naval sub-

marines, there remains to be a notable dearth of published applications in the context of commercial submersibles. Moreover, as an innovative merchant vessel, the SST diverges from conventional submarines in numerous facets. Notably, hazards and their effects differ significantly, given that the SST travels slower than naval submarines. Additionally, the SST's distinct structural composition aimed at maintaining a minimum 50% payload relative to its dry weight for economic attractiveness [19] markedly reduces its collapse pressure compared to naval submarines. This makes the SST SOE distinguished from naval submarines. Therefore, this study advances our understanding of SOE analysis for commercial and non-military submersibles, including subsea gliders [32, 130]. It can address the singular challenges presented by such vessels. The framework outlined herein holds promise for application on other novel subsea vessels currently in development, all intending to advance a sustainable and low-carbon maritime sector.

7.1 Model Set-Up

7.1.1 Manoeuvring Simulation Model

The SST manoeuvring model is derived following Section 2.2, and the Simulink model is presented in Section 5.1.

7.1.2 Compensation Tanks Modelling

The SST is equipped with two compensation tanks situated at the bow and aft free flooding compartments, as designed in Chapter 3 and depicted in Figure 3.2. These tanks are ballasted during normal operations. The ballast volumes within these compensation tanks depend on the cargo tank's condition, ensuring neutral buoyancy—a state where the SST's weight matches its buoyancy. During emergency rising manoeuvres, compensation tank blowing is initiated. This tank-

blowing procedure closely follows the established processes used in crewed naval submarines, as extensively documented in references [131–134].

The schematic representation of the compensation tank blowing during an emergency recovery is presented in Figure 7.2. This process unfolds in three steps. First, the high-pressure air system blows compressed air from the air reservoir into the tank. This rapid air injection swiftly increases compensation tank pressure, eventually surpassing the external hydrostatic pressure. Subsequently, the volume of air inside the compensation tank expands, expelling ballast water from the lower portion of the tank. This expulsion of ballast water is a key mechanism in facilitating the SST's ascent. Eventually, the buoyancy force generated exceeds the SST's weight, compelling it to rise to the surface.

Bettle [131] outlines this procedure using an air-volume ratio within the compensation tank. This mathematical formulation for the SST can be expressed as follows:

$$\frac{Vol_a}{Vol_t} = A_1 + \sqrt{A_1^2 + A_2^2} \tag{7.1}$$

$$A_1 = \frac{-p_a - \rho g(z_0 - x_t \sin\theta - 0.45 D_t \cos\theta)}{1.8 \rho g D_t \cos\theta} \tag{7.2}$$

$$A_2 = \frac{m_{a0} C_g T (1 - e^{-tC_b})}{0.9 \rho g D_t N_t V_t \cos\theta} \tag{7.3}$$

where Vol_a is the volume occupied by air inside the compensation tank, Vol_t is the volume of a single compensation tank, N_t is the total number of compensation tanks, p_a is the atmospheric pressure, z_0 is the diving depth, x_t is the compensation tank position along the x-axis, D_t is tank diameter, m_{a0} is the initial mass of the compressed air inside the reservoir, C_g is the gas constant, T is the temperature in compensation tanks, t is the time since emergency recovery action is taken, and C_b is the tank blowing constant. The parameters used in

compensation tank blowing are listed in Table 7.1.

Table 7.1: Compensation tank blowing configuration.

Parameter description	Value	Unit
Compensation tank diameter (D_t)	8	m
Compensation tank x position (x_t)	67.8, -67.8	m
Compensation tank volume (Vol_t)	800	m^3
Atmospheric pressure (p_a)	1×10^5	Bar
Reservoir air mass (m_{a0})	13,000	kg
Gas constant (C_g)	8.31	$kg \cdot m^2 \cdot s^{-2} \cdot K^{-1} \cdot mol^{-1}$
Tank temperature (T)	283.15	K
Blowing constant (C_b)	-0.03	-

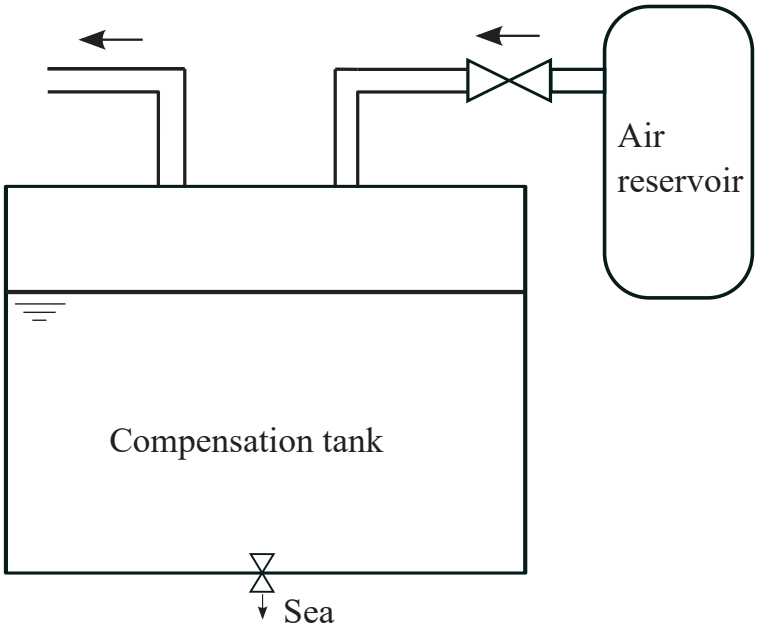

Figure 7.2: Schematic of compensation tank blowing.

7.1.3 Propeller Modelling

A Wageningen B4-70 propeller with a pitch ratio of 1.0 is modelled in this section. The open-water thrust coefficient K_T is derived from the

results of open-water tests [135]. These results are interpolated using an 8th-order polynomial function of the advance number J. The agreement between the interpolated curve and the test data is well demonstrated in Figure 7.3. The polynomial function used for fitting is expressed as:

$$\begin{aligned} K_T = &-2.157J^8 + 5.006J^7 - 1.399J^6 - 4.309J^5 + 2.999J^4 \\ &+ 0.564J^3 - 0.998J^2 - 0.133J^2 + 0.444 \end{aligned} \tag{7.4}$$

The advance number J can be calculated by:

$$J = \frac{1 - w_T}{nD_p} u \tag{7.5}$$

where w_T is the wake fraction, n is propeller rotational speed in revolutions per second, D_p is the propeller diameter, and u is SST surge velocity.

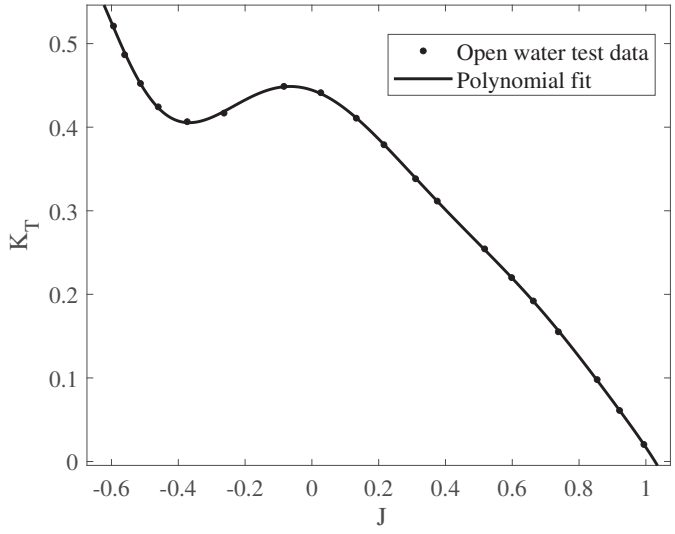

Figure 7.3: Wageningen B4-70 thrust coefficient interpolation.

The propeller configurations are outlined in Table 7.2, and a vi-

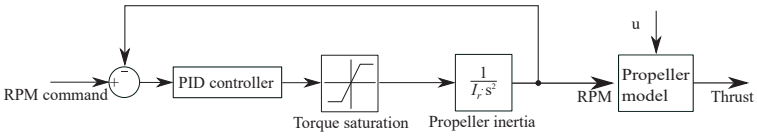

Figure 7.4: Propeller control diagram.

Table 7.2: Propeller configuration used in Chapter 7.

Parameter description	Value	Unit
Selected propeller	Wageningen B4-70	-
Blade number	4	-
Propeller diameter	7	m
Expanded blade ratio	0.70	-
Pitch ratio	1.0	-
Wake fraction	0.47	-
Propeller rotational inertia	4.1×10^5	kg·m ^{2}
Maximum engine torque	2.5×10^6	N·m

sual representation of the propeller model is provided in Figure 7.4 through a block diagram. A PID controller is employed in this model to manage the propeller's behaviour. The PID controller takes both the desired propeller RPM and the actual propeller RPM error as inputs, generating the desired motor output through its computations. Subsequently, a saturation block establishes the maximum threshold for motor torque. Further in the diagram, a second-order transfer function accounts for the rotational inertia resulting from the shaft and propeller. This component replicates any response delay attributed to motor and shaft dynamics, a phenomenon typically encountered when there is a swift alteration in thrust reference. Finally, the real-time thrust produced by the propeller is computed based on the propeller's rotational speed and the SST's surge velocity.

7.1.4 Control Plane Modelling

The influence of control planes on the SST's forces and moments is captured by a linear lift rate coefficient. The control forces resulting

from a single control plane can be computed as follows:

$$X_{\delta c} = -0.5\rho u_{pln}^2 A_c C_{D\delta} \tag{7.6}$$

$$Z_{\delta c} = 0.5\rho u_{pln}^2 A_c C_{L\delta} \tag{7.7}$$

$$M_{\delta c} = 0.5\rho u_{pln}^2 A_c x_c C_{L\delta} \tag{7.8}$$

where $X_{\delta c}$ is control plane drag, $Z_{\delta c}$ is control plane lift, $M_{\delta c}$ is the control plane pitch moment. u_{pln} is the relative velocity at the plane position, $C_{D\delta}$ is the drag rate coefficient, and $C_{L\delta}$ is the lift rate coefficient.

Table 7.3: Hydroplane configuration used in Chapter 7.

Parameter description	Value	Unit
Bow plane position (x_{bow})	45	m
Bow plane area (A_{bow})	50	m²
Bow plane lift rate coefficient ($C_{LB\delta}$)	2.1	-
Bow plane angle rate limit	±5	°/s
Aft plane position (x_{aft})	-60	m
Aft plane area (A_{aft})	28	m²
Aft plane lift rate coefficient ($C_{LA\delta}$)	6.1	-
Aft plane angle rate limit	±5	°/s

7.2 Standard Operation Procedures for Accidental Cases

An SOE is established through a series of simulations encompassing various accident scenarios [129, 136]. As a result, it becomes crucial to figure out Standard Operating Procedures (SOPs) for each specific failure event. When a failure situation arises, the SST must respond according to a predefined set of SOPs. Within this section, SOPs for different accident cases are formulated. Additionally, the criteria for determining successful recoveries versus instances of vessel loss are

established.

7.2.1 Partial Flooding

Flooding in a submarine occurs through systems connected to the sea, typically kept closed. This possibility exists for valves related to SST loading, offloading, or ballast loading. Such flooding is particularly concerning when the SST is travelling at low speeds.

Flooding risks are associated with free flooding compartments, specifically machinery compartments. In this work, an unclosed valve in the aft compartment is considered. When flooding occurs there, three emergency recovery actions are initiated. First, full forward rpm is applied to increase speed. Second, main ballast tanks are blown to enhance buoyancy. Third, the maximum bow plane angle generates lift, facilitating the SST's ascent. From the experiences related to naval submarines, it's noted that unpowered high-rate rising manoeuvres might lead to horizontal instability and significant roll motion [131, 134, 137–139]. Renilson [136] proposes limiting the pitch angle during emergency rising to counter this effect. Additionally, tank blowing should involve all ballast tanks simultaneously, rather than just the forward tank, to maintain stability. In the event of flooding, successful recovery is achieved if the SST reaches the sea surface without surpassing the maximum trimming angle, exceeding the maximum diving depth, or coming into contact with the seabed.

The water flooding rate is calculated as:

$$r_{sw} = \rho A_{fld} \sqrt{2gh_d(t)} \tag{7.9}$$

where r_{sw} is the seawater flood rate with a unit of kg/s, A_{fld}=0.785 m_2 is the opening area, and $h_d(t)$ is SST diving depth at time t. During the simulations, the maximum flooded volume is 600 m^3, as the free flooding area is also divided into small compartments by watertight bulkheads.

7.2.2 Control Plane Jamming

In the event of a control plane jamming, the SST utilises an independently actuated X-plane arrangement. In this system, a single control plane jam is considered a failure mode, leaving the remaining three planes still operational for roll control. This type of failure can result in two potential scenarios: jam-to-rise or jam-to-dive. Each case requires different procedures for emergency recovery. Here are the outlined recovery actions for each scenario:

Jam-To-Rise

If a jam-to-rise failure occurs, the SST executes a crash-stop manoeuvre. This manoeuvre involves two simultaneous actions: initiating a full astern RPM to decrease forward velocity and applying the maximum positive bow plane angle to halt the ascent. Similarly to the recovery action for jam-to-dive, the three aft control planes that remain functional are used to control the vessel's heel angle. In a jam-to-rise situation, the SST is deemed to have successfully recovered if it avoids surfacing too abruptly or surpassing the pitch limit.

Jam-to-dive

In the case of a jam-to-dive scenario, the recovery process comprises two main actions. The first action involves a crash-stop manoeuvre, where the SST commands full astern RPM. The second action centres around pumping out ballast from the forward compensation tank while simultaneously applying the most negative bow control plane angle. These actions collectively generate a positive buoyancy force and diminish the trimming angle of the SST. To qualify as a successful recovery in a jam-to-dive situation, the SST must ascend before contacting the seabed or exceeding the collapse depth. However, it is essential to ensure that the maximum trimming angle is not exceeded as well.

When establishing the Safety Operating Envelope (SOE), a comprehensive set of manoeuvring limits is defined. These limits encompass a range of factors, including depth boundaries, pitch angle thresholds, control plane reaction angles, and the SST's response time. The specific manoeuvring limits incorporated into the SOE are detailed in Table 7.4. Some of the most critical definitions are elucidated as follows:

- **Safety Depth:** The safety depth represents the minimum permissible operational depth for the SST. Operating above this depth poses the risk of collision with large-draught vessels and other offshore structures. The DNV naval submarine code recommends that submarines navigate below water depths of 30-40 meters [70].

- **Nominal Diving Depth:** This depth is the boundary for unrestricted SST operations. The SST is authorized to operate anywhere between the nominal and safety depths. For the SST, this value is defined as 70 meters.

- **Collapse Diving Depth:** The collapse diving depth is of utmost significance as it corresponds to the hydrostatic pressure that aligns with the SST's designed 19-bar pressure. Consequently, this depth has critical implications for the structural design of the SST.

- **Pitch Angle Restriction:** Although the SST operates autonomously and is not subject to human-related constraints, excessively large pitch angles can lead to machinery and equipment malfunctions. This is especially pertinent during high-speed operations, where the SST transitions from the nominal diving depth to the collapse diving depth within a short period. Notably, recommendations from Burcher [15] suggest that submarines generally maintain a maximum pitch angle of around 20 degrees. Furthermore, the pitch limit is confined to 5-10 degrees

during high-speed operations. This study involves the execution of emergency recoveries at initial pitch angles of 10, 15, and 20 degrees.

- **Reaction Time:** The reaction time denotes the duration between the occurrence of a malfunction and the commencement of recovery actions. The elevated autonomy level of the SST significantly reduces reaction times from seconds to milliseconds. Consequently, the SST responds instantaneously to failures.

Table 7.4: SST manoeuvring limitations.

Parameter description	Value	Unit
Safety depth	40	m
Nominal diving depth	70	m
Collapse diving depth	190	m
Pitch angle restriction	10,15,20	°
Aft control plane jam angle	15	°
Bow control plane reaction angle	20	°
Reaction time	0	s

7.3 Result and Discussion

This chapter delves into creating a safety operational envelope for a baseline SST. The investigation focuses on three malfunction scenarios: flooding, aft control plane jam-to-rise, and aft control plane jam-to-dive. The study involves conducting a series of 37 free-running tests, utilising various initial pitch angles and 14 different initial speeds. These tests are carried out using Simulink. Each simulation runs for a duration of 1000 seconds to account for the dampening of initial transient conditions and attainment of steady-state conditions. Moreover, this duration proves adequate to capture the utmost depth excursion as well as the minimum depth excursion within each simulation. Subsequently, the time span between the occurrence of the

incident and the successful execution of the emergency recovery action is determined during the post-processing phase.

This section presents detailed discussions of the SOE. These discussions offer a comprehensive understanding of the behaviour of the SST during emergency recovery scenarios triggered by aft compartment flooding, jam-to-rise, and jam-to-dive events. Following this, the study explores the SST's manoeuvring constraints across a wide spectrum of depths, pitch angles, and velocities. This examination leads to establishing a desired range for depth and speed, which forms the basis for defining the SOE.

7.3.1 Aft Compartment Flooding Recovery Response

Figure 7.5 presents the SST's depth excursion and pitch motion after flooding occurs. In this simulation scenario, the SST starts with an initial speed of 0 m/s, implying that the flooding incident transpires immediately after the SST's subsea well offloading. The SST's initial depth is 114 m during offloading. The time series depiction reveals that the flooding incident commences at t = 50 s, triggering an instantaneous recovery action by the predefined SOP. This recovery process unfolds over approximately 150 s. Initially, within the first 50 s, the SST's descent accelerates. Subsequently, around t = 100 s, the effects of the recovery action become evident, slowing down the descent. Eventually, at t = 205 s, the SST reaches its maximum depth of 190 m. After this point, the descent halts, and the SST begins to ascend, successfully avoiding vessel loss. Regarding pitch behaviour, as the flooding occurs at the aft of the SST, the weight distribution shifts, inducing a negative pitch moment. Consequently, the pitch angle rapidly increases right after the incident. However, due to the enhanced hydrostatic restoring moment, pitch angle stabilisation is observed as time progresses.

Figure 7.5b presents surge and heave velocities measured in the

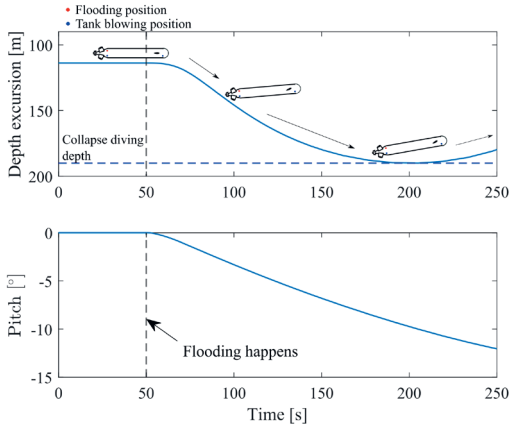

(a) SST motion

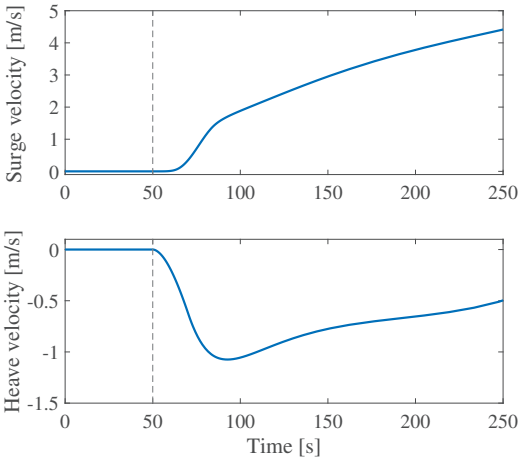

(b) SST velocity

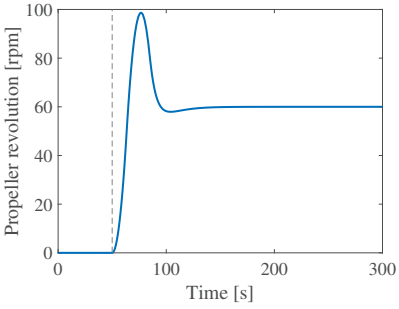

(c) Propeller response

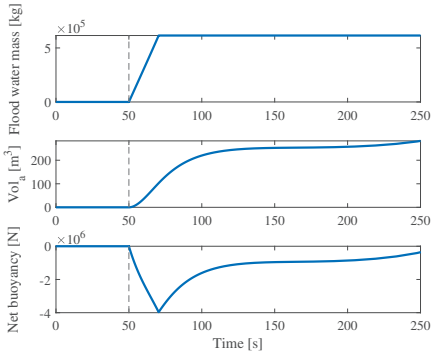

(d) Compensation tank condition

Figure 7.5: SST responses during emergency recovery from flooding.

body-fixed reference frame. Notably, both surge and heave velocities begin at 0 m/s during the initial 50 seconds. Figure 7.5c displays a propeller command of 60 rpm issued at the incident's occurrence. The propeller, controlled by a PID controller, notably introduces a 10-second surge velocity delay due to the SST's significant inertia. The propeller thrust plays a vital role throughout the recovery process, propelling the SST upwards during negative pitch angles. The heave velocity remains consistently positive due to the SST's weight exceeding its displacement after flooding.

Figure 7.5d shows the flooding and compensation tank blowing process. Under 11.4-bar hydrostatic pressure, a 600 m^3 compartment fills with seawater in a mere 20 seconds. The efficiency of the tank blowing depends on the hydrostatic pressure, determining the blowing rate and maximum volume. At a depth of 190 m, a single compensation tank can blow 258 m^3, equivalent to 265 tonnes of seawater. While tank blowing alone may not fully counteract flooding at greater depths, it does contribute to moderating the descent speed.

7.3.2 Jam-To-Rise Recovery Response

Figure 7.6 illustrates the SST's response during a jam-to-rise incident, with an initial speed of 3 m/s and a pitch angle of -15 °. This scenario involves the aft control plane jamming, necessitating immediate recovery actions such as the propeller's emergency brake application and the maximum bow control plane angle command order.

In Figure 7.6a, the SST's heave and pitch motions are depicted. Prior to the jamming, the SST is ascending at a pitch angle of -15 °. Following the incident, the SST's recovery is deemed successful if its ascent halts before breaching the water's surface. In this case, the process takes approximately 170 seconds, with the incident occurring at t = 55 s and the ascent ceasing at t = 225 s. The minimum depth excursion is recorded at -38.5 m, just 1.5 m below the surface. Throughout this period, the pitch angle gradually increases from -15° to -4°.

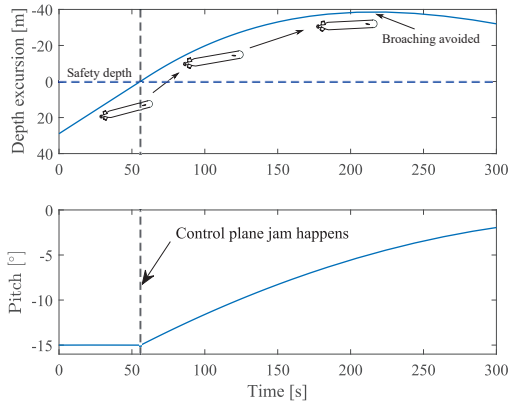

(a) SST motion

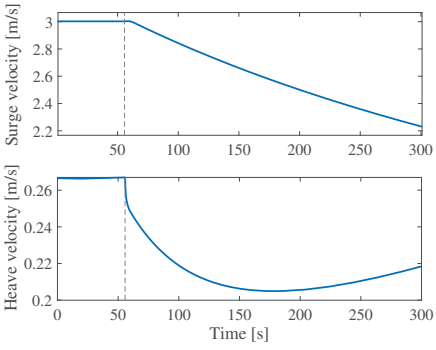

(b) SST velocity

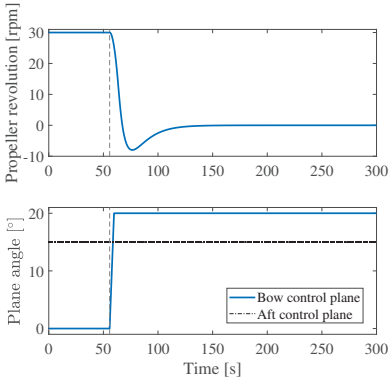

(c) Propeller and plane response

Figure 7.6: SST responses during emergency recovery from jam-to-rise at 3 m/s service speed.

In Figure 7.6b, the surge and heave velocities are displayed in the body-fixed reference frame. The surge velocity diminishes from 3 m/s to 2.2 m/s over the timeframe. The heave velocity remains consistently positive in the body frame throughout the process. Figure 7.6c provides insights into the SST's propeller revolution, bow control plane angle, and aft control plane angle during the recovery. The propeller exhibits a sluggish response due to its substantial rotational inertia. The propeller rpm drops from 30 rpm to 0 rpm within 17 seconds initially, overshooting to -7 rpm, and subsequently returns to the ordered revolution speed at t = 135 s. The aft control planes become jammed at -15 °, while the bow control plane angle transitions from 0 to 20 ° throughout the recovery process. This adjustment generates a positive fin lift that aids in stopping the SST's ascent.

Here, it examines the response of the SST in a jam-to-dive recovery scenario at an initial speed of 5 m/s. The incident of jam-to-dive occurs at t = 50 s, and the recovery process takes around 100 seconds. The initial pitch angle is set at 15 ° during the incident. Figure 7.7a visualises the SST's maximum depth excursion and pitch angle throughout the recovery process. The maximum recoverable depth is determined to be 100 m. The SST's descent halts at a water depth of 190 m, commencing from this point. The SST's pitch angle transitions from 15° to 6° over 100 seconds. This adjustment occurs more rapidly compared to the jam-to-rise incident due to the activation of the forward compensation tank's blowing mechanism. The surge and heave velocities in the body-fixed reference frame are depicted in Figure 7.7b. Given the SST's substantial inertia, the surge velocity takes time to decrease to 0. The heave velocity experiences a rapid decrease after the forward compensation tank blowing is initiated, eventually becoming negative at t = 110 s. However, in the NED frame, the SST's diving stops 40 seconds later. Figure 7.7c illustrates the response of the propeller and control planes. At t = 50 s, a command for 0 rpm is issued to the propeller. Subsequently, the propeller's rotational speed rapidly decreases, reaching an astern revolution speed of -25 rpm. This speed

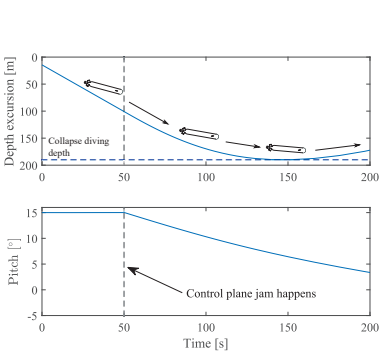

(a) SST motion

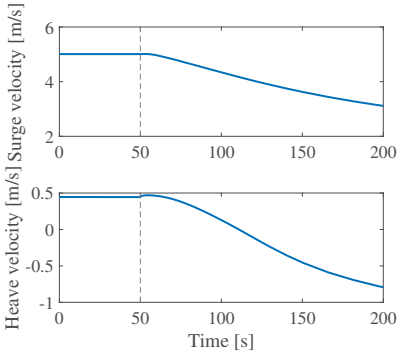

(b) SST velocity

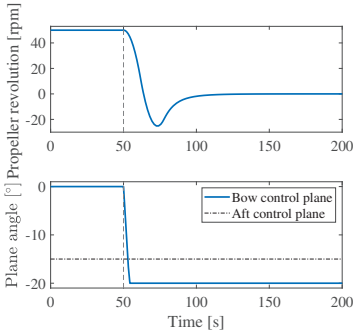

(c) Propeller and plane response

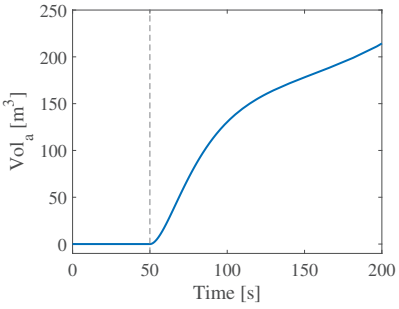

(d) Compensation tank condition

Figure 7.7: SST responses during emergency recovery from jam-to-dive at 5 m/s initial speed.

later increases to 0 rpm around t = 100 s. Concerning the control planes, the bow control plane angle adopts a minimum of -20 ° when the SST is released at t = 50 s. Throughout the process, the aft control plane remains jammed at a maximum -15 ° angle. Figure 7.7d provides insights into the forward compensation tank blowing process. The blow rate (indicated by the slope of the curve) initially decreases as the SST's diving depth increases due to the higher hydrostatic pressure. Subsequently, it increases once again as the SST begins its ascent.

7.3.3 Operation Limitations

The analysis of operation limitations for the baseline SST is presented in this section, based on the results of the 37 simulated cases shown in Figure 7.8

Aft Compartment Flooding: For the SST to be recoverable from aft compartment flooding, it should operate above the flooding limit line, as depicted in Figure 7.8a. This becomes particularly crucial when the SST is moving at a slow speed, as the lift forces generated by the SST body and control planes are limited. The maximum recoverable depth ranges from 80 m when stationary to 110 m at a design speed of 3 m/s. Both these depths exceed the 70-m nominal diving depth of the baseline SST, indicating the ability to recover from aft compartment flooding when operating below the nominal diving depth.

Jam-to-Rise: To prevent broaching the surface when control plane jamming occurs, the SST must operate below the jam-to-rise lines. The results for initial pitch angles of 10 °, 15 °, and 20 ° are presented as solid lines in Figure 7.8. The region of interest lies between 0 m/s and 6 m/s, where the SST is designed to operate efficiently. The 10 ° pitch angle limit does not significantly impact the results in this speed range. However, at speeds exceeding 3 m/s, the pitch angle limit becomes 15 °. Speeds below this threshold allow a 20 ° restriction to

avoid structural and machinery damage rather than just considering control plane jamming.

Jam-to-Dive: For the SST to avoid exceeding the collapse diving depth during a control plane jamming scenario, it should operate above the jam-to-dive lines. Similarly to the jam-to-rise situation, the θ = 10 ° limit does not impact the result due to its speed region not being reached (above 8 m/s). The θ = 20° limitation also does not significantly affect the depth limit, as it is positioned below the flooding limit in Figure 7.8a. Therefore, the θ = 15° limit has the most substantial effect on SST operations. Additionally, the SST remains recoverable from a jam-to-rise incident when operating at speeds below 5 m/s and water depths above 100 m, suggesting that the 70 m nominal operational depth is conservative in terms of recoverability from jam-to-dive situations.

Based on the designed operating velocities and depth limits, an envelope is drawn in Figure 7.8b. This envelope forms the basis for the SOE illustrated in Figure 7.9. This figure encompasses the depth range from 0 m to 190 m and the velocity range from 0 m/s to 6 m/s, encompassing all potential operating conditions of the SST under regular circumstances. A ”broaching avoid” zone within the envelope is defined between 0 m and 40 m safety depth. The SST is permitted to travel below 40 m water depth at a maximum speed of 3 m/s. Beyond this speed, the SST must operate at greater depths to prevent an unrecoverable jam-to-rise incident. The operational zone within the envelope is divided into unrestricted and restricted areas. In the unrestricted area, the SST can recover from the considered malfunctions during various manoeuvres. In the restricted operation area, a maximum pitch angle restriction of 15° is imposed to prevent unrecoverable control plane jam incidents. Additionally, the 70 m nominal diving depth is deemed conservative from a manoeuvring perspective. For the baseline SST travelling at 3 m/s, an operational depth of 100 m is suggested. This range allows the SST to recover from partial flooding incidents or jam-to-dive incidents when moving between speeds of 2

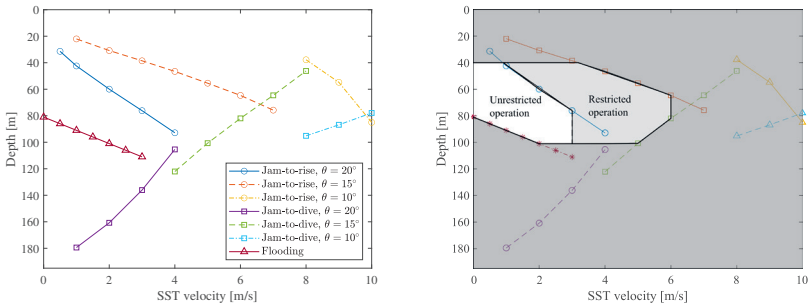

(a) Operation limitations **(b)** SOE

Figure 7.8: Operation limitations and the SOE of the SST.

m/s and 5 m/s (67% - 167% of the designed speed). This effectively covers normal SST operation at a constant speed. Notably, flooding is a significant concern at slow speeds (below 2 m/s), while control plane jamming is more risky at speeds exceeding 3 m/s.

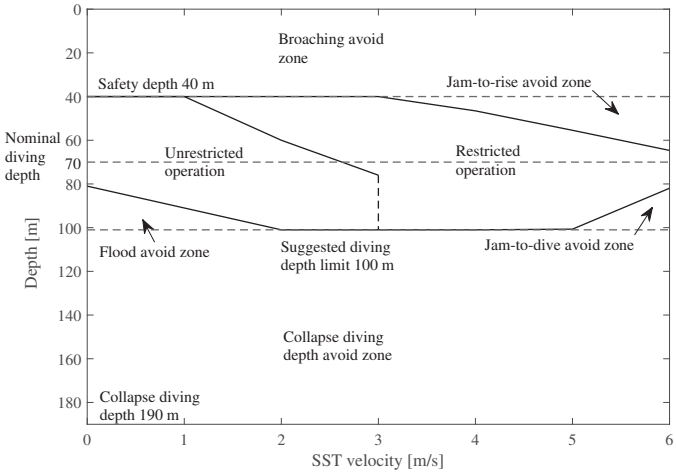

Figure 7.9: Final SST safety operational envelope.

7.4 Concluding remarks

The conclusion of the chapter on the safety operational envelope (SOE) for the baseline SST can be summarised as follows:

The primary objective of this chapter was to establish the SOE for the SST, a critical aspect of its design and operational safety. Although the concept of SOE has long been established for military submarines, it is relatively unexplored in the context of civilian vessels. This paper aims to bridge this knowledge gap and contribute to the safe operation of large subsea vessels.

The conclusions drawn from the study's findings include:

- The SST can prevent surface broaching due to aft control plane jamming when travelling at a 3 m/s design speed, as long as it maintains a 40 m safety depth. If higher speeds are required, the SST must operate at greater depths.
- The SST can safely handle all considered malfunctions when operating at a 70 m nominal water depth.
- To recover from partial flooding, the SST should remain above 80 m water depth during offloading operations.
- The maximum allowable pitch angle for the SST is set at ±15 °. This range ensures recoverability in the event of aft control plane jamming.
- The 70 m nominal diving depth prescribed by the DNV naval submarine code is conservative. The SOE permits the SST to dive to a maximum of 100 m, considering a collapse diving depth of 190 m. This provides operational safety as the SST can recover from critical malfunctions.
- Reducing the safety factor between nominal and collapse diving depths could be considered to reduce the structural weight of the SST, as long as the design remains within the defined SOE.

Chapter 8

CFD Analysis of SST Near-Bottom Operation

Currently, the SST is still in the conceptual study phase. However, conducting experimental studies on such large underwater vehicles at ultra-high Reynolds numbers (Re) is exceedingly costly. Hence, a cost-effective alternative is to employ state-of-the-art Computational Fluid Dynamics (CFD) analysis to gain a comprehensive understanding of the flow around the SST and the forces acting on it.

In this chapter, numerical evaluation is provided for SST under two scenarios:

- SST performs near-bottom voyage in still water (No boundary layer).
- SST hovers facing current (With boundary layer).

The CFD analysis is conducted using the open-source toolbox OpenFOAM [140], employed in numerous submarine hydrodynamics investigations[141–144]. The present study applies the Reynolds-Averaged Navier-Stokes (RANS) method to predict the pressure and skin friction on the SST and its lift coefficient during near-bottom operation. The model is validated with the benchmark SUBOFF-AFF-1 submarine [145]. The results are compared with the experimental data and numerical simulations by third parties [145–149]. In addition,

Richardson extrapolation is performed to obtain the convergence prediction [150–152]. The validation study and Richardson extrapolation are presented in Ma et al. (2023) [39]. The chapter is presented in the following manner: Section 8.1 outlines the model setup and the numerical method. Section 8.2 presents the mesh convergence studies. Section 8.3 presents the results of the CFD analysis on subsea shuttle hydrodynamics during near-bottom operation. Finally, the main findings of this work are summarised in Section 8.4.

8.1 Model Setup

8.1.1 SST Design Configurations Used in CFD Study

The computer-aided design (CAD) model of a 135-metre version of SST is presented in Figure 8.1. This alternative SST design is performed by the University of Stavanger [153]. Some of the preliminary dimensions are unveiled in a CFD study [96]. This chapter's simplified SST CAD model adapts the above-mentioned design. The most critical design configurations relevant to this numerical analysis are presented in Figure 8.2 and summarised in Table 8.1.

Table 8.1: SST design parameters used in Chapter 8.

Design parameter [Unit]	**Value**
Length L [m]	135
Beam D [m]	17
Wetted surface area S_{wet} [m²]	6,768.97
Wetted surface area of the hull S_{hull} [m²]	6,628.37
Wetted surface area of the propeller hub S_{hub} [m²]	140.60
Designed voyage speed [m/s]	3.09
Propeller nozzle diameter [m]	7.22
Propeller hub diameter [m]	2.12
Seawater density ρ [kg/m³]	1,025
Seawater kinematic viscosity ν [m²/s]	1×10^{-6}

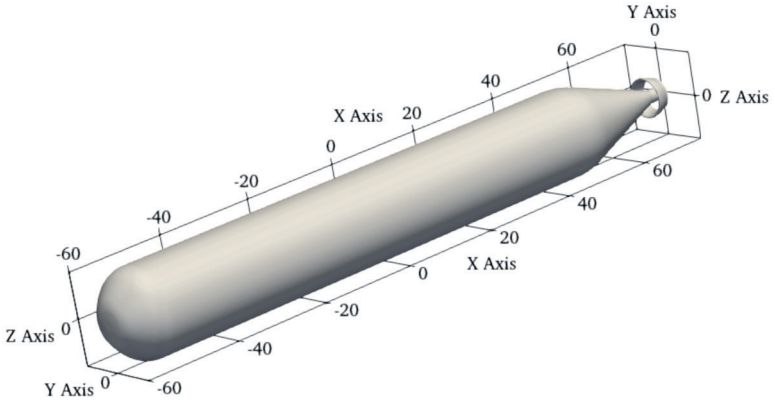

Figure 8.1: CAD model of a 135-metre version of SST, simplified from Equinor subsea shuttle (ref: Figure 1.8 [19, 96])

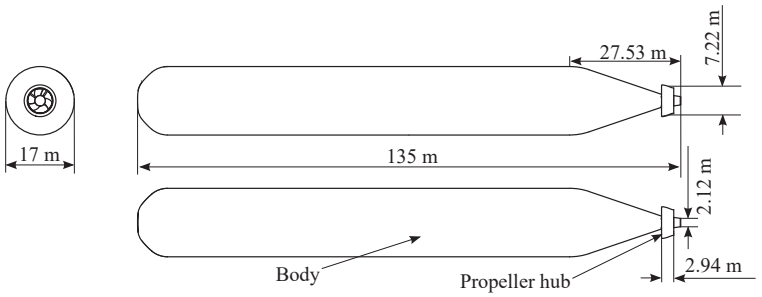

Figure 8.2: The three views with general dimensions of the 135 m SST, design configurations summarised in Table 8.1.

8.1.2 Numerical Scheme

The open-source CFD toolbox OpenFOAM [140] is used in this work to conduct numerical analyses on the hydrodynamic performance of the SST. The Navier-Stokes equations are discretised using the finite volume method. To maintain flow incompressibility, the Semi-Implicit Method for Pressure Linked Equations (SIMPLE) algorithm is employed to solve the pressure-velocity coupled equations. Table 8.2 summarises the discretisation schemes utilised for each term of the governing equations and the residual of the equation interactions.

Table 8.2: Numberical scheme configuration.

Configuration name	Configuration value
Gradient scheme	Gauss linear
Divergence scheme	Gauss linear
Laplacian scheme	Gauss linear
Surface-normal gradient scheme	Limited, non-orthogonal contribution does not exceed the orthogonal part
Cell-to-face interpolation scheme	Linear
Pressure, velocity, k, and ω solver tolerance	10^{-6}

8.1.3 Computational Domain and Grid

The computational domain for the study is represented in Figure 8.3, with Figure 8.3a showing the front view and Figure 8.3b and Figure 8.3c showing the side view. The domain dimensions are given in terms of the SST diameter (D) and length (L). The domain's height and width are set to $35D$, and the length is set to $10L$. The gap (G) represents the distance between the SST bottom and the seabed (marked as "bottom" in Figure 8.3). The boundary conditions and setups for the simulated cases are listed in Table 8.3 and are described as follows:

- At the bottom: For the first scenario where the SST moves with a forward speed in still water, the bottom boundary condition is set

to no-slip, and the bottom boundary moves at velocity U_∞ in the positive x-direction to simulate the forward movement. For the second scenario, where the hovering SST is exposed to a current, the bottom boundary remains fixed, and a no-slip condition with $(u, v, w) = (0, 0, 0)$ is applied.

- Velocity inlet: A boundary layer profile is implemented at the inlet for both cases and the second scenario.
- Outlet: A fixed pressure of zero is set as the boundary condition.
- Sides (two lateral sides and the top side shown in Figure 8.3): Zero gradient boundary conditions are applied.
- The surface of the SST: A no-slip boundary condition is set, and the standard wall function is applied for k and ω.

Table 8.3: Case setups in the present study.

Parameter	Convergence study	Still water with forward speed (Moving bottom)	Heading current hovering near the seabed (Fixed bottom)
G/D	17	0.2, 0.3, 0.5, 0.7, 1	
U_∞	3.09	0.51, 1.03, 3.09	0.58, 1.17, 1.79, 3.54

Figure 8.4 displays the mesh grid surrounding the SST, which corresponds to Mesh 2 as listed in Table 8.4 in Section 8.2. The boundary layer mesh is generated by extruding the surface mesh to ensure high-quality prism cells in the near-wall region. The mesh is further refined in the wake and near the seabed and gradually becomes coarser away from the hull to reduce computational cost.

8.1.4 Seabed Boundary Layer Setup

The fully developed boundary layer velocity profiles are obtained through one-dimensional precursor flow simulations. These profiles

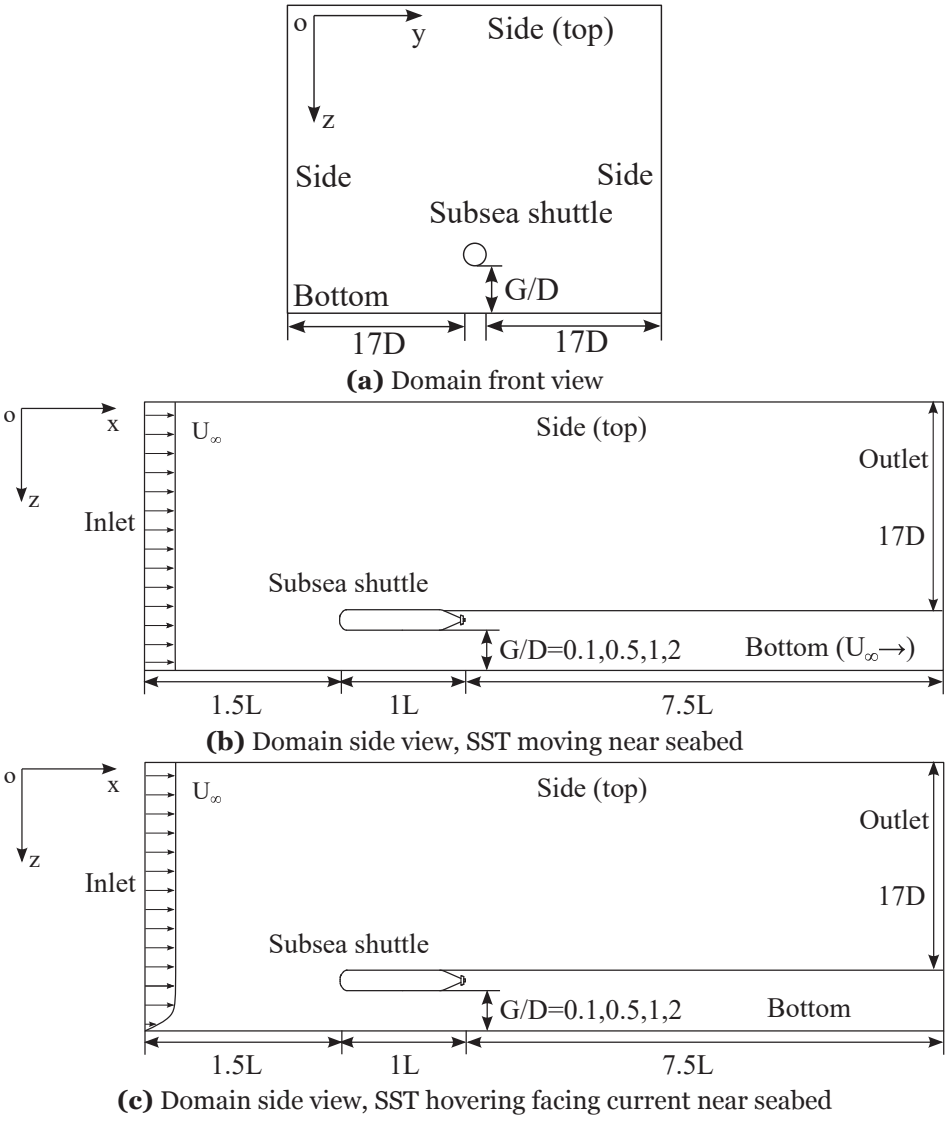

(a) Domain front view

(b) Domain side view, SST moving near seabed

(c) Domain side view, SST hovering facing current near seabed

Figure 8.3: Schematic of the computational domain and boundary conditions for SST near seabed operation.

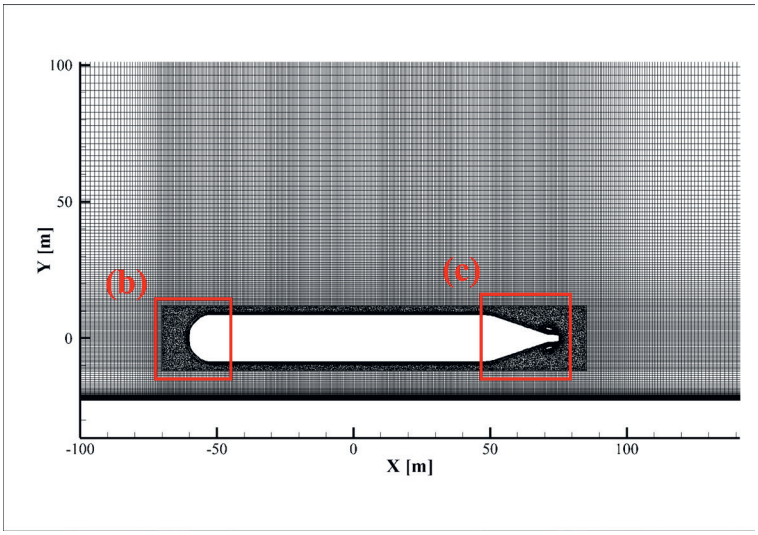

(a) SST

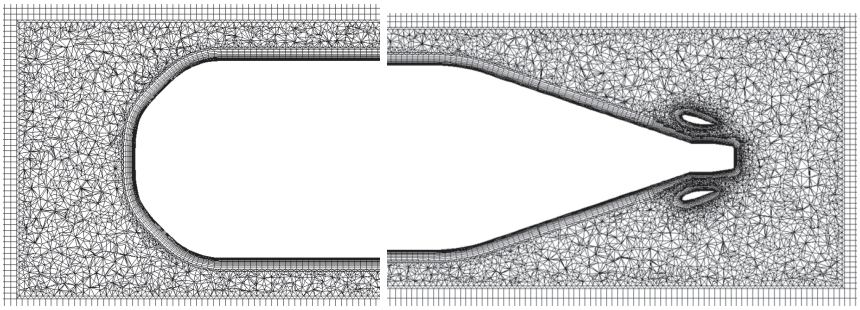

(b) SST bow **(c)** SST aft

Figure 8.4: SST computational mesh view. Note: Positive y-axis points upward in this figure.

are then applied to the inlet as velocity boundary conditions, as shown in Figure 8.3c. In the precursor simulation, a body force P_b is utilised to drive the flow, and it is determined as follows:

$$P = \frac{U_*^2}{h} \tag{8.1}$$

where U_* is the friction velocity. It is obtained by a given freestream velocity from the flow resistance formula. The equation is given by Eq. (8.2), and h is the height of the domain in the y direction.

$$U_* = \frac{U_\infty \kappa}{ln\left(\frac{30h}{k_s}\right) - 1} \tag{8.2}$$

Eq. (8.2) defines the desired freestream current velocity outside the boundary layer as U_∞, where $\kappa = 0.41$ represents the von Karman constant, and k_s=0.01 m represents the seabed roughness. Figure 8.5 displays the steady boundary layer velocity profiles at the inlet for various freestream current velocities, including 0.58 m/s, 1.17 m/s, 1.79 m/s, and 3.54 m/s.

8.2 Mesh Convergence Study

A mesh convergence study is conducted with three variants of meshes: coarse, medium, and dense, and each of them is generated with a constant refinement factor. The SST is positioned at the centre of the yoz plane in Figure 8.3, with an inflow velocity of U_∞=3.08 m/s representing uniform flow in the x-direction. Zero normal gradient boundary conditions are applied to the sides and bottom, and the resulting Reynolds number is $Re = 4.158 \times 10^8$. Table 8.4 provides a summary of the mesh parameters, and the results of the mesh refinement analysis are also presented.

The mesh refinement analysis shows that relative difference of 1.66% in the total drag force between Mesh 2 (14.68 million) and Mesh

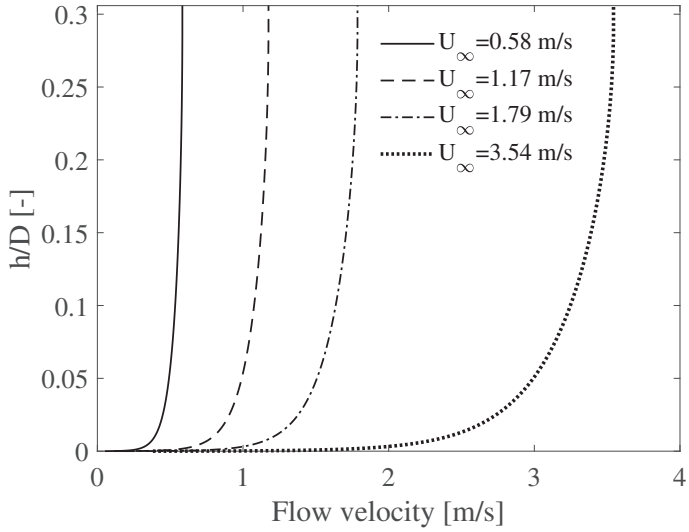

Figure 8.5: Streamwise current velocity profile used as the input for SST hovering cases (Ref. Figure 8.3c).

Table 8.4: Mesh refinement analysis configuration and result.

	Mesh 3 Dense	**Mesh 2 Medium**	**Mesh 1 Coarse**
Number of cells	24.23 million	14.68 million	3.30 million
Total drag [kN]	81.19	82.54	89.84
Total drag relative difference	-	1.66%	8.84%
Pressure drag [kN]	24.60	25.94	33.26
Pressure drag relative difference	-	5.45%	28.22%
Viscous drag [kN]	56.59	56.60	56.57
Viscous drag relative difference	-	0.02%	0.05%

3 (24.23 million). Figure 8.6 presents the (a) pressure coefficient C_p, (b) y^+, and (c) wall shear stress coefficient C_f as a function of non-dimensional length x/L.

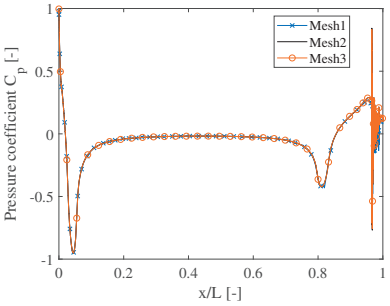

(a) Pressure coefficient C_p

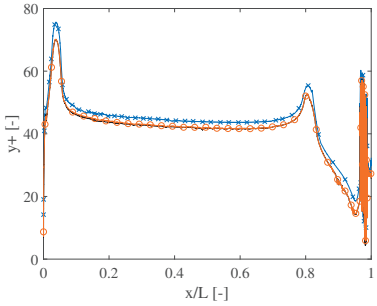

(b) $y+$ value

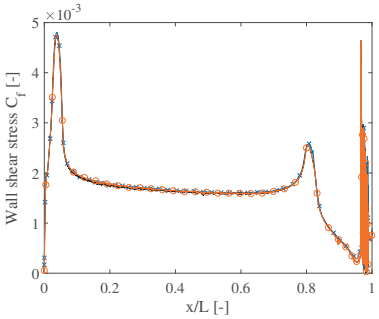

(c) Wall shear stress C_f

Figure 8.6: SST mesh convergence study.

The pressure coefficient C_p is calculated as:

$$C_p = (p - p_\infty)/(0.5\rho U_\infty^2) \tag{8.3}$$

where p is the pressure at the point of interest, p_∞ is the pressure in the freestream.

The non-dimensional wall distance y^+ is given as:

$$y^+ = \frac{\Delta y u^*}{\nu} \tag{8.4}$$

where Δy is the distance between the first grid centre and the wall. u^* is the friction velocity at the nearest wall.

The wall shear stress coefficient C_f is defined as:

$$C_f = \tau_{wall}/(0.5\rho U_\infty^2) \tag{8.5}$$

where τ_{wall} is the wall shear stress

Figure 8.6b displays the distribution of y^+ on the SST hull. The average y^+ value is found to be 39.5, indicating that the SST is in the logarithmic region (30 < y^+ < 100 [154]). The standard wall function is applied at the surface boundary of the SST. The results obtained from the three different meshes demonstrate good agreement on C_p and C_f. Considering the mesh sensitivity study results, Mesh 2 is deemed adequate in providing sufficient grid resolution for the current investigation.

8.3 SST Near Wall Operation Performance

With the above-mentioned simulation schematic (Figure 8.3) and case inputs (Table 8.3), the results of the SST near-bottom operation are presented in this section. For the moving SST cases (Figure 8.3b), the seabed bottom boundary moves at the same speed as the far field in-

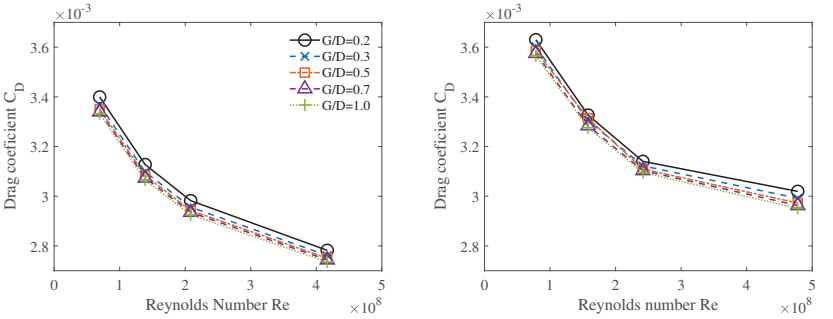

(a) SST moving in still water **(b)** Hovered SST heading current

Figure 8.7: The drag coefficients C_D as a function of the Reynolds number when the SST travels at various speeds.

flow velocity (U_∞), effectively eliminating the seabed boundary layer.

On the other hand, in the case of a hovering SST facing a steady current, the bottom wall boundary remains stationary. The pre-simulated inflow described in Section 8.1.4 is applied to consider the effects of the seabed boundary layer.

This section investigates the effects of flow velocity U_∞ and gap ratio G/D on the hydrodynamic loads acting on the SST. The velocity and pressure contours for the various flow cases under investigation are presented.

8.3.1 Inflow Speed, Gap Ratio and Boundary Layer Effects

Figure 8.7 shows the effect of U_∞ and G/D on the total drag force acting on the SST. The drag coefficient C_D is calculated using Eq. (8.6) from the drag force F_x. It shows a decreasing trend with increasing Reynolds number for all investigated G/D ratios. The gap ratio G/D does not significantly affect C_D. Even though when G/D is reduced, C_D increases, this effect becomes less significant as G/D increases. Notably, as illustrated in Figure 8.7b, considering the seabed boundary layer effect results in substantially higher values of C_D.

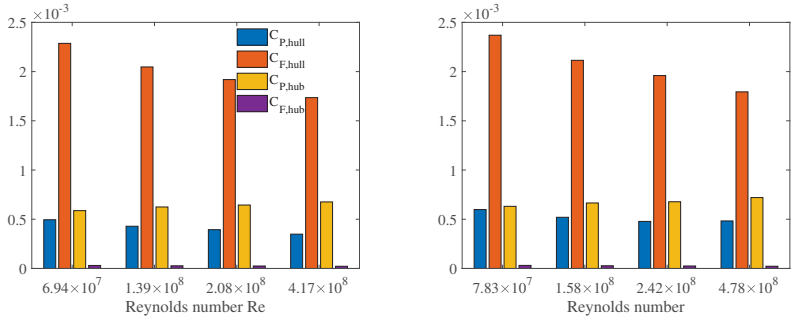

(a) SST moving in still water **(b)** Hovered SST heading current

Figure 8.8: SST drag components at various travel speeds at $G/D = 0.2$.

$$C_D = F_x/(0.5\rho U_\infty^2 S_{wet}) \tag{8.6}$$

The SST is divided into the vessel body and the propeller hub (as marked in Figure 8.2). The pressure drag coefficient C_P is calculated from the total form drag F_{Px}, and the skin friction coefficient C_F is calculated from the total friction drag F_{Fx}, using expressions in Eqs. (8.7) and (8.8). Figure 8.8 presents the contributions of each drag component for the G/D = 0.2 cases. The G/D = 0.2 cases represent other investigated gap ratios, as the effect of G/D on drag is rather small, as shown in Figure 8.7.

$$C_P = F_{Px}/(0.5\rho U_\infty^2 S_{wet}) \tag{8.7}$$

$$C_F = F_{Fx}/(0.5\rho U_\infty^2 S_{wet}) \tag{8.8}$$

For both Figures 8.8a and 8.8b, it can be observed that the hull viscous drag is the dominant contribution, varying between 67% of total drag for U_∞ = 0.514 m/s (1 knot) to 62% of total drag for U_∞ = 3.09 m/s (6 knots). The contribution of pressure drag is less significant, as the SST has a slender, streamlined shape without sharp corners. The

hub pressure drag is larger than the hull pressure drag, comprising approximately 17.7% to 24.3% of the total drag. The hull pressure drag is approximately 12.5% to 14.5% of the total drag. The hub viscous drag is negligible, contributing less than 1% to the total drag due to its small wetted surface area.

Figure 8.9 compares the drag coefficients when the SST is moving in still water and hovering near the seabed, and subjected to a current. The pressure and friction drags are higher for the hovering SST case at similar Reynolds numbers.

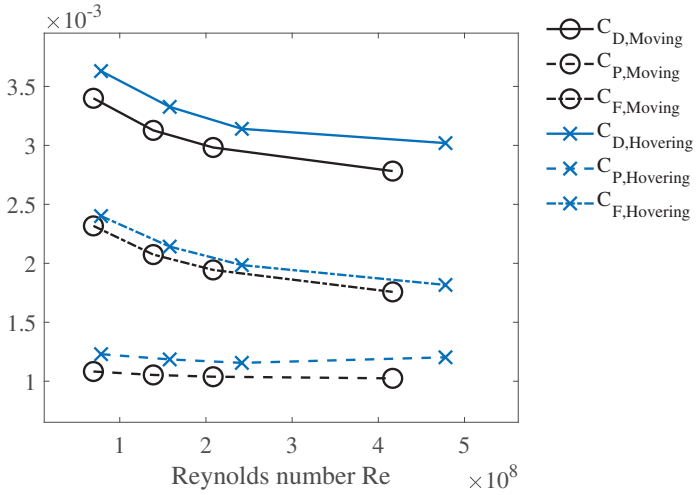

Figure 8.9: C_D, C_P, and C_F as a function of Re with G/D=0.2.

A consistent downward-pointing lift force is observed for all the investigated cases, which aligns with Mackay's findings [25]. This downward force results from a pressure difference between the upper and lower surfaces of the SST, causing it to be pulled towards the seabed. Similar to the drag force, the magnitude of this suction force increases proportionally to the square of the inflow velocity. When the G/D is below 0.3, the suction force surpasses the total drag force in magnitude for all the investigated cases. As the speed increases, the lift force also substantially grows with a decrease in G/D. Table 8.5 compares the drag and lift forces at specific speeds and gap ratios. This ratio be-

tween the lift and drag diminishes with G/D and increases with U_∞.

$$C_L = F_y/(0.5\rho U_\infty^2 S_{wet}) \tag{8.9}$$

Figure 8.10 depicts the lift coefficient C_L calculated using Eq. (8.9) from the vertical force F_y as a function of Re. As defined in Figure 8.3, the positive vertical force points downward. In Figure 8.10a, it becomes apparent that, in contrast to C_D, C_L exhibits relative insensitivity to changes in Re within the investigated range. However, C_L increases substantially with G/D. When the stationary shuttle is subject to an incoming boundary layer flow (Figure 8.10b), the lift coefficient is lower than when SST moves with a forward speed in quiescent fluid. The lift coefficient first increases and then decreases as Re increases, especially for smaller G/D. The lift coefficient becomes almost constant when G/D is above 0.5.

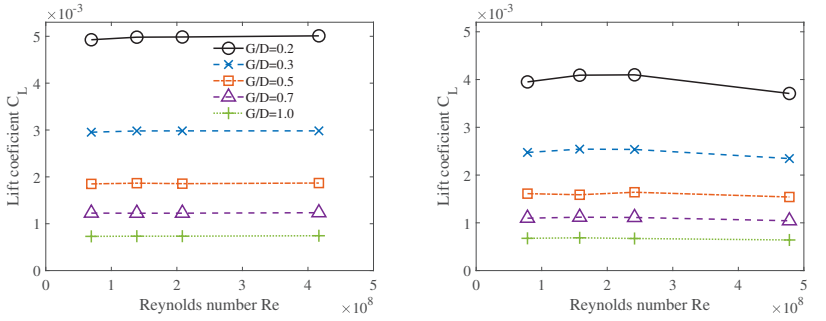

(a) SST moving in still water **(b)** Hovered SST heading current

Figure 8.10: SST drag components at various travel speeds at $G/D = 0.2$.

8.3.2 Velocity Field at Design Speed

Figure 8.11 illustrates the velocity profile between the SST and the seabed at the highest speeds (U_∞ = 3.09 m/s and 3.54 m/s) for the smallest and largest G/D, showing the impact of the boundary layer. A comparable velocity profile can be observed near the SST for both

Table 8.5: Lift force as a percentage of the corresponding drag force for various G/D and U_∞.

SST moving in still water				
	U_∞=0.51 m/s	U_∞=1.03 m/s	U_∞=1.54 m/s	U_∞=3.09 m/s
G/D=0.2	145.9%	159.3%	167.2%	180.1%
G/D=0.3	87.7%	96.2%	100.9%	108.0%
G/D=0.5	55.2%	60.5%	63.0%	67.9%
G/D=0.7	36.7%	39.8%	41.7%	45.0%
G/D=1.0	21.9%	23.9%	25.1%	27.2%
Hovered SST heading current				
	U_∞=0.58 m/s	U_∞=1.17 m/s	U_∞=1.79 m/s	U_∞=3.54 m/s
G/D=0.2	108.9%	123.0%	130.5%	122.8%
G/D=0.3	68.7%	77.0%	81.2%	78.4%
G/D=0.5	44.9%	47.9%	52.8%	51.8%
G/D=0.7	30.7%	34.0%	35.8%	35.2%
G/D=1.0	18.9%	21.0%	21.7%	21.7%

scenarios: when it moves in still water and when it hovers near the seabed with a heading current. Due to the boundary layer effect, the hovering cases exhibit a reduced velocity within the gap, particularly for the small G/D.

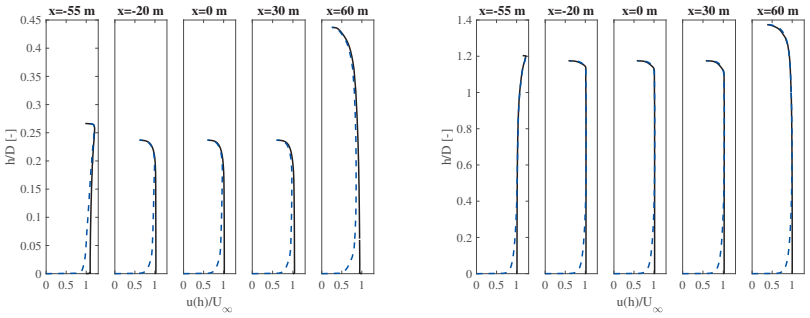

(a) G/D=0.2 **(b)** G/D=1.0

Figure 8.11: The non-dimensional velocity profile between the SST and the seabed. (a) G/D = 0.2. (b) G/D = 1.0. Moving (solid line): the SST moves in the still water. Hovering (dash line): the SST hovers near the seabed while subject to heading current.

Figure 8.12 displays contour plots of the SST's horizontal velocity

on the XoY-symmetry plane. The plots depict cases of the SST travelling near the seabed at a speed of 3.09 m/s (6 knots) with different G/D. In front of the SST, a zone of decelerated flow is observed within approximately -90 m < X < -60 m (marked as A in Figure 8.12a). This decelerated flow zone extends from the bottom surface of the hull to the seabed when the gap ratio is less than 0.5, as shown in Figures 8.12a to 8.12c. The size of this decelerated flow zone decreases with an increase in G/D. For G/D = 0.2, the decelerated flow zone is more pronounced and covers the gap between the SST and the seabed. Additionally, accelerated flow zones are observed at X = ±50 m (denoted as B in Figure 8.12a), and in the tail region, the flow speed decreases at 50 m < x < 90 m (denoted as C in Figure 8.12a).

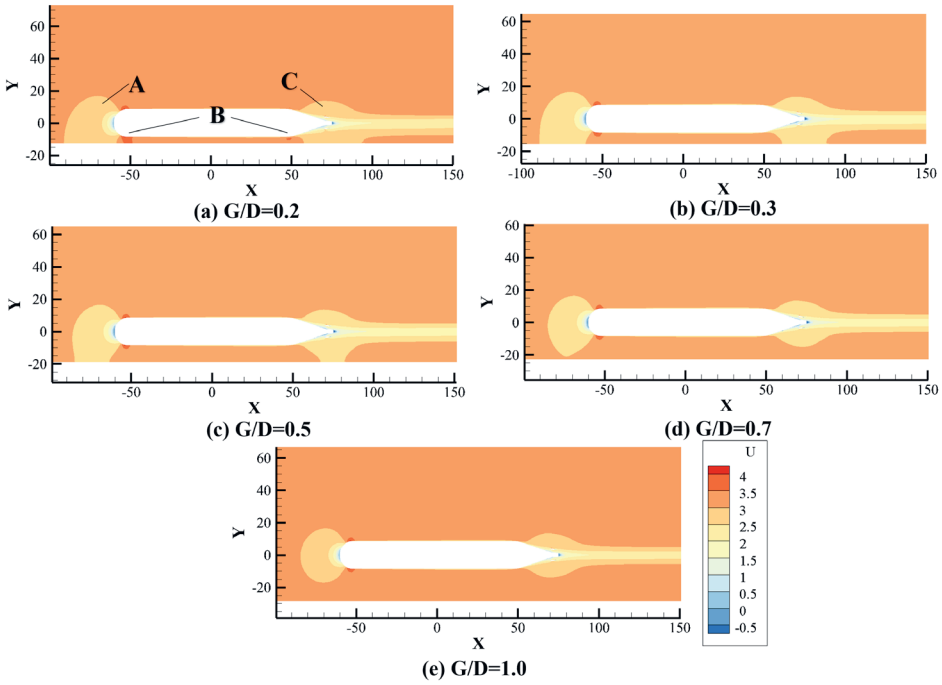

Figure 8.12: Horizontal velocity contours with U_∞=3.09 m/s for different G/D. Units: U [m/s], X [m], Y [m]. Case: the SST is moving in the still water. Note: Positive y-axis points upward in this figure.

Figure 8.13 illustrates the hovering case's velocity distribution around the SST. The boundary layer thickness increases ahead of the SST (point A in Figure 8.13a) due to the decelerating effects of the SST on the incoming flow. The decelerated flow zones located at the bow and tail extend to the boundary layer for all gap ratios (marked as B in Figure 8.13a). Similar to the moving SST case, accelerated flow zones are also observed at X = ±50 m (marked as C in Figure 8.13a). This leads to a reduction in the seabed boundary layer thickness and an increase in the parallel mid-body. Additionally, the boundary layer becomes thicker at the wake region.

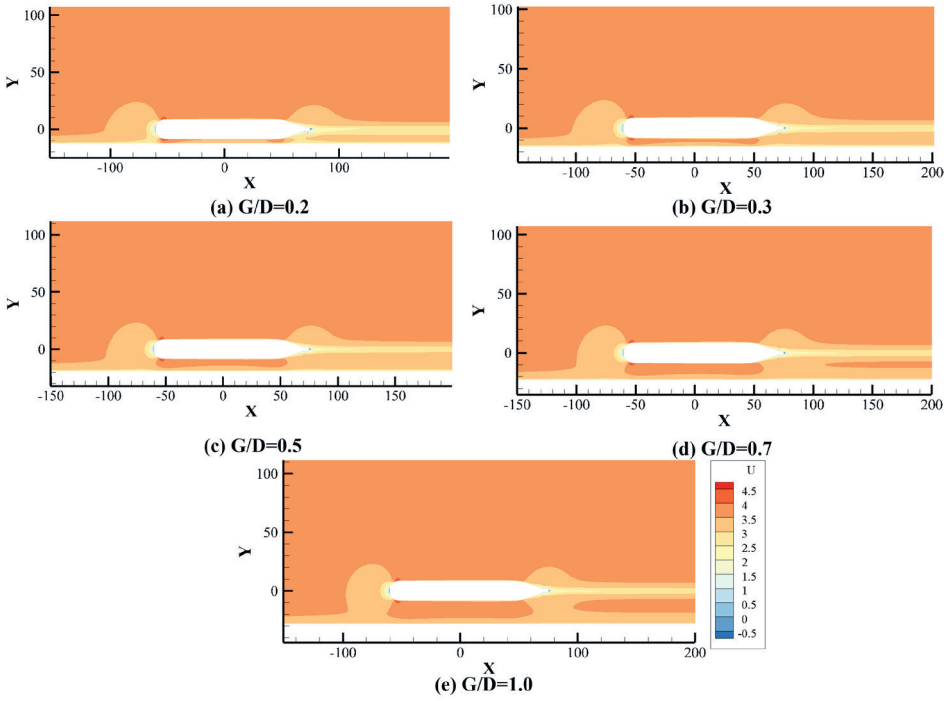

Figure 8.13: Horizontal velocity contours with U_∞=3.54 m/s for different G/D. Units: U [m/s], X [m], Y [m]. Case: the SST faces the current and hovers near the seabed. Note: Positive y-axis points upward in this figure.

8.3.3 Pressure Distribution at Design Speed

Figure 8.14 displays the pressure contours for all investigated gap ratios in the case of an SST travelling at design speed (3.09 m/s = 6 knots). High-pressure regions are observed at the bow and near the tail end. Along the mid-body, the pressure is generally slightly lower than the far-field pressure, with notable low-pressure zones forming near the transition points from the bow (X = -50 m, marked as A in Figure 8.14a) and stern (X = 50 m, marked as B in Figure 8.14a) geometry to the tubular mid-body. At x = -70 m, a high-pressure region forms due to the slowdown of incoming flow when approaching the SST. Conversely, low-pressure zones are formed when the flow is accelerated at x = 50 m. In Figure 8.14a, the high-pressure and low-pressure zones are larger beneath the SST due to the smaller G/D. Combining this with Figure 8.12a, it is evident that the accelerated and decelerated flow zones below the SST become more pronounced for cases with smaller seabed clearances. These influence zones become smaller as the SST moves away from the bottom. The high-pressure zone in the SST bow detaches from the seabed when G/D = 0.5. The low-pressure zone at the beginning of the SST mid-body detaches from the seabed when the gap ratio is 0.7. When G/D is 1.0, the pressure distribution above and below the SST is similar.

Figure 8.15 displays the pressure contours for all gap ratios when the SST hovers in the current. These pressure distributions exhibit similarities to those of the moving SST cases.

Figure 8.16 presents a detailed pressure coefficient distribution along the SST at the upper and lower boundaries. A similar pressure coefficient distribution can be observed for both the moving and hovering SST cases. In both cases, the pressure coefficient at the upper boundary is higher than at the lower boundary when x/L is around ±0.3. This pressure difference creates a downward suction force.

Figure 8.17 compares the spatial pressure distribution between a moving SST and a hovering SST at the lowest inflow velocity cases.

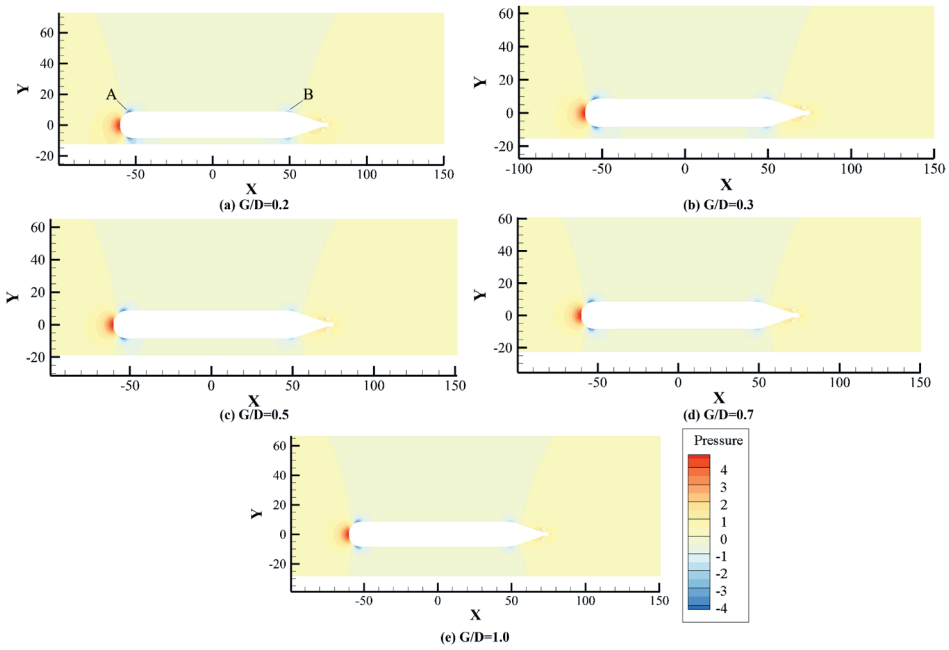

Figure 8.14: Horizontal pressure contours with U_∞=3.09 m/s for different G/D. Units: P [pa], X [m], Y [m]. the SST is moving in the still water. Note: Positive y-axis points upward in this figure.

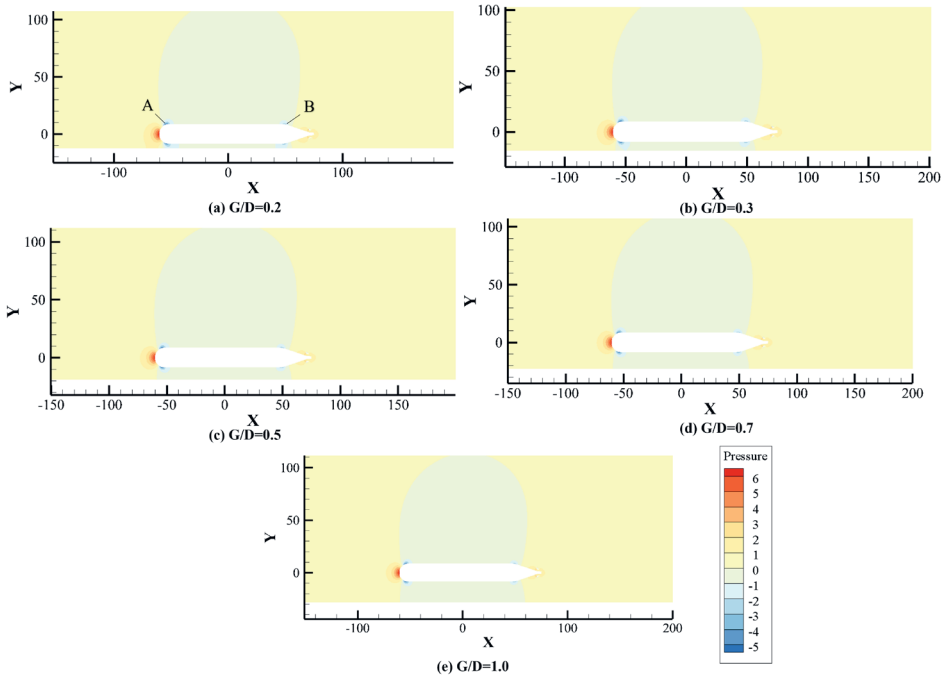

Figure 8.15: Horizontal pressure contours with U_∞=3.54 m/s for different G/D. Units: P [pa], X [m], Y [m]. Case: the SST faces the current and hovers near the seabed. Note: Positive y-axis points upward in this figure.

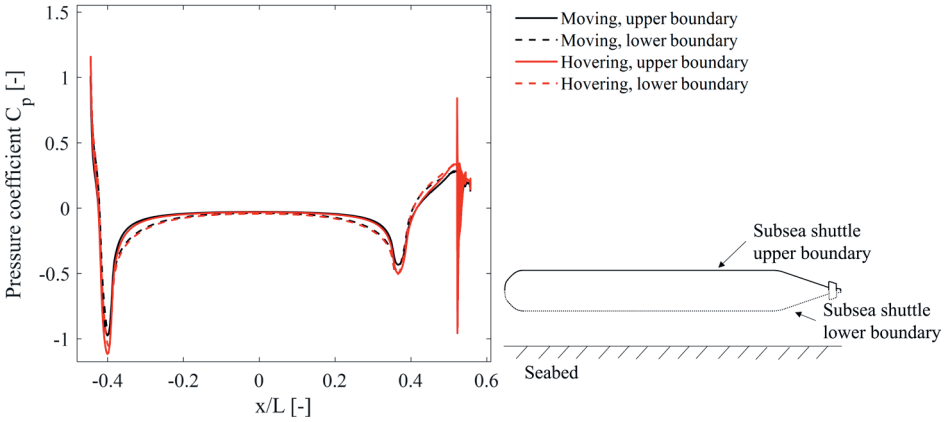

Figure 8.16: Pressure coefficient C_p distribution at the SST upper and lower boundary. U_∞ is 0.51 m/s and 0.58 m/s for moving and SST, respectively. G/D=0.2 for both cases.

The high-pressure zones below the bow (Figure 8.17b) and aft (Figure 8.17c) are larger when the vessel hovers compared to the moving subsea shuttle case, resulting in a lower lift coefficient, as shown in Figure 8.10.

In addition, vorticity contour is studied according to Bolzon et al. [155] and Hansen et al. [156]. This is documented in Ma et al.(2023) [39] as it does not directly explain the changes in the lift force.

8.4 Concluding remarks

This chapter presents a numerical hydrodynamic investigation of a full-scale subsea shuttle system during near-bottom operations at ultra-high Reynolds numbers ranging from 6.75×10^7 to 4.73×10^8. The simulations employ the RANS method in combination with the $k-\omega$ SST model to predict the hydrodynamic behaviour of the SST. A mesh convergence study is conducted to determine an appropriate grid resolution.

Two operating scenarios are considered: one where the SST oper-

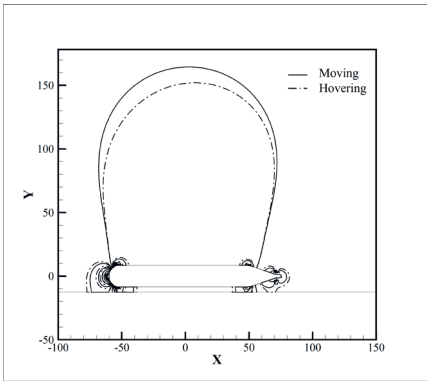

(a) Entire SST

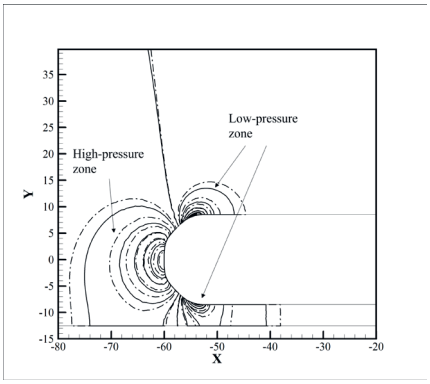

(b) SST bow zoom in

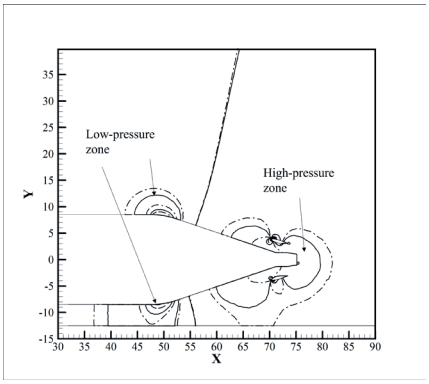

(c) SST aft zoom in

Figure 8.17: Comparison of pressure contour between hovering and moving SST. U_∞ is 0.51 m/s and 0.58m/s for moving and hovering SST, respectively. Note: Positive y-axis points upward in this figure.

ates in still water with a forward speed, achieved by moving the bottom wall boundary at the same speed as the inflow, thus eliminating the boundary layer at the seabed. The other scenario involves the SST hovering near the seabed under the influence of an ocean current boundary layer, which may occur during offloading at a subsea well. 1D simulations generate the fully developed boundary layer profile, which is implemented as the inflow condition for the subsea shuttle simulations.

The main findings of the study are summarised as follows:

- A significant lift force is observed, causing the SST to descend towards the seabed, particularly in simulations with a small bottom gap and high velocity. The lift coefficient increases notably as the G/D decreases and remains independent of changes in the Reynolds number. For the moving bottom case, the lift force surpasses the drag force when the G/D is 0.2 or with an inflow velocity higher than 1.54 m/s and a G/D of 0.3. When the bottom is fixed, the lift coefficient is larger than the drag coefficient for G/D = 0.2, indicating that the SST may require higher thrust in the vertical direction than the main propeller.

- The drag coefficient shows little sensitivity to G/D and slightly decreases with an increase in Re, while the lift coefficient remains nearly constant. The hull viscous drag dominates the total drag over the pressure drag.

- The presence of the seabed boundary layer results in a lower lift coefficient but increases the drag coefficient compared to the moving bottom case. This indicates that the boundary layer significantly affects the hydrodynamic behaviour of the subsea shuttle during near-bottom operations.

Chapter 9

Conclusion

This thesis examined the design and preliminary dynamic analysis of a 164 metre SST concept for liquid CO_2 transportation. This thesis efforts to inform scholars, naval architects, design houses, stakeholders, and regulatory bodies about the design considerations and feasibility of such concepts. In this study, the dynamic analysis part aims to help reduce the designed collapse depth from the operation perspective and further contribute to minimising material cost and further increasing payload capacity. The key results for the baseline design, CO_2 vessel transportation evaluation, hovering analysis, safety operational envelop identification, and near-seabed operation are summarised in Sections 9.1 - 9.5. The limitations of the present study and suggestions for future works are listed in Section 9.6.

9.1 SST Baseline Design

The baseline design of an SST is developed to support the research studies into large commercial autonomous underwater vehicles. It has the potential to become an alternative marine transportation method to existing shuttle tankers and subsea pipelines. The baseline design presents the SST's major specifications and features:

- The purpose of the SST is defined for liquid CO_2 transportation. It

can transport liquid CO_2 from offshore facilities/ports to subsea wells for direct injection.

- The SST is divided into three compartments by two water-tight bulkheads. Thirteen cylindrical cargo tanks are in the flooded mid-body, while the machinery and ballast tanks are arranged in the front and aft free flooding compartments.
- The hydrostatic properties of the SST is checked against DNVGL-RU-NAVAL-Pt4Ch1, Section 3.5.2.3 [70].
- The rule-based structural design is conducted. The SST's main feature is the double hull design with a pressure compensation system which allows the SST to avoid collapse pressure design at the external hull flooded mid-body. This approach helps to reduce the SST's structural weight and contributes to a considerable payload capacity, i.e., 46 % of the total displacement. The SST hull collapse design is performed following DNV guidelines [70, 78]. The internal cargo tank burst design is performed following ASME BPVC rules [80, 81].
- The SST's resistance, powering, and propulsion are studied. The SST is propelled by a three-bladed Wageningen B-series propeller and can use Li-ion battery packs as its energy source. It can achieve a range of 400 km.

The high payload capacity of the SST and slow service speed allow it to maximise its transportation capacity with minimum energy cost.

9.2 Liquid Carbon Dioxide Transportation

CO_2's key properties during transportation and SST operation are discussed. This evaluation discussed CO_2's key properties during

transportation and SST operation, such as thermodynamic properties, purity captured from the source facility, and hydrate formation. CO_2 is stored as a saturated liquid during vessel or vehicle transportation. Normally, it is transported under one of the 3 pressure-temperature combinations; they are Refrigerated state (6 bar, -50 °C), semi-refrigerated state (22 bar, -10 °C), or pressurised state (45 bar, 10 °C). It is found that transporting CO_2 under a pressurised state at room temperature has numerous advantages:

- Transporting liquid carbon dioxide can reduce energy consumption significantly by avoiding liquefication requirements.
- Using carbon steels can reduce the complexity of cargo tank welding and the manufacturing cost.
- The solubility of water in CO_2 increases with temperature. Therefore, the risk of free water and corrosion can be mitigated.
- The risk of hydrate formation is significantly lower when the CO2 temperature is above 8 degrees and therefore reduces the risk of blockage in the piping and pumps.

9.3 Hovering Analysis and Extreme Current Hovering Analysis

9.3.1 SST Manoeuvring Model

After the baseline SST was proposed, and the key design configurations were determined. A dynamic manoeuvring model can be established to further study the feasibility and dynamic response of the SST during different operation scenarios, as most of the submarine manoeuvring software is developed for military submarines. It also needs to be highlighted that civilian submarines will be larger in size and restricted in their manoeuvrability. Therefore, the effect of nonlinearity

in the derivatives-based hydrodynamic models will reduce. Thanks to this, more reliable results can be obtained if the hydrodynamic derivatives are obtained in a correct manner.

As a basis of the SST dynamic analysis, a manoeuvring simulation model that follows semi-empirical formulas is derived [38]. This model enables the consideration of combined load effects from hydrodynamic loads, ocean current, propeller thrust, ballast tank control, thruster control, and control plane actuation. The thruster and ocean current modules are used in the hovering control study [36, 37]. The ballast tank control and control plane modules are applied on SST SOE analysis [38].

9.3.2 Hovering Control Analysis

Based on the proposed SST manoeuvring model, an LQR controller is designed for hovering stability in this work. The following results are concluded during the control system development:

- A planar model is developed based on the baseline design geometry to study the SST's vertical position keeping current using its propeller and two independent tunnel thrusters. A closed-loop control system consists of an LQR controller and a Luenberger observer is designed.
- The SST manoeuvring model is controllable and observable. A control system designed from linearised SST state-space model can successfully control the SST during hovering.
- The selection of linearisation points will not affect the stability of the closed-loop system, a 1 ° smaller inflow angle can lead to better controller gain performance. However, the inflow angle cannot be reduced to 0 ° as the thruster contributions are not captured.
- The Luenberger observer can provide good measurement to SST

states. However, better observation is found on heave motion than on surge and pitch motions.

- Placing the observer poles further to the negative real axis can reduce this error and increase hovering performance.

The SST station-keeping analysis can be performed with the developed manoeuvring model and control system. Such study can help the design and operation of the SST vessel and its relevant facilities.

- Case studies of three four-hour time-domain simulations confirmed that the SST could keep its position using its equipped actuators.
- Sufficient thrust can be provided by tunnel thrusters to cope with 1 m/s designed current speed.
- An envelope of SST trajectory during offloading under three different mean current velocities is outlined.
- The maximum surge and heave motions are 0.25 m and 2.5 m for 1.5 m/s extreme current velocity.

9.3.3 Extreme Current Hovering Analysis

The hovering control model serves as a basis to answer critical questions regarding the design and operation of the SST and the related infrastructures. Further, it can help improve the understanding of manoeuvring and the development of extra-large autonomous subsea vessels. One critical question is how to obtain an efficient structural design for the SST. The existing engineering codes tend to be very conservative by requiring a significant safety factor which will further result in a heavy structural design. Therefore, knowing the maximum response of the SST will benefit the study of such merchant underwater vehicles in two ways: first, knowing the extreme depth excursion

unveils the maximum potential off-site SST during offloading. This reduces the level of uncertainty and denotes a less conservative design by knocking down the safety factor of the structural design. In addition, the extreme depth excursion can also provide a basis for the decision-makers regarding SST operation. This study clarifies the maximum and minimum off-sites of the SST from its desired offloading reference point. During offloading, it determines the required minimum safety distance from subsea installations and floating structures. The extreme response of the SST hovering during offloading. The following findings are concluded in the extreme current hovering analysis:

- The mean current velocity is set to be 1.6 m/s, corresponding to observation data in the North Sea with a return period of 50 years.
- Twenty 4-hour simulations are performed to get the SST response. The extreme responses with the exceedance rate of 1×10^{-6} from 5 measurement points located at the SST centroid, upper-aft, upper-bow, lower-aft, and lower-bow are studied using the ACER method.
- Effect of k value from 1 to 6 is studied, and the result shows that $k\geq 2$ can provide a very accurate prediction of the SST extreme response during hovering.
- The extreme depth excursion happens at the SST aft during hovering, and the maximum depth excursion is 86 m. This means the 19 bar (corresponds to 190 m water depth) collapse pressure can be significantly reduced.
- From an operational perspective, a minimum 16 m safety distance is suggested for the SST hovering. The SST should avoid any subsea or floating structures with a minimum 16 m distance to avoid a potential collision.
- When the SST is offloading at a 40 m safety depth, the maximum draught of the floating structures in the vicinity should be less

than 23 m.

9.4 Safety Operational Envelope

The SST's evacuation ability during critical malfunctions is studied. The SOE is a crucial topic in the SST design process as it demonstrates the recoverability of the SST under critical malfunctions, including partial flooding, jam-to-rise, and jam-to-dive. Even though SOE has been established for military submarines for over 50 years, public literature on such analyses is still not readily available. In addition, as very few submarines have been designed for civilian use, this work will also help close this knowledge gap and further assist the development and safety operation of large novel subsea vessels.

The SOE helps to improve the currently existing design and operation of the SST in the following aspects:

- A 40 m safety depth is sufficient to allow the SST to avoid broaching the surface when aft control plane jams when travelling at 3 m/s design speed. If a higher sailing speed is required, the SST has to travel at deeper water depths.
- The SST can survive through all considered malfunctions when travelling at a 70 m nominal water depth.
- The SST should hover above 80 m water depth during offloading to recover from partial flooding.
- The maximum pitch angle of the SST is set to be $\pm$ 15 °. Within this limit, the SST is recoverable if aft control plane jam occurs.
- The 70 m nominal diving depth proposed by the DNV naval submarine code is conservative. The SOE allows the existing SST design to travel a maximum 100 m diving depth in accordance with a 190 m collapse diving depth. This depth can fulfil operation safety as the SST can survive crucial malfunctions.

- The safety factor between nominal and collapse diving depths can be reduced. This can reduce SST structural weight and avoid heavy and complex steel construction.

9.5 CFD Analysis of SST Near-Bottom Operation

The first dynamic manoeuvring model was developed following semi-empirical formulas. For a higher level of accuracy, the numerical hydrodynamic study of the real-size SST during near-bottom operations is conducted. Ultra-high Reynolds numbers between 6.75×10^7 and 4.73×10^8 are considered. RANS simulations combined with the $k-\omega$ SST model are used to predict the hydrodynamic properties of the SST. A mesh convergence study is conducted to determine an appropriate grid resolution. The applied mesh and method in this thesis are validated against the published experimental data and numerical results of the SUBOFF submarine and documented in [39]. Two types of operating scenarios are considered. The first case considers the SST operating in still water with forward speed. The second case considers an SST hovering near the seabed subjected to an ocean current boundary layer. The effects of velocity, gap ratio, and boundary layer are investigated. The main conclusions are summarised below:

- A significant lift force forcing the SST to be decent towards the seabed can be noticed for simulations with a small bottom gap and high velocity. The lift coefficient grows significantly when the gap ratio reduces and is independent of the change in the Reynolds number. For the moving bottom case, the lift force overpasses the drag force when the gap ratio is 0.2 or with an inflow velocity higher than 1.54 m/s and a gap ratio of 0.3. When the bottom is fixed, the lift coefficient is larger than the drag coefficient for G/D = 0.2. As a result, it indicates the subsea shuttle

may require higher thrust in the vertical direction than the main propeller.

- The drag coefficient is not sensitive to the bottom gap ratio. It slightly decreases with the increase of Reynolds number while the lift coefficient remains the same. The hull viscous drag dominates the total drag over the pressure drag.
- The seabed boundary layer results in a lower lift coefficient but increases the drag coefficient compared with the moving bottom case.

9.6 Limitations and Suggestions for Future Work

Several limitations are apparent in the design, manoeuvring modelling, and dynamic analysis of this study. These constraints offer opportunities for further exploration, serving as a natural extension of the current research on SST design and dynamic analysis. This section aims to illuminate these limitations and provide suggestions for future investigation.

The conceptual design phase of this study focuses solely on one potential baseline SST. This SST blueprint stems from the collaborative efforts of Xing and Equinor ASA, as documented in prior works [19, 33, 34, 96, 130]. However, this study does not encompass the potential range of SST sizes, omitting considerations for smaller (50 m length) or larger (over 200 m length) variations. Nonetheless, a brief discussion on these dimensions is included in a techno-economic study at UiS [157].

Additionally, the baseline SST blueprint outlined in this thesis adopts a traditional rule-based design methodology. This approach incorporates safety factors stipulated by the DNVGL-RU-NAVAL-Pt4Ch1 guidelines, which dictate augmented structural safety factors

with decreasing water depth. Consequently, it is evident that safety factors become excessively high when the SST is intended for operation in shallower waters. There exists the potential to harness advanced engineering tools like Finite Element Analysis (FEA) to enhance structural design and achieve optimal solutions. By subjecting the SST's structure to a diverse array of design scenarios through FEA, potential issues such as overdesign, underdesign, or stress concentration can be identified.

The baseline design omits consideration for automation control, communication, and navigation systems. A systematic evaluation is warranted to pinpoint risks and potential hazards inherent in SST operations or the broader utilisation of extra-large autonomous underwater vehicle operations.

The discourse on CO_2 transportation properties is an initial assessment grounded in the existing literature. Notably, gaps in knowledge persist, warranting more comprehensive research to investigate the effects of saturated CO_2 liquid with varying purity levels across diverse pressure and temperature conditions for SST operations.

Although this study develops a planar manoeuvring model for the SST, its potential is further underscored by its capability to evolve into a comprehensive 6 DoFs model facilitated by the symmetry of the geometry. The hovering control model can be broadened to encompass scenarios such as functionality failures, extreme loading conditions, and the impact of offloading disturbances, shifts in the CoG, and flowline snap-loadings.

Lastly, the semi-empirical nature of the hovering and SOE studies could benefit from enhanced reliability achieved through numerical simulations incorporating greater nonlinearity in hydrodynamic derivatives.

Appendix A

Baseline SST Nominal Diving Depth Determination

The 70 m nominal diving depth is determined based on a preliminary estimation of the minimum recoverable depth from a worst jam-to-rise situation. In this situation, a malfunction in the hydroplane control system is assumed to occur when the SST is sailing at 9.2 knots maximum speed v_{max} (including 2 knots considering current) speed with a 5 ° initial pitch angle. After a 5 s reaction time, the SST control system realises the situation and takes restoring reaction. It pumps aft trim tank ballast to the front to decrease the pitch angle. This reduces the ascent speed. The SST can be recovered if the pitch angle is reduced to 0 ° before reaching the 40 m safety depth. The following parameters are used in the calculations:

- Maximum pitch angle: The maximum pitch angle of the SST is defined to be 5 °. The SST does not require excellent manoeuvrability since it travels constantly at a fixed water depth.

- Maximum sailing speed: The maximum sailing speed is 7.2 knots. This is 20 % higher than the SST's design speed. Current: The designed current speed is set to be 1 m/s (2 knots) at the same

speed range with the highest observed current speed of the North Atlantic Current and Norwegian Coastal Current.

- Trim tank pump capacity: The maximum trim tank pump capacity is 2,000 m^3/h. This can be achieved by two 1,000 m^3/h pumps, e.g., Wärtsilä AQ-1200-EC [158].
- Moment of inertia: The moment of inertia I_{yy} is estimated to be 7.9×10^7 t/m^2 as a solid cylinder using:

$$I_{yy} = \frac{1}{4} W \frac{D^2}{2} + \frac{1}{12} W L^2 \tag{A.1}$$

  where W is the SST weight, D is the SST beam, and L is the SST length.
- BG: The distance of the CoB and CoG is estimated to be 0.6 m.
- Reaction time: The reaction time is estimated to be 5 s. Since the SST is autonomous, it has a faster response than a normal submarine, whose reaction time is around 15 s [129]. This is the period before the SST takes recovering reactions after the jam-to-rise happened.

With the above assumptions, the total pitch moment acting on the SST can be calculated as follows:

$$M_{tot} = \underbrace{-L_{trim} \cdot w_{tw}}_{\text{Trim tank restoring moment}} + \underbrace{W \cdot BG \cdot \sin \alpha_{max}}_{\text{Jammed aft plane}} - \underbrace{\frac{W \cdot BG \cdot \sin \alpha}{2}}_{\text{Contribution from the SST COG}} \tag{A.2}$$

where L_trim is the longitudinal distance between two trim tanks, w_{tw} is the weight of trim ballast pumped from the aft trim tank to the fwd trim tank, α_{max} is the 5 ° maximum pitch angle.

The pitch angular velocity γ_r is therefore calculated as:

$$\gamma_r = \frac{M_{tot}}{I_{yy}} \tag{A.3}$$

As a result, the recovery time is 60 s, and together with the 5 s reaction time, the total ascent time t_{as} is 65 s. The ascent distance is calculated as follows:

$$d_{as} = v_{max} \cdot \sin \alpha_{max} \cdot t_{as} \tag{A.4}$$

The total ascent distance is calculated to be 26 m. As a result, the lowest recoverable depth in a jam-to-rise situation is 66 m. Based on this, the nominal diving depth is set as 70 m.

Appendix B

Baseline SST Resistance Forces Estimation

This section presents the calculation of resistance forces as a function of the slenderness ratio. When the SST travels forward, its resistance can be separated into two components: skin friction and body drag. Skin friction is caused by resistance forces acting on the body's surface. This means that it highly depends on the hull roughness and wetted surface area. The body drag is caused by the pressure difference between the bow and aft of the body, which is more dependent on the body shape. The skin friction for a slender structure usually is higher than the body drag because of the high wetted surface area/volume ratio. The resistance components are calculated as follows: The skin friction C_{sf} is derived from the Reynolds number Re in accordance with the ITTC-57 correlation line [82]:

$$C_{sf} = \frac{0.075}{(\log Re - 2)^2} \tag{B.1}$$

A form factor k is introduced to calculate pressure drag C_v contribution using:

$$C_v = (1 + k)\, C_{sf} \tag{B.2}$$

where k is calculated using the formula:

$$k = 1.5\left(\frac{D}{L}\right)^{\frac{3}{2}} + 7\left(\frac{D}{L}\right)^{3} \tag{B.3}$$

The results are shown in Figure 3.6. The volume is fixed at 32,799 m^3 while the slenderness ratio varies. This method provides a rough but quick estimation of the vessel's slenderness in the early stages of the design process. CFD analysis and scale model tests are usually performed if more accurate results are required.

Appendix C

Baseline SST External Hull Design Calculations

The design calculation method in DNVGL-RU-NAVAL-Pt4Ch1, Appendix A, Section 6 [70] is applied to determine the SST's external hull properties. The calculation input and process are given in Table C.1. The symbols presented in the table are aligned with the notation used in the guideline. The corresponding equation numbers used in the guideline are also mentioned here. The stresses in the free flooding compartments and flooded mid-body external hulls are listed in Table C.2, Table C.3, Table C.4 and Table C.5. The external hulls in free flooding compartments are the pressure hull subjected to hydrostatic pressures. Thus, they are checked against permissible stress at nominal diving depth, test diving depth, and collapse depth in accordance with Chapter 4 in DNVGL-RU-NAVAL-Pt4Ch1 [70]. The permissible values are listed in Table C.6. Although the flooded mid-body external hull does not handle hydrostatic pressure, it is designed for 7 bar (70 m) collapse pressure to avoid immediate structural failure in accidental load cases like the malfunction of the mid-body seawater vent.

A finite element analysis is performed to justify the watertight bulkhead design. Table C.7 lists the numerical analysis results and the permissible stresses in DNVGL-RU-NAVAL-Pt4Ch1 Sec.4.3 [70]. Figure C.1 presents the bulkhead equivalent stress distribution under

19 bar collapse depth pressure, the applied force, and the boundary condition. Static pressure is applied normally to the ellipsoidal bulkhead from the flooded mid-body. The external hull is clamped at the far end of the mid-body.

Table C.1: SST external hull design spreadsheet

Parameter	Free flooding compartment			Flooded compartment	Eq. number in DNVGL RU P4C1 Appendix A
Design pressure type	Nominal diving depth	Test diving depth	Collapse depth	Collapse	
Design pressure	7 bar	10.5 bar	19 bar	7 bar	User input
Hull thickness	0.041 m			0.025 m	User input
Hull radius	8.500 m				User input
Frame web height	0.300 m				User input
Frame web thickness	0.030 m				User input
Flange width	0.100 m				User input
Flange thickness	0.033 m				User input
Frame spacing	1.000 m			1.500 m	User input
Frame cross-sectional area	0.012 m^2				User input
Inner radius to the flange of frame	8.15 m				User input
Youngs modulus	206 GPa				User input
Poisson Ratio	0.3				User input
Poisson ratio in elastic-plastic range	0.300	0.300	0.309	0.300	(A48)
Frame distance without thickness	0.97 m			1.47 m	(A9)
Effective length	0.91 m			0.72 m	(A10)
Effective area	0.013 m2				(A11)
The radial displacement in the middle between the frames	-0.0035 m	-0.0053 m	-0.0093 m	-0.0087 m	(A15)
The radial displacement at the frames	-0.0019 m	-0.0027 m	-0.0057 m	-0.0094 m	(A16)
The reference stress is the circumferential stress in the unstiffened cylindrical pressure hull	145 MPa	218 MPa	394 MPa	238 MPa	(A13)
The equivalent stresses are composed of the single stresses in longitudinal and circumferential direction at the middle between frames	95 MPa	142 MPa	252 MPa	214 MPa	(A14)
The equivalent stresses are composed of the single stresses in longitudinal and circumferential direction at the frames	70 MPa	104 MPa	197 MPa	236 MPa	(A14)
Average membrane stress in longitudinal direction	73 MPa	109 MPa	197 MPa	119 MPa	(A17)
Membrane stress in circumferential direction in the middle between the frames	108 MPa	160 MPa	284 MPa	247 MPa	(A18)
Membrane stress in circumferential direction at the frames	67 MPa	98 MPa	197 MPa	272 MPa	(A19)
Bending stresses in longitudinal direction in the middle between the frames	28 MPa	45 MPa	93 Mpa	126 MPa	(A20)
Bending stresses in longitudinal direction at the frames	95 MPa	149 MPa	255 MPa	69 MPa	(A21)
Bending stresses in circumferential direction in the middle between the frames	8 MPa	13 MPa	28 MPa	38 MPa	(A22)
Bending stresses in circumferential direction at the frames	29 MPa	45 MPa	76 MPa	21 MPa	(A23)
Tangential module	206 GPa	206 GPa	206 GPa	206 GPa	(A38)
Secant module	206 GPa	206 GPa	199 GPa	206 GPa	(A39)
Elastic buckling pressure	58.3 bar			39.9 bar	(A21)
Theoretical elastic-plastic buckling pressure	57.0 bar			39.9 bar	(A22)
Reduction factor	0.75				(A23)
Elastic-plastic buckling pressure	42.9 bar			39.9 bar	(A23)·(A23)

Table C.2: Stresses in the free flooding compartment (nominal diving depth).

Types of stresses	At the frame			In the middle of the field		
	Circumferential	Equivalent	Axial	Circumferential	Equivalent	Axial
Membrane stress [MPa]	67	-	73	108	-	73
Membrane equivalent stress [MPa]	-	95	-	-	70	-
Bending stresses [MPa]	29	-	95	8	-	28
Normal stress outside [MPa]	96	-	168	116	-	101
Equivalent normal stress outside [MPa]	-	146	-	-	109	-
Normal stress inside [MPa]	96	-	168	116	-	101
Equivalent normal stress inside [MPa]	-	146	-	-	109	-

Table C.3: Stresses in the free flooding compartment (test diving depth).

Types of stresses	At the frame			In the middle of the field		
	Circumferential	Equivalent	Axial	Circumferential	Equivalent	Axial
Membrane stress [MPa]	98	-	109	160	-	109
Membrane equivalent stress [MPa]	-	142	-	-	104	-
Bending stresses [MPa]	45	-	149	13	-	45
Normal stress outside [MPa]	142	-	257	174	-	153
Equivalent normal stress outside [MPa]	-	223	-	-	164	-
Normal stress inside [MPa]	142	-	257	174	-	153
Equivalent normal stress inside [MPa]	-	223	-	-	164	-

Table C.4: Stresses in the free flooding compartment (collapse depth).

Types of stresses	At the frame			In the middle of the field		
	Circumferential	Equivalent	Axial	Circumferential	Equivalent	Axial
Membrane stress [MPa]	197	-	197	284	-	197
Membrane equivalent stress [MPa]	-	252	-	-	197	-
Bending stresses [MPa]	76	-	255	28	-	93
Normal stress outside [MPa]	273	-	452	312	-	290
Equivalent normal stress outside [MPa]	-	394	-	-	302	-
Normal stress inside [MPa]	273	-	452	312	-	290
Equivalent normal stress inside [MPa]	-	394	-	-	302	-

Table C.5: Stresses in the flooded compartment.

Types of stresses	At the frame			In the middle of the field		
	Circumferential	Equivalent	Axial	Circumferential	Equivalent	Axial
Membrane stress [MPa]	272	-	119	247	-	119
Membrane equivalent stress [MPa]	-	214	-	-	236	-
Bending stresses [MPa]	21	-	69	38	-	126
Normal stress outside [MPa]	293	-	188	285	-	245
Equivalent normal stress outside [MPa]	-	257	-	-	267	-
Normal stress inside [MPa]	293		188	285	-	245
Equivalent normal stress inside [MPa]	-	257	-	-	267	-

Table C.6: External hull permissible stresses (Ref. Sec.4.3 in [70]).

Location (depth)	VL D47 tensile strength	VL D47 yield strength	Permissible stress calculation	Permissible stress value	Results
Free flooding compartment (nominal diving depth)	550 MPa	460 MPa	$min\left\{\frac{550\ MPa}{2.7}, \frac{460\ MPa}{1.7}\right\}$	203 MPa	Tab. C.2
Free flooding compartment (test diving depth)			$\frac{460\ MPa}{1.1}$	418 MPa	Tab. C.3
Free flooding compartment (collapse depth)			$\frac{460\ MPa}{1.0}$	460 MPa	Tab. C.4
Flooded compartment (collapse depth)			$\frac{460\ MPa}{1.0}$	460 MPa	Tab. C.5

Table C.7: Watertight bulkhead equivalent stresses and permissible stresses.

Case	Depth	Maximum equivalent stress	Permissible stress (Ref. Sec.4.3 in DNVGL-RU-P4C1)	Criterion fulfilled?
Nominal diving depth	70 m	153 MPa	203 MPa	Yes
Test diving depth	105 m	229 MPa	418 MPa	Yes
Collapse depth	190 m	415 MPa	460 MPa	Yes

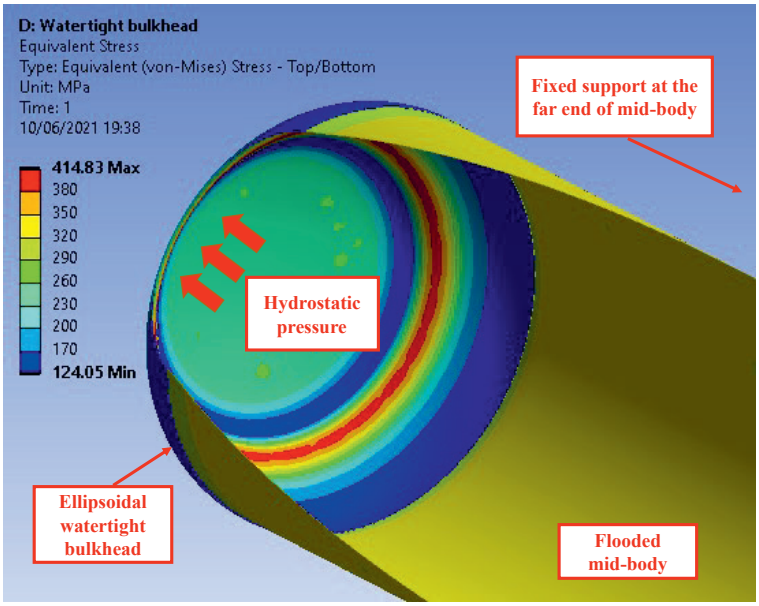

Figure C.1: SST bulkhead finite element analysis results at 190 m collapse depth.

Appendix D

Baseline SST Internal Tank Design Calculations

The internal tanks within the SST adhere to the guidelines outlined in Chapter 4 of ASME BPVC Section VIII, Division 2 [80]. Within the SST structure, specific tanks, including the main cargo tanks, auxiliary cargo tanks, compensation tanks, and trim tanks, are engineered to withstand burst pressure. Additionally, the buoyancy tubes are designed with consideration for collapse pressure.

Tanks Under Internal Pressure

Determining hull thicknesses for cylindrical shells and hemisphere heads for tanks subjected to internal pressure is based on the provisions detailed in Chapter 4.3.3 and Chapter 4.3.5 of ASME VIII-2 [80], respectively. The minimum requisite thickness for a cylindrical hull exposed to internal pressure is articulated as follows:

$$t_{shell} = \frac{D_t}{2}\left(e^{\frac{p_i}{S_a E_w}} - 1\right) \tag{D.1}$$

where t_{shell} is the hull thickness, D_t is the tank diameter, and S_a is the allowable stress of the material. E_w is the weld joint efficiency, this is set to be 1.0 for circumferential joints and longitudinal joints on a

shell (Ref. Table 7.2 in ASME VIII-2 [80]). p_i is the design pressure. It is defined to be 55 bar for the cargo tanks and hydrostatic pressure for the trim and composition tanks.

Similarly, the required minimum thickness of a hemisphere head under burst (internal) pressure is expressed as:

$$t_{shell} = \frac{D_t}{2}\left(e^{\frac{0.5 \cdot p_i}{S_a E_w}} - 1\right) \tag{D.2}$$

Tanks Under External Pressure

Chapter 4.4.5 in ASME VIII-2 [80] introduces the pressure design of pressure vessels under external pressure. It is used to determine the buoyancy tank properties. The step-by-step calculation process can be found in Table D.1.

Table D.1: Buoyancy tube calculation.

Parameter	**Symbol in ASME BPVC Sec. VIII Div.2**	**Value**	**Eq. number in ASME BPVC Sec. VIII Div.2**
Thickness	t	0.015 m	User input
Outer diameter	D_o	1.28 m	User input
Unsupported length	L	4 m	User input
Young's modulus	E_y	200 GPa	User input
Minimum yield strength	S_y	414 MPa	User input
Design factor	FS	2.4	(4.4.1)
Predicted elastic buckling stress	F_{he}	84 MPa	(4.4.19)
Factor	M_x	41	(4.4.20)
Factor	C_h	0.02	(4.4.22)
Predicted buckling stress	F_{ic}	84 MPa	(4.4.27)
Allowable external pressure	P_a	8 bar	(4.4.28)

Appendix E

Baseline SST Propeller Design Calculations

Propeller K_T, K_Q and $_O$

The wake fraction, w_T, is obtained from Figure 6.7 in Burcher el al. (1994) [15] (reproduced in Figure E.1) given the tailcone angle, α_c and propeller/hull ratio, P/H.

Inflow velocity advance of the propeller V_A is calculated as:

$$V_A = (1 - w_T)\, V_s \tag{E.1}$$

The advance number, J is then calculated as:

$$J = \frac{V_A}{nD_p} \tag{E.2}$$

Based on the advance number J, the thrust and torque coefficients K_T and K_Q and efficiency, η_O, can be found using the propeller curves from [83].

Propeller QPC

The thrust deduction, t can be obtained from Fig. 6.8 in Burcher el al. (1994) [15] (reproduced in Figure E.2) given the tailcone angle, αc and propeller/hull ratio, P/H. The hull efficiency, η_H, represents the ratio between effective power and thrust power and is calculated as:

$$eta_H = \frac{1-t}{1-w_T} \tag{E.3}$$

A relative rotative efficiency η_R of 1.05 is used based on the recommendation in Chapter 5.1.5 of Renilson (2015) [84] for similarly sized submarine hulls and propellers. Finally, the quasi-propulsive coefficient (QPC) is calculated as follows:

$$QPC = \eta_o \cdot \eta_H \cdot \eta_R \tag{E.4}$$

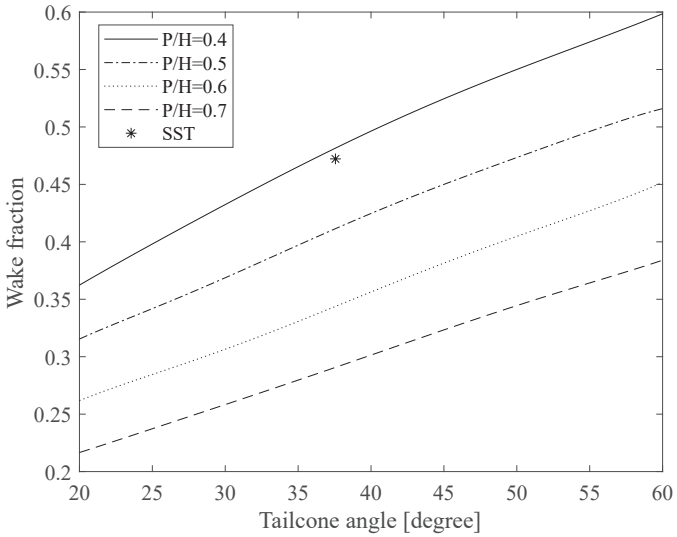

Figure E.1: Effects of tailcone angle on wake fraction reproduced from Burcher et al. (1994) [15].

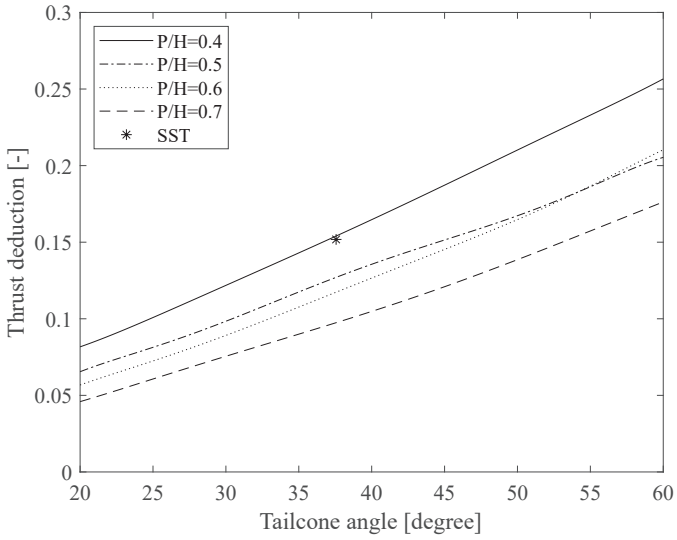

Figure E.2: Effects of tailcone angle on thrust deduction reproduced from Burcher et al. (1994) [15].

References

[1] R Fullenbaum, J Fallon, and B Flanagan. *Oil & Natural Gas Transportation & Storage Infrastructure: Status, Trends, & Economic Benefits*. IHS Global Inc, Washington, USA, 2013.

[2] Andrew C Palmer and Roger A King. *Subsea pipeline engineering*. PennWell Corp., Tulsa, Oklahoma, USA, 2 edition, 2008.

[3] Julie Wilson. Shuttle tankers vs pipelines in the gom frontier. *World oil*, 229(4):149–151, 2008.

[4] Catrine Vestereng. Shuttle tankers brazil - tanker insights - dnv, 2019. URL `https://www.dnv.com/expert-story/maritime-impact/shuttle-tankers-Brazil.html`.

[5] Norwegian Petroleum Directorate (NPD). Carbon capture and stroage, 2023. URL `https://www.norskpetroleum.no/en/environment-and-technology/carbon-capture-and-storage/`.

[6] Equinor ASA. Northern lights ccs, 2023. URL `https://www.equinor.com/en/what-we-do/northern-lights.html`.

[7] Apostolos Papanikolaou. *Ship Design: Methodologies of Preliminary Design*. Springer, Dordrecht Heidelberg New York London, 2014.

[8] UNFCCC. Adoption of the paris agreement. united nations framework convention on climate change, 2015.

[9] Ottmar Edenhofer, Ramón Pichs-Madruga, Youba Sokona, Kristin Seyboth, Susanne Kadner, Timm Zwickel, Patrick Eickemeier, Gerrit Hansen, Steffen Schlömer, Christoph von Stechow, et al. *Renewable energy sources and climate change mitigation: Special report of the intergovernmental panel on climate change*. Cambridge University Press, New York, USA, 2011.

[10] Jeff Tollefson. Covid curbed 2020 carbon emissions-but not by much. *Nature*, 589(343), 2021. DOI:10.1038/d41586-021-00090-3.

[11] Northern Lights. Annual report northern lights 2022. Annual report, Northern Lights JV DA, 2023.

[12] International Energy Agency (IEA). Energy technology perspectives 2010 - part of energy technology perspectives. Report, International Energy Agency, 2010. URL https://www.iea.org/reports/energy-technology-perspectives-2010.

[13] Paul S. Granville. Elements of the drag of underwater bodies. Technical Report SPD-672-01, David W. Taylor Naval Ship Research and Development Centre, 1976. URL https://apps.dtic.mil/sti/citations/ADA031995.

[14] N. Friedman. *Submarine Design and Development*. Naval Institute Press, Annapolis, USA, 1983.

[15] Roy Burcher and Louis Rydill. *Concepts in Submarine Design*. Cambridge University Press, Cambridge, UK, 1994.

[16] D.A. Jones, D.B. Clarke, I.B. Brayshaw, J.L. Barillon, and B. Anderson. The calculation of hydrodynamic coefficients for underwater vehicles. Technical Report DSTO-TR-1329, Defence Science and Technology Organisation, Australia, 2002.

[17] P.N. Joubert. Some aspects of submarine design part 1. hydrodynamics. Technical Report DSTO-TR-1622, Defence Science and Technology Organisation, Australia, 2004.

[18] P.N. Joubert. Some aspects of submarine design part 2. shape of a submarine. Technical Report DSTO-TR-1920, Defence Science and Technology Organisation, Australia, 2006.

[19] Yihan Xing, Muk Chen Ong, Tor Hemmingsen, Kjell Einar Ellingsen, and Lorents Reinås. Design considerations of a subsea shuttle tanker system for liquid carbon dioxide transportation. *Journal of Offshore Mechanics and Arctic Engineering*, 143(4), 2021. ISSN 0892-7219. DOI:10.1115/1.4048926. URL https://doi.org/10.1115/1.4048926.

[20] Boeing. 747-400/-400er freighter, 2010. URL https://www.boeing.com/resources/boeingdotcom/company/about_bca/startup/pdf/freighters/747-400f.pdf.

[21] American Bureau of Shipping (ABS). Scaling the tanker market. *Surveyor*, Winter:5–9, 2002. URL https://web.archive.org/web/20070930043604/http://www.eagle.org/NEWS/pubs/pdfs/SurveyorWinter02.pdf.

[22] Carl TF Ross. *Pressure vessels: external pressure technology*. Woodhead Publishing, Philadelphia, USA, 2 edition, 2011.

[23] Yucong Ma, Yihan Xing, Muk Chen Ong, and Tor Henning Hemmingsen. Baseline design of a subsea shuttle tanker system for liquid carbon dioxide transportation. *Ocean Engineering*, 240: 109891, 2021. DOI:10.1016/j.oceaneng.2021.109891.

[24] Filipe Dutra da Silva, Thiago Pontin Tancredi, and Ernane Silva. Corrections for the drag on submarines due to the blockage effect. *Ocean Engineering*, 275:114150, 2023. DOI:10.1016/j.oceaneng.2023.114150.

[25] Michael Mackay. Estimation of submarine near-bottom hydrodynamic loads and squat. Technical report, 2003.

[26] Tahsin Tezdogan, Atilla Incecik, and Osman Turan. A numerical investigation of the squat and resistance of ships advancing through a canal using cfd. *Journal of marine science and technology*, 21:86–101, 2016. DOI:10.1007/s00773-015-0334-1.

[27] Lawrence R Jacobsen. Subsea transport of arctic oil-a technical and economic evaluation. In *Offshore Technology Conference*, pages OTC–1425, Houston, Texas, 1971. DOI:10.4043/1425-MS.

[28] PK Taylor and JB Montgomery. Arctic submarine tanker system. In *Offshore Technology Conference*, pages OTC–2998, Houston, Texas, 1977. DOI:10.4043/2998-MS.

[29] P Moloney. Submarine tanker concepts and problems. Report NMRC-KP-129, National Maritime Research Center, 1974.

[30] L Jacobsen, K Lawrence, K Hall, P Canning, and E Gardner. Transportation of lng from the arctic by commercial submarine. *Marine Technology and SNAME News*, 20(04):377–384, 1983. DOI:10.5957/mt1.1983.20.4.377.

[31] Hendrik Brandt, Christian Frühling, Achim Hollung, Marc Schiemann, and Thomas Voß. A multi-purpose submarine concept for arctic offshore operations. In *OTC Arctic Technology Conference*, pages OTC–25501, Copenhagen, Denmark, 2015. DOI:10.5957/mt1.1983.20.4.377.

[32] Usman Nawaz Ahmad, Yihan Xing, and Yucong Ma. Uis subsea-freight glider: A large buoyancy-driven autonomous cargo glider. *Journal of Offshore Mechanics and Arctic Engineering*, 145(4):045001, 01 2023. DOI:10.1115/1.4056419.

[33] Equinor Energy AS. RD 662093-Subsea shuttle system. *Research Disclosure*, 2019.

[34] Kjell Einar Ellingsen, Ola Ravndal, Lorents Reinås, Jan Henry Hansen, Francesco Marra, Erling Myhre, Pablo Matias Dupuy, and Knut Sveberg. Rd 677082-subsea shuttle system. *Research Disclosure*, 2020.

[35] Yucong Ma, Yihan Xing, and Tor Henning Hemmingsen. An evaluation of key challenges of co2 transportation with a novel subsea shuttle tanker. In *COTech & OGTech 2021*, page 012078, Stavanger, Norway, 2021. IOP Publishing. DOI:10.1088/1757-899X/1201/1/012078.

[36] Yucong Ma, Yihan Xing, and Dan Sui. Trajectory envelope of a subsea shuttle tanker hovering in stochastic ocean current—model development and tuning. *Journal of Offshore Mechanics and Arctic Engineering*, 145(3):030901, 2023. DOI:10.1115/1.4055282.

[37] Yucong Ma, Terje Andreas Jevnaker, and Yihan Xing. Station keeping of a subsea shuttle tanker system under extreme current during offloading. *Ships and Offshore Structures*, pages 1–13, 2023. DOI:10.1080/17445302.2023.2211244.

[38] Yucong Ma and Yihan Xing. Identification of the safety operating envelope of a novel subsea shuttle tanker. *Ocean Engineering*, 266:112750, 2022. DOI:10.1016/j.oceaneng.2022.112750.

[39] Yucong Ma, Guang Yin, Marek Janocha, Yihan Xing, and Muk Chen Ong. Numerical investigation on near-bottom operation of an extra-large freight submarine. *Journal of Offshore Mechanics and Arctic Engineering*, pages 1–24, 2023. DOI:10.1115/1.4063022.

[40] MathWorks. *Simulink User's Guide*. The MathWorks, Inc., MA, USA, 2022.

[41] Yucong Ma, Dan Sui, Yihan Xing, Muk Chen Ong, and Tor Henning Hemmingsen. Depth control modelling and analysis of a subsea shuttle tanker. In *International Conference on Offshore Mechanics and Arctic Engineering*, volume 85154, page V005T05A026. American Society of Mechanical Engineers, 2021.

[42] Yucong Ma, Yihan Xing, Dan Sui, Muk Chen Ong, and Tor Henning Hemmingsen. Two-dimensional planar modeling of the depth control of a subsea shuttle tanker. *Journal of Offshore Mechanics and Arctic Engineering*, 145(4):044501, 2023. DOI: 10.1115/1.4056418.

[43] Yucong Ma, Yihan Xing, Marina Simplicio Da Silva, and Dan Sui. Modelling of a subsea shuttle tanker hovering in ocean currents. In *International Conference on Offshore Mechanics and Arctic Engineering*, volume 85901, page V05BT06A039. American Society of Mechanical Engineers, 2022.

[44] Terje Andreas Jevnaker. Station keeping of a subsea shuttle tanker system under extreme current during offloading. Master's thesis, uis, 2022.

[45] Andrew Ross, Thor I Fossen, and Tor Arne Johansen. Identification of underwater vehicle hydrodynamic coefficients using free decay tests. *IFAC Proceedings Volumes*, 37(10):363–368, 2004. DOI:10.1016/S1474-6670(17)31759-7.

[46] SJ Tinker. Identification of submarine dynamics from free model tests. In *Admiralty Marine Technology Establishment, UK, Proceedings of the DRG Seminar on Advanced Hydrodynamic Testing Facilities, Session 3, Paper 16, The Netherlands. Paper: P1982-1 Proceedings.*, 1982.

[47] Thor I Fossen. *Handbook of marine craft hydrodynamics and motion control*. John Wiley & Sons, West Sussex, UK, 2011.

[48] Timothy Timothy Jason Prestero. Verification of a six-degree of freedom simulation model for the remus autonomous underwater vehicle. Master's thesis, Massachusetts institute of technology, 2001.

[49] R.D. Blevins. *Formulas for Natural Frequency and Mode Shape*. Van Nostrand Reinhold Co., New York, 1979.

[50] Odd Faltinsen. *Sea loads on ships and offshore structures*, volume 1. Cambridge university press, Cambridge, UK, 1993.

[51] S.F. Hoerner. *Fluid-dynamic drag: Practical Information on aerodynamic drag and hydrodynamic resistance*. Published by the author, California, USA, 1965.

[52] Brian DO Anderson and John B Moore. *Optimal control: linear quadratic methods*. Courier Corporation, New York, USA, 2007.

[53] Carlos Hugo Mendes, Cristiano Bentes, Tiago Alexandre Rebelo, and K Bousson. Guidance and robust control of a double-hull autonomous underwater vehicle. *Proceedings of ICEUBI-2017*, 1:1194–1203, 2017.

[54] Brij Kishor Tiwari and Rajiv Sharma. Design and analysis of a variable buoyancy system for efficient hovering control of underwater vehicles with state feedback controller. *Journal of Marine Science and Engineering*, 8(4):263, 2020. DOI:10.3390/jmse8040263.

[55] Michael Athans and Peter L Falb. *Optimal control: an introduction to the theory and its applications*. Courier Corporation, 2013.

[56] Lal Bahadur Prasad, Barjeev Tyagi, and Hari Om Gupta. Optimal control of nonlinear inverted pendulum system using pid

controller and lqr: performance analysis without and with disturbance input. *International Journal of Automation and Computing*, 11:661–670, 2014. DOI:10.1007/s11633-014-0818-1.

[57] MathWorks. Linear-quadratic regulator (lqr) design - matlab lqr, 2023. URL https://se.mathworks.com/help/control/ref/lti.lqr.html.

[58] C.-T. Chen. *Linear System Theory and Control*. Oxford University Press, New York, USA, 2013.

[59] Jon H Davis. *Foundations of deterministic and stochastic control*. Boston, MA, USA, 2002.

[60] David Luenberger. An introduction to observers. *IEEE Transactions on automatic control*, 16(6):596–602, 1971. DOI:10.1109/TAC.1971.1099826.

[61] Arvid Næss and Oleg Gaidai. Estimation of extreme values from sampled time series. *Structural safety*, 31(4):325–334, 2009. DOI:10.1016/j.strusafe.2008.06.021.

[62] Oleh Karpa. *Development of bivariate extreme value distributions for applications in marine technology*. PhD thesis, 2015.

[63] Arvid Næss and Torgeir Moan. *Stochastic dynamics of marine structures*. Cambridge University Press, Cambridge, UK, 2013.

[64] Yihan Xing, Oleg Gaidai, Yucong Ma, Arvid Næss, and Fang Wang. A novel design approach for estimation of extreme responses of a subsea shuttle tanker hovering in ocean current considering aft thruster failure. *Applied Ocean Research*, 123: 103179, 2022. DOI:10.1016/j.apor.2022.103179.

[65] Wei Chai, Bernt J Leira, and Arvid Næss. Probabilistic methods for estimation of the extreme value statistics of ship ice loads. *Cold regions science and technology*, 146:87–97, 2018.

[66] Florianr Menter. Zonal two equation kw turbulence models for aerodynamic flows. In *23rd fluid dynamics, plasmadynamics, and lasers conference*, page 2906, 1993. DOI:10.2514/6.1993-2906.

[67] Brian Edward Launder and Dudley Brian Spalding. The numerical computation of turbulent flows. In *Numerical prediction of flow, heat transfer, turbulence and combustion*, pages 96–116. Elsevier, 1983. DOI:10.1016/0045-7825(74)90029-2.

[68] David C Wilcox et al. *Turbulence modeling for CFD*, volume 2. DCW industries, Inc., CA, USA, 1998.

[69] Florian R Menter, Martin Kuntz, Robin Langtry, et al. Ten years of industrial experience with the sst turbulence model. *Turbulence, heat and mass transfer*, 4(1):625–632, 2003.

[70] DNV-GL. Rules for classification, naval vessels, part 4 subsurface ships, chapter 1 submarines. Standard DNVGL-RU-NAVAL-Pt4Ch1, Det Norske Veritas, Oslo, Norway, January 2018.

[71] A. J. Mariano, E. H. Ryan, B. D. Perkins, and S. Smithers. The mariano global surface velocity analysis 1.0. Report CG-D-34-95, United States Coast Guard Research and Development Centre, 1995.

[72] Gerhard Ersdal. An overview of ocean currents with emphasis on currents on the norwegian continental shelf. Report 010322, NPD Preliminary Report, 2001.

[73] Roald Sætre. *The Norwegian coastal current: oceanography and climate*. Fagbokforlaget, Bergen,Norway, 2007.

[74] M. Mohitpour, H. Golshan, and A. Murray. *Pipeline Design & Construction: A Practical Approach, Third Edition*. ASME Press, New York, USA, 01 2007.

[75] Erika De Visser, Chris Hendriks, Maria Barrio, Mona J Mølnvik, Gelein de Koeijer, Stefan Liljemark, and Yann Le Gallo. Dynamis co2 quality recommendations. *International journal of greenhouse gas control*, 2(4):478–484, 2008. DOI:10.1016/j.ijggc.2008.04.006.

[76] Equinor ASA. El001 northern lights - receiving and permanent storage of co2. Technical report, Equinor ASA, 2021. URL https://northernlightsccs.com/wp-content/uploads/2021/03/RE-PM673-00011-02-Impact-Assessment.pdf.

[77] Tomislav Šabalja, Ivo Senjanović, and Neven Hadžić. Structural design of a typhoon class submarine. In *Sorta 2014: zbornik radova XXI. simpozija Teorija i praksa brodogradnje, in memoriam prof. Leopold Sorta= Conference proceedings of the 21st symposium Theory and practice shipbuilding, in memoriam prof. Leopold Sorta*, pages 397–406, 2014.

[78] DNV-GL. Rules for classification, ships, part 2 materials and welding, chapter 2 metallic materials. Standard DNVGL-RU-SHIP-Pt2Ch2, Det Norske Veritas, Oslo, Norway, January 2019.

[79] JFE Steel . Steel plate, cat.no.c1e-001-08, 2021. URL https://www.jfe-steel.co.jp/en/products/plate/catalog/c1e-001.pdf.

[80] ASME. Boiler and pressure vessel code, section viii, division 2. Standard ASME BPVC.VIII.2, The American Society of Mechanical Engineers, New York, USA, 2015.

[81] ASME. Boiler and pressure vessel code, section ii, part d. Standard ASME BPVC.II.D, The American Society of Mechanical Engineers, New York, USA, 2015.

[82] ITTC. Recommended procedures and guidelines: Resistance test. Standard ITTC-57, 26th International Towing Tank Committee (ITTC) Resistance Committee, Zürich, Switzerland, 2011.

[83] Michael M Barnitsas, D Ray, and P Kinley. Kt, kq and efficiency curves for the wageningen b-series propellers. Technical report, University of Michigan, 1981.

[84] Martin Renilson. *Submarine Hydrodynamics*. Springer International Publishing AG, Cham, Switzerland, 1 edition, 2015.

[85] Hoyer Motor. Ie2 marine motor — 365 kw - 4p - frame 355 - b3, 2023. URL https://hoyermotors.com/products/motors/hoyer-ie2-marine-motors/.

[86] Rolls-Royce. Marine products and systems, 2023. URL https://www.rolls-royce.com/~/media/Files/R/Rolls-Royce/documents/marine-product-finder/MPS%202017%20LR.pdf.

[87] Wärtsilä. Lr2 product tanker data sheet, 2023. URL https://cdn.wartsila.com/docs/default-source/product-files/sd/merchant/tankers/data-sheet-ship-design-tanker-wsd47-113k.pdf?sfvrsn=c447c545_5.

[88] G. Mau. *Handbuch Dieselmotoren im Kraftwerks-und Schiffsbetrieb*. Springer-Verlag, Wiesbaden, Germany, 2013.

[89] Lutz Kretschmann, Hans-Christoph Burmeister, and Carlos Jahn. Analyzing the economic benefit of unmanned autonomous ships: An exploratory cost-comparison between an autonomous and a conventional bulk carrier. *Research in transportation business & management*, 25:76–86, 2017. DOI:10.1016/j.rtbm.2017.06.002.

[90] J. Elsey. How to define measure centrifugal pump efficiency: Part 1, 2023. URL https://www.pumpsandsystems.com/how-define-measure-centrifugal-pump-efficiency-part-1#:~:text=Centrifugal%20pumps%20can%20approach%2094,will%20vary%20by%20plant%20type.

[91] S. Hall. *Rules of thumb for chemical engineers*. Butterworth-Heinemann, Oxford, UK, 2017.

[92] Wärtsilä. Wsd50 30k 30,000 m3 lng carrier data sheet, 2023. URL https://cdn.wartsila.com/docs/default-source/product-files/sd/merchant/lng/wsd50-30k-lng-carrier-ship-design-o-data-sheet.pdf?sfvrsn=e8b38445_8ttps://cdn.wartsila.com/docs/default-source/product-files/sd/merchant/lng/wsd50-30k-lng-carrier-ship-design-o-data-sheet.pdf?sfvrsn=e8b38445_8.

[93] A. Depetro. The design safety challenges of a lithium-ion main storage battery for conventional submarines. In *the 4th SIA Submarine Science, Technology and Engineering Conference*, 2017.

[94] A Wikström. Lithium ion battery - opportunities and challenges for submarines. In *Presentation in 2019 Underwater Defence Technology*, Stockholm, Sweden, 2019.

[95] Y. Mikhaylik, I. Kovalev, C. Scordilis-Kelley, L. Liao, M. Laramie, U. Schoop, and T. Kelley. 650 wh/kg, 1400 wh/l rechargeable batteries for new era of electrified mobility. In *2018 NASA Aerospace Battery Workshop*, Alabama, USA, 2018.

[96] Yihan Xing, Marek Jan Janocha, Guang Yin, and Muk Chen Ong. Cfd investigation on hydrodynamic resistance of a novel subsea shuttle tanker. *Journal of Marine Science and Engineering*, 9(12):1411, 2021. DOI:10.3390/jmse9121411.

[97] Noriyuki Kokubun, Kiyohiko Ko, and Masahiko Ozaki. Cargo conditions of co2 in shuttle transport by ship. *Energy Procedia*, 37:3160–3167, 2013. DOI:10.1016/j.egypro.2013.06.202.

[98] Bert Metz, Ogunlade Davidson, HC De Coninck, Manuela Loos, and Leo Meyer. *IPCC special report on carbon dioxide capture and storage*. Cambridge: Cambridge University Press, New York, USA, 2005.

[99] Byeong-Yong Yoo, Dong-Kyu Choi, Hyun-Jin Kim, Young-Sik Moon, Hee-Seung Na, and Sung-Geun Lee. Development of co2 terminal and co2 carrier for future commercialized ccs market. *International Journal of Greenhouse Gas Control*, 12:323–332, 2013. DOI:10.1016/j.ijggc.2012.11.008.

[100] Ola Eiken, Philip Ringrose, Christian Hermanrud, Bamshad Nazarian, Tore A Torp, and Lars Høier. Lessons learned from 14 years of ccs operations: Sleipner, in salah and snøhvit. *Energy procedia*, 4:5541–5548, 2011. DOI:10.1016/j.egypro.2011.02.541.

[101] EPA. Inventory of u.s. greenhouse gas emissions and sinks. Technical Report 430-R-21-005, United States Environmental Protection Agency (EPA), 2021.

[102] Victor E Onyebuchi, Athanasios Kolios, Dawid P Hanak, Chechet Biliyok, and Vasilije Manovic. A systematic review of key challenges of co2 transport via pipelines. *Renewable and Sustainable Energy Reviews*, 81:2563–2583, 2018. DOI:10.1016/j.rser.2017.06.064.

[103] Joo-Youp Lee, Tim C Keener, and Y Jeffery Yang. Potential flue gas impurities in carbon dioxide streams separated from coal-fired power plants. *Journal of the Air & Waste Management Association*, 59(6):725–732, 2009. DOI:10.3155/1047-3289.59.6.725.

[104] Richard TJ Porter, Michael Fairweather, Mohamed Pourkashanian, and Robert M Woolley. The range and level of impurities

in co2 streams from different carbon capture sources. *International Journal of Greenhouse Gas Control*, 36:161–174, 2015. DOI:10.1016/j.ijggc.2015.02.016.

[105] European CCS Demonstration ProjectNetwork. Situation report 2012: a public report outlining the progress, lessons learnt and details of the european ccs demonstration project network. Technical report, Global CCS Institute, 2013.

[106] Mohammad Ahmad and Sander Gersen. Water solubility in co2 mixtures: Experimental and modelling investigation. *Energy Procedia*, 63:2402–2411, 2014. DOI:10.1016/j.egypro.2014.11.263.

[107] Yong Xiang, Zhe Wang, Xiaoxian Yang, Zheng Li, and Weidou Ni. The upper limit of moisture content for supercritical co2 pipeline transport. *The Journal of Supercritical Fluids*, 67:14–21, 2012. DOI:10.1016/j.supflu.2012.03.006.

[108] Auden Aspelund, MJ Mølnvik, and G De Koeijer. Ship transport of co2: Technical solutions and analysis of costs, energy utilization, exergy efficiency and co2 emissions. *Chemical Engineering Research and Design*, 84(9):847–855, 2006. DOI:10.1205/cherd.5147.

[109] Zero Emissions Platform. The costs of co2 transport: post-demonstration ccs in the eu. Technical report, 2011.

[110] Peter Brownsort. Ship transport of co2 for enhanced oil recovery-literature survey. Technical report, 2015.

[111] DNV-GL. Liquefied gas carriers with independent cylindrical tanks of type c. Standard DNVGL-CG-0135, Det Norske Veritas, Oslo, Norway, 2016.

[112] Manabu Hoshino, Naoki Saitoh, Hirohide Muraoka, and Osamu Saeki. Development of super-9% ni steel plates with superior

low-temperature toughness for lng storage tanks. *Shinnittetsu Giho*, pages 17–20, 2004.

[113] Kongsberg. Marine products and systems, 2019. URL https://www.kongsberg.com/globalassets/maritime/km-products/documents/product-catalog-2019.pdf.

[114] DNV-GL. Dnv-rp-c205 environmental conditions and environmental loads. Standard DNVGL-CG-0135, Det Norske Veritas, Oslo, Norway, 2010.

[115] Siyuan Yu, Wenhua Wu, Bin Xie, Shisheng Wang, and Arvid Næss. Extreme value prediction of current profiles in the south china sea based on eofs and the acer method. *Applied Ocean Research*, 105:102408, 2020.

[116] Baptiste Domps, Dylan Dumas, Charles-Antoine Guérin, and Julien Marmain. High-frequency radar ocean current mapping at rapid scale with autoregressive modeling. *IEEE Journal of Oceanic Engineering*, 46(3):891–899, 2021.

[117] Asgeir J. Sørensen. *Marine Cybernetics (Lecture Notes)*. Department of Marine Technology, NTNU, Trondheim, 2018.

[118] Kjersti Bruserud and Sverre Haver. Current conditions in the northern north sea. *Ocean Engineering*, 156:318–332, 2018. DOI:10.1016/j.oceaneng.2018.03.025.

[119] MathWorks. Linearize simulink model at model operating point, 2023. URL https://se.mathworks.com/help/slcontrol/ug/linearize-simulink-model.html.

[120] Tianjiao Dai, Shuo Yang, Yihan Xing, and Yucong Ma. Dynamic design and analysis of subsea co2 discharging flowline for cargo submarines used for ccs in low-carbon and renewable energy value chains. *Frontiers in Marine Science*, 9:1016062, 2022. DOI:10.3389/fmars.2022.1016062.

[121] DT Pugh. Estimating extreme currents by combining tidal and surge probabilities. *Ocean Engineering*, 9(4):361–372, 1982. DOI:10.1016/0029-8018(82)90029-4.

[122] Sean M Kery, Michael Eaton, Scott C Henry, John Vasilakos, and Sean M Kery. On the creation of a safe operating envelope for ships. In *SNAME Maritime Convention*, page D033S010R003. SNAME, 2018.

[123] Thomas Lombaerts, Stefan Schuet, Kevin Wheeler, Diana M Acosta, and John Kaneshige. Safe maneuvering envelope estimation based on a physical approach. In *Aiaa guidance, navigation, and control (gnc) conference*, page 4618, 2013.

[124] Phillip Marchant and N Kimber. Assuring the safe operation of submarines with operator guidline. In *Underwater Defence Technology*, Liverpool, UK, 2014.

[125] Alfred J Giddings and William L Louis. Overcoming submarine control—surface jams and flooding casualties. *Naval Engineers Journal*, 78(6):1055–1067, 1966. DOI:10.1111/j.1559-3584.1966.tb04132.x.

[126] Christopher Tingle. Submarine accidents a 60-year statistical assessment. *Professional Safety*, 54(09), 2009.

[127] QinetiQ. The influence of aft control surface configuration of a submarine on the submerged operational performance. In *Underwater Defence Technology*, Glasgow, UK, 2018.

[128] Jong-Yong Park and Nakwan Kim. Design of a safety operational envelope protection system for the pitch angle of a submarine. *Proceedings of the Institution of Mechanical Engineers, Part M: Journal of Engineering for the Maritime Environment*, 231(2):441–451, 2017. DOI:10.1177/1475090216644281.

[129] Jong-Yong Park and Nakwan Kim. Design of a safety operational envelope protection system for a submarine. *Ocean Engineering*, 148:602–611, 2018. DOI:10.1016/j.oceaneng.2017.11.016.

[130] Yihan Xing. A conceptual large autonomous subsea freight-glider for liquid co2 transportation. In *International Conference on Offshore Mechanics and Arctic Engineering*, volume 85161, page V006T06A052. American Society of Mechanical Engineers, 2021.

[131] Mark C Bettle, Andrew G Gerber, and George D Watt. Unsteady analysis of the six dof motion of a buoyantly rising submarine. *Computers & Fluids*, 38(9):1833–1849, 2009. DOI:10.1016/j.compfluid.2009.04.003.

[132] Roberto Font, Javier García, and Diana Ovalle. Modelling and simulating ballast tank blowing and venting operations in manned submarines. *IFAC Proceedings Volumes*, 43(20):67–72, 2010. DOI:10.3182/20100915-3-de-3008.00029.

[133] Roberto Font and Javier García-Peláez. On a submarine hovering system based on blowing and venting of ballast tanks. *Ocean Engineering*, 72:441–447, 2013. DOI:10.1016/j.oceaneng.2013.07.021.

[134] George D Watt. Modelling and simulating unsteady six degrees-of-freedom submarine rising maneuvers. Technical report, Dartmouth, Canada, 2007.

[135] Øyvind Notland Smogeli. Control of marine propellers: from normal to extreme conditions. 2006.

[136] Martin Renilson. *Submarine Hydrodynamics*. Springer International Publishing AG, Cham, Switzerland, 2 edition, 2018.

[137] Qinglong Chen, Hongwei Li, Shudi Zhang, Jian Wang, Yongjie Pang, and Qingyun Wang. Effect of waves on the behavior of emergent buoyantly rising submarines using cfd. *Applied Sciences*, 10(23):8403, 2020.

[138] George D Watt. A quasi-steady evaluation of submarine rising stability: the stability limit. In *RTO-AVT symposium on advanced flow management*, Loen, Norway, 2001.

[139] Shudi Zhang, Hongwei Li, Tiedong Zhang, Yongjie Pang, and Qinglong Chen. Numerical simulation study on the effects of course keeping on the roll stability of submarine emergency rising. *Applied Sciences*, 9(16):3285, 2019.

[140] Henry G Weller, Gavin Tabor, Hrvoje Jasak, and Christer Fureby. A tensorial approach to computational continuum mechanics using object-oriented techniques. *Computers in physics*, 12(6):620–631, 1998. DOI:10.1063/1.168744.

[141] Tokihiro Katsui, Satoshi Kajikawa, and Tomoya Inoue. Numerical investigation of flow around a rov with crawler based driving system. In *International Conference on Offshore Mechanics and Arctic Engineering*, volume 44946, pages 23–30. American Society of Mechanical Engineers, 2012. DOI:10.1115/OMAE2012-83280.

[142] Zhi Shang, David R Emerson, and Xiaojun Gu. Numerical investigations of cavitation around a high speed submarine using openfoam with les. *International Journal of Computational Methods*, 9(03):1250040, 2012. DOI:10.1142/S0219876212500405.

[143] David A Jones, Michel Chapuis, Mattias Liefvendahl, Daniel Norrison, and Ronny Widjaja. Rans simulations using openfoam software. Technical Report DST-Group-TR-3204, De-

fence Science and Technology Group: Fishermans Bend, VIC, Australia, Victoria, Australia, 2016.

[144] C Fureby, B Anderson, D Clarke, L Erm, S Henbest, M Giacobello, D Jones, M Nguyen, M Johansson, M Jones, et al. Experimental and numerical study of a generic conventional submarine at 10 yaw. *Ocean Engineering*, 116:1–20, 2016. DOI: 10.1016/j.oceaneng.2016.01.001.

[145] Han-Lieh Liu and Thomas T Huang. Summary of darpa suboff experimental program data. Technical report, Naval surface warfare center, Carderock division (NEWCCD), 1998.

[146] Chi Yang and Rainald Lohner. Prediction of flows over an axisymmetric body with appendages. In *The 8th International Conference on Numerical Ship Hydrodynamics*, Busan, Korea, 2003.

[147] Yi Liu, Zhiteng Zhou, Lixing Zhu, and Shizhao Wang. Numerical investigation of flows around an axisymmetric body of revolution by using reynolds-stress model based hybrid reynolds-averaged navier–stokes/large eddy simulation. *Physics of Fluids*, 33(8), 2021. DOI:10.1063/5.0058016.

[148] Praveen Kumar and Krishnan Mahesh. Large-eddy simulation of flow over an axisymmetric body of revolution. *Journal of Fluid Mechanics*, 853:537–563, 2018. DOI:10.1017/jfm.2018.585.

[149] Jingyuan Li, Qinghe Zhang, and Tongqing Chen. Numerical investigation of internal solitary wave forces on submarines in continuously stratified fluids. *Journal of Marine Science and Engineering*, 9(12):1374, 2021.

[150] ASME. Procedure for Estimation and Reporting of Uncertainty Due to Discretization in CFD Applications. *Journal of Fluids Engineering*, 130(7):078001, 07 2008. ISSN 0098-2202.

DOI:10.1115/1.2960953. URL https://doi.org/10.1115/1.2960953.

[151] Andrés Meana-Fernández, Jesús Manuel Fernández Oro, Katia María Argüelles Díaz, Mónica Galdo-Vega, and Sandra Velarde-Suárez. Application of richardson extrapolation method to the cfd simulation of vertical-axis wind turbines and analysis of the flow field. *Engineering Applications of Computational Fluid Mechanics*, 13(1):359–376, 2019. DOI:10.1080/19942060.2019.1596160.

[152] Patrick J Roache. Quantification of uncertainty in computational fluid dynamics. *Annual review of fluid Mechanics*, 29 (1):123–160, 1997. DOI:10.1146/annurev.fluid.29.1.123.

[153] Yihan Xing. Equinor subsea shuttle tanker concept study report. Technical report, University of Stavanger, Stavanger, Norway, 2019.

[154] Lars Davidson et al. Fluid mechanics, turbulent flow and turbulence modeling. *Chalmers University of Technology, Goteborg, Sweden (Nov 2011)*, 2011.

[155] Michael DP Bolzon, Richard M Kelso, and Maziar Arjomandi. Formation of vortices on a tubercled wing, and their effects on drag. *Aerospace Science and Technology*, 56:46–55, 2016.

[156] Kristy L Hansen, Nikan Rostamzadeh, Richard M Kelso, and Bassam B Dally. Evolution of the streamwise vortices generated between leading edge tubercles. *Journal of Fluid Mechanics*, 788:730–766, 2016.

[157] Yihan Xing, Tan Aditya Dwi Santoso, and Yucong Ma. Technical–economic feasibility analysis of subsea shuttle tanker. *Journal of Marine Science and Engineering*, 10(1):20, 2021.

[158] Wärtsilä. Aquarius ec ballast water management system product leaflet, 2018. URL https://www.wartsila.com/docs/default-source/product-files/bwms-files/brochure-o-aquarius-ec.pdf?utm_source=bwms&utm_medium=bwms&utm_term=aquariusec&utm_content=brochure&utm_campaign=msleadscoring.